Fall 2016

Novel quantitative description approaches assessing coronary morphology and development

Zhi Chen
University of Iowa

NOVEL QUANTITATIVE DESCRIPTION APPROACHES ASSESSING CORONARY MORPHOLOGY AND DEVELOPMENT

by

Zhi Chen

A thesis submitted in partial fulfillment of the
requirements for the Doctor of Philosophy degree
in Electrical and Computer Engineering
in the Graduate College of
The University of Iowa

December 2016

Thesis Supervisors: Professor Milan Sonka

Graduate College
The University of Iowa
Iowa City, Iowa

CERTIFICATE OF APPROVAL

PH.D. THESIS

This is to certify that the Ph.D. thesis of

Zhi Chen

has been approved by the Examining Committee for the thesis requirement for the Doctor of Philosophy degree in Electrical and Computer Engineering at the December 2016 graduation.

Thesis Committee: _____
Milan Sonka, Thesis Supervisor

_____
Andreas Wahle

_____
Edwin L. Dove

_____
Punam Saha

_____
Mona K. Garvin

ACKNOWLEDGEMENTS

I would like to first say thank you to my advisor, Dr. Milan Sonka, co-director of Iowa Institute for Biomedical Imaging (IIBI). He has given me constant support and guidance since the first day I began working with him. He helps me build up confidence by encouraging me and showing appreciation for all my work. Many thanks also go to Dr. Andreas Wahle for his advice and informative discussion throughout the entire project. I learned from both of them real scientific attitude about creativity, honesty, objectivity and curiosity.

My deep appreciation goes out to all cardiologists I have worked with. I have interacted with Dr. John Lopez weekly who is always helpful and provides me insight into cardiovascular diseases. A special thank you to Dr. Tomas Kovarnik for his patient data collection and intravascular ultrasound tracing work with our software. Without his diligent clinical work and invaluable feedback, my research aims would not have been achievable. I am also grateful to Dr. Michal Pazdernik for providing heart transplant datasets, which show me a chance to expand my research field. I am especially grateful to Dr. Michal Pazdernik and my colleague Zhihui Guo for taking a significant time and effort to manually trace IVOCT images. Without those precious tracings, my PhD study would not have been complete.

Dr. Ling Zhang deserves a special thank you for our collaborative work on registration throughout the IVUS project. I greatly appreciate the support from Dr. Honghai Zhang for graph-based discussions and guidance on coding conventions during the last phase of my PhD work. As a teaching assistant this semester, I am indebted to Dr. Mona K. Garvin especially for always providing homework solution in advance. This helps me a lot for grading and preparing for my office hours. Thus, I have more time to write my thesis. Additionally, I would like to thank Dr. Edwin L. Dove, Dr. Punam Saha and Dr. Mona K. Garvin for serving on my committee and guiding me through all these years.

Last but not least, I would like to give special thanks to my family: my dad and my mom, Guoqin Chen and Yinping Ye for always encouraging me to follow my dreams; my younger brother, Ziye Chen for always believing in me; my dear wife, Shichao Wang for her love and support over 10 years; my sweet daughter, Hannah Chen for bringing me the greatest happiness of life during this challenging period.

ABSTRACT

Coronary atherosclerosis is by far the most frequent cause of ischemic heart disease. Intravascular ultrasound (IVUS) along with virtual histology (VH) is a useful tool for quantification of coronary plaque buildup and provides new insights into the diagnosis of coronary disease. Rupture of vulnerable plaque causing acute coronary syndromes, coronary remodeling maintaining lumen size and plaque phenotype revealing pathological severity are among the most important topics related to atherosclerosis. In this thesis, variations of IVUS-VH-derived thin-cap fibroatheroma (TCFA) definitions are proposed to evaluate the plaque rupture, which is further analyzed in a layered manner; statins effects on coronary remodeling are comprehensively assessed with the implementation of automated IVUS segmentation and registration of IVUS pullbacks based on baseline and 1-year followup datasets; plaque phenotypes are determined and analyzed morphologically and compositionally on segmental basis using the same serial datasets.

In addition, our research involves another important coronary disease — coronary allograft vasculopathy (CAV) which is a frequent complication of heart transplantation (HTx). Another intra-coronary imaging modality — intravascular optical coherence tomography (IVOCT) for quantifying CAV is involved. We present an optimal and automated 3-D graph search approach for the simultaneous IVOCT multi-layer segmentation by transforming the 3-D segmentation problem into finding a minimum-cost closed set in a weighted graph. Furthermore, a computer-aided just-enough-interaction refinement method is proposed to help achieve fully satisfactory 3-D segmentation of IVOCT images. We believe this is the first work that provides a fast, efficient and accurate solution for IVOCT multi-layer assessment in the context of CAV.

The major contributions of this thesis are: (1) Proving that IVUS-VH-derived TCFA prevalence may be overestimated, and elucidating the potential loss of plaque

material during rupture, (2) providing a comprehensive understanding of remodeling in the context of both changing the remodeling direction and changing the remodeling extent, and demonstrating the statin therapy effects on remodeling across patients, based on automated segmentation of IVUS images and registration of serial data (3) showing that the pathological intimal thickening is the most active plaque phenotype in terms of plaque composition changes and plaque vulnerability progression, and (4) developing and validating a method for multi-layer 3-D segmentation of IVOCT images within a novel interactive environment.

PUBLIC ABSTRACT

Coronary atherosclerosis is the most frequent cause of ischemic heart disease. Intravascular ultrasound (IVUS) along with virtual histology (VH) is a useful imaging modality for quantification of atherosclerosis buildup. In this thesis, variations of IVUS-VH-derived thin-cap fibroatheroma (TCFA) definitions are proposed to evaluate plaque rupture causing acute coronary syndromes. It is proved that IVUS-VH-derived TCFA prevalence may be overestimated, and the potential loss of plaque material during rupture is elucidated as well in a layered analysis. With the implementation of automated segmentation of IVUS images and automated registration of baseline and 1-year followup datasets, statins therapy effects on coronary remodeling, a compensatory process in response to plaque progression, are comprehensively assessed in the context of both remodeling direction and remodeling extent. Additionally, plaque phenotypes revealing pathological severity of atherosclerosis are analyzed morphologically and compositionally on segmental basis using the same serial datasets, showing that pathological intimal thickening is the most active phenotype in terms of plaque composition changes and plaque vulnerability progression. Our research also involves another important coronary disease, coronary allograft vasculopathy (CAV), which is a frequent complication of heart transplantation. High-resolution imaging modality — intravascular optical coherence tomography (IVOCT) for quantifying CAV is utilized. We present and validate an optimal and automated 3-D graph search approach for simultaneous multi-layer segmentation of IVOCT images. Furthermore, a computer-aided just-enough-interaction refinement method is proposed to help achieve fully satisfactory results.

TABLE OF CONTENTS

LIST OF TABLES

Table

LIST OF FIGURES

Figure

CHAPTER 1
INTRODUCTION

1.1 Atherosclerosis and coronary artery disease

Coronary atherosclerosis (Figure 1.1) is by far the most frequent cause of ischemic heart disease, and rupture of vulnerable plaque or occlusive coronary disease causes the acute coronary syndromes of unstable angina, myocardial infarction, and sudden death [13, 54]. Some people have a genetic propensity for developing atherosclerosis but the disease could happen in almost everyone. Most people have atherosclerosis throughout their bodies and have no symptoms of heart ischemia at early stage but gradually develop some serious medical symptoms over decades. Although a broad spectrum of clinical heart diseases are atherosclerosis related, rupture of the atherosclerosic plaque accounts for the majority of acute events. While it is now well known that the risk of thrombosis, which develops during plaque rupture, depends on plaque composition, understanding of relationships between vessel morphology, plaque composition and atherosclerosic plaque progression and rupture remains incomplete. The intriguing complexity of the pathogenesis of human atherosclerosis and fatal complication of plaque rupture provides a rationale for this study.

1.2 Intravascular ultrasound (IVUS)

During past decades, coronary angiography is commonly performed to visualize the silhouette of coronary arteries. While angiography is limited in resolution and not able to visualize plaque, intravascular ultrasound (IVUS) is a valuable adjunct to angiography, ushering in the era of quantification of coronary plaque buildup and providing new insights into the diagnosis of coronary disease. IVUS allows tomographic cross-sectional visualization of the full luminal wall not just a 2D silhouette of the lumen and enables in vivo assessment of plaque morphology. A catheter is placed into distal coronary artery and pulled back to the aorta-ostial junction usually under motorized control at a constant speed of 0.5 mm/s. Gray scale images (Figure 1.2)

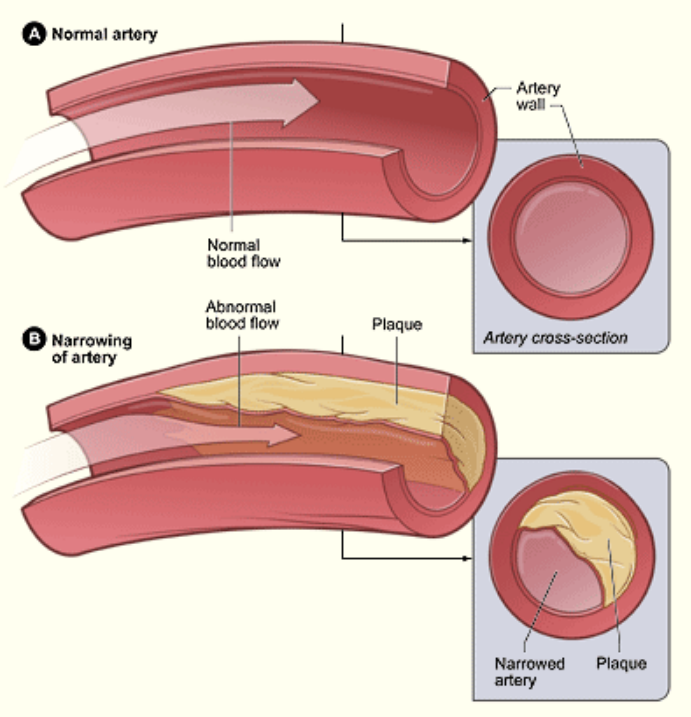

Figure 1.1: **Atherosclerosis**. In atherosclerosis, fatty streaks appear below the surface of artery and cells are accumulating in bulges along artery walls. The bulges are called plaques. Rather than uniformly thickening, plaques may be unevenly distributed sometimes. (Source: NHLBI, 2011a http://www.nhlbi.nih.gov/health/health-topics/topics/cad/)

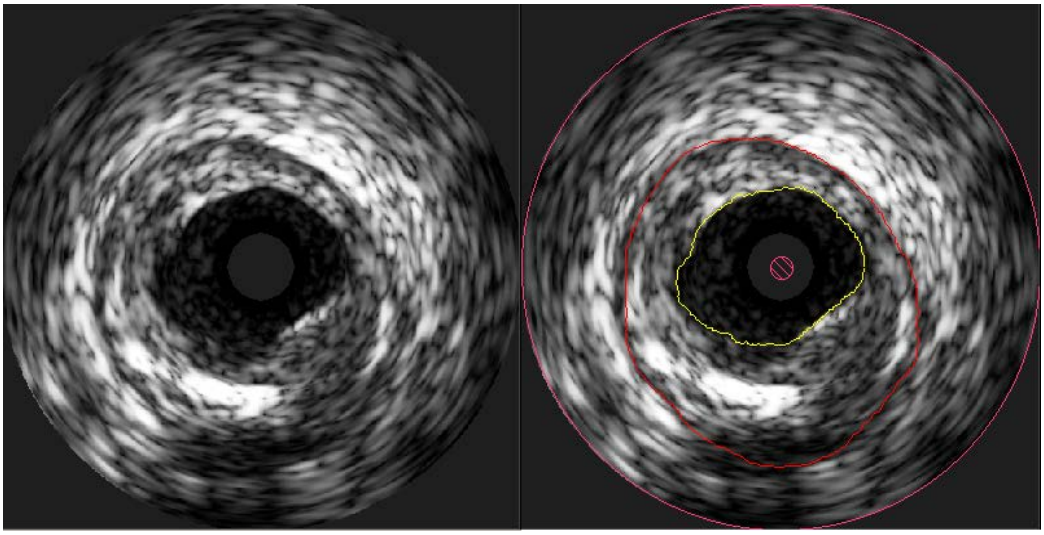

Figure 1.2: **Intravascular ultrasound**. Intravascular ultrasound cross-sectional image of left anterior descending artery is shown on the left with border delineation on the right. The atherosclerosic plaque is the area between the lumen (yellow) and adventitia (red).

are recorded during pullback. High ultrasound frequencies are used, typically at 20 to 40 MHz range and providing excellent theoretical resolution [42].

1.3 Virtual histology (VH)

One limitation of detection of vulnerable plaques using grayscale IVUS imaging is the inability to accurately characterize plaque components. In IVUS, dense plaque formations such as calcified and dense fibrous plaque are highly echoreflective, causing false imaging like shadowing. Meanwhile, the low echoreflective formations may include a broad range of tissues and are not easy to differentiate. A more detailed quantitative assessment on different plaque types — fibrous, fibro-fatty, necrotic core, and dense calcium are achieved by virtual histology IVUS (VH-IVUS). It's implemented through classification trees based on spectral analysis of IVUS radiofrequency backscattered data. Results from 51 LAD arteries showed that the classification of the four tissue types has high predictive accuracies of 89.5%-92.8% for the training

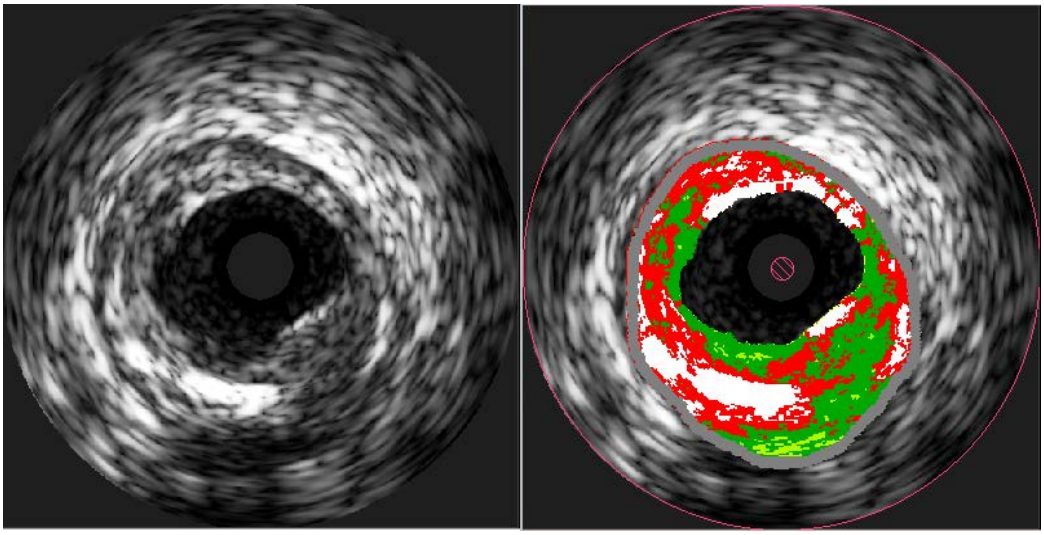

Figure 1.3: **Virtual histology**. The same IVUS image from Figure 1.2 is shown on the left with plaque components on the right, color-coded as white (dense calcium [DC]), red (necrotic core [NC]), light green (fibrofatty [FF]), and dark green (fibrous tissue [F])

data and 79.7%-92.8% for the test data [40]. The color-coded scheme used by VH is shown in Figure 1.3.

1.4 Coronary allograft vasculopathy (CAV)

Coronary allograft vasculopathy (CAV) is a frequent complication of heart transplantation (HTx), occurring in more than 50% of patients in the first post-transplant years. According to the Registry of the International Society for Heart and Lung Transplantation [20], CAV is the leading cause of death between 1 and 3 years after heart transplantation surgery. Unlike focal and eccentric conventional atherosclerosis, allograft vasculopathy is an accelerated coronary artery disease of concentric progressive intima thickening and diffuse luminal narrowing along the entire length of coronary vessels as shown in Figure 1.4. Treatment of CAV is limited for the lack of early clinical symptoms. Cardiac sympathetic denervation during transplantation not only reduces the heart control from nervous system but also prevents patients from

experiencing chest pain, which indicates an underlying heart problem. Patients with CAV usually do not seek medical attention at early stage and present late with silent myocardial infarction, heart failure or sudden death [23]. Therefore, this challenging complexity and silent fatality of coronary allograft vaculopathy proves the importance of early determination of layer-specific coronary wall thickening using intravascular imaging modality.

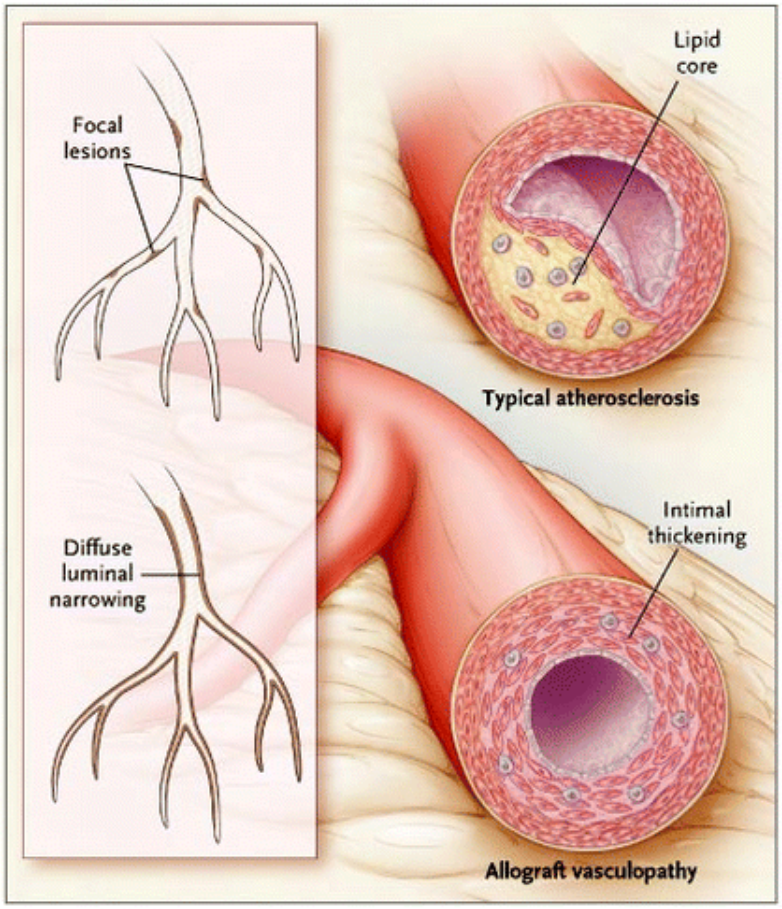

Figure 1.4: **Conventional atherosclerosis and coronary allograft vasculopathy** [2]. In contrast to focal and eccentric conventional atherosclerosis with formation of lipid core, CAV involves diffuse and concentric thickening of arterial intima.

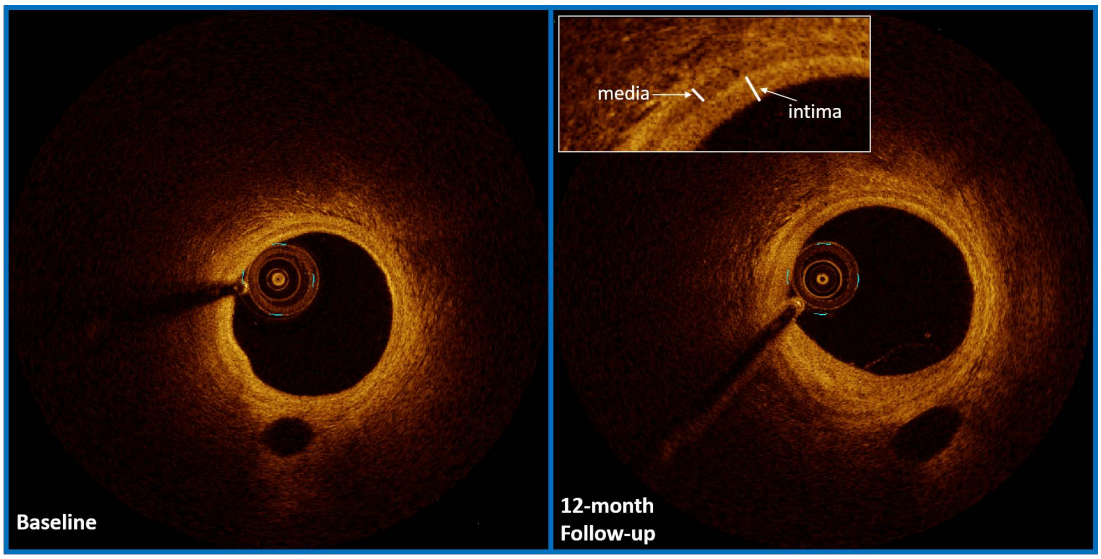

Figure 1.5: **Intravascular optical coherence tomograph.** Baseline and matched 12-month followup cross-sectional images obtained by IVOCT are displayed on left and right panel respectively. Artery wall shows a 3-layered structure, comprising high backscattering intima and low backscattering media and heterogeneous adventitia.

1.5 Intravascular optical coherence tomography (IVOCT)

CAV is a disease of progressive intima, which can be observed as early as 6 months after transplantation. Angiography and IVUS as the standard method for detecting focal plaques, lack sensitivity and resolution in detecting CAV through multi-layer analysis. Intravascular optical coherence tomography (IVOCT) is a new catheter-based intra-coronary imaging modality using near infrared light [25,58]. By measuring the delay time of optical echoes reflected or backscattered from biological tissues, IVOCT can obtain tissue structural information and provide cross-sectional images with a high resolution of 1020 μm (10 times greater than IVUS), making it feasible to visualize vessel wall layer structure in vivo at an unprecedented level of detail (see Figure 5.1). It has been proved that precise measurement of intimal thickness could be evaluated by IVOCT and correlated well with histological examination [32]. Thus, IVOCT is supremely qualified for quantitative assessment of early CAV.

1.6 Project history

1.6.1 Multi-modality fusion of angiography and IVUS

Andreas Wahle et al. have developed a comprehensive system that generates geometrically correct 3-D and/or 4-D (i.e. 3-D plus time) reconstructions of coronary arteries and computes quantitative indices of coronary morphology [70–72]. In general, vessel curvature and torsion are derived from a pair of single-plane or biplane angiograms and the cross-sectional information is obtained from IVUS. An example of reconstructed 3-D pullback path with lumen outline from a pair of single-plane angiograms with the mapping of IVUS data is shown in Figure 1.6. Once both angiograms and IVUS data are segmented, the fusion results in geometrically correct mapping of the IVUS borders to the true 3-D space allowing the calculation of associated quantitative indices [35–37, 68]. A database system for data and analysis-result handling, control and maintenance was developed to allow comprehensive tracking of all acquired and computed data.

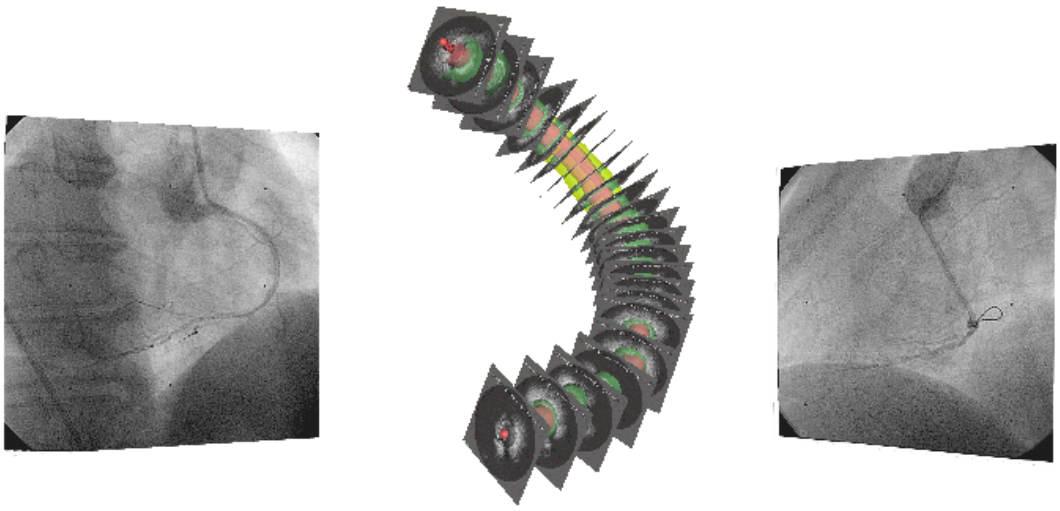

Figure 1.6: **Example of angiography-intravascular ultrasound fusion [69].**

1.7 Specific aims

In particular, the specific aims for this thesis are as follows:

- **Aim 1:** Develop and assess performance of variations of IVUS-VH-derived TCFA definitions for assessment of coronary plaque rupture.
- **Aim 2:** Develop novel IVUS-VH-based quantitative description approaches assessing location-specific serial changes of plaque morphology characteristics along the course of the vessel; perform a baseline/follow-up study of coronary plaque development in a patient population.
  - **Aim 2.1:** Use this approach to evaluate effects of lipid-lowering therapy on vascular remodeling.
  - **Aim 2.2:** Use this approach to evaluate morphological and compositional development of different plaque phenotypes.
- **Aim 3:** Develop a framework for multi-layer segmentation of coronary IVOCT using 3D graph search with just-enough-interaction editing.

1.8 Thesis overview

This thesis consists of five chapters as follows:

- Chapter 2 – Intravascular ultrasound based assessment of coronary plaque morphology.
- Chapter 3 – Comprehensive serial study of statin effects on coronary location-specific remodeling over general atherosclerotic artery.
- Chapter 4 – Novel quantitative approaches assessing plaque phenotype serial progression based on intravascular ultrasound.
- Chapter 5 – Multi-layer segmentation of coronary intravascular optical coherence tomography images.

- Chapter 6 – Conclusion and future directions.

CHAPTER 2
INTRAVASCULAR ULTRASOUND BASED ASSESSMENT OF CORONARY PLAQUE MORPHOLOGY

In this chapter, we review prior approaches and concepts assessing coronary plaque vulnerability and present a more comprehensive method (published at [21]) to evaluate coronary culprit sites based on IVUS-VH modalities.

2.1 Review of prior approaches assessing coronary plaque

Talking about coronary plaque morphology, the most important feature will be thin-cap fibroatheroma (TCFA). Recall that TCFA is a descriptive term used to imply vessel lesions that are at risk for rupture. According to American Heart Association, fibroatheroma is termed as advanced lesion where the fibrous "rim" keeping necrotic core from lumen is shrinking as disease progresses. If fibrous cap ruptures, fatty plaque full of necrotic core is exposed to blood flow causing blood clot around the rupture. Based on the actual cap thickness of autopsy specimens, TCFA (**Fig**. 2.1) is identified when a fibrous cap is < 65 μm thick and increased macrophages infiltration is involved. The value of 65 μm is chosen because in rupture, the mean cap thickness is 23 ± 19 μm; 95% of ruptured caps measure less than 64 μm [4].

However, due to the limited axial resolution (100-150 μm) of intravascular ultrasound (IVUS), it is impossible to visualize TCFA in cross-sectional IVUS images. To deal with this limitation, several studies proposed some indirect methods to identify TCFA based on its compositional and morphological characteristics by utilizing virtual histology (VH) to assess plaque components. Virmani et al. reported that nearly 75% of TCFA lesions have >10% area of the plaque occupied by necrotic core, and the mean cross-sectional area narrowing of the TCFA is 71% and most have 10-25% of the cross-sectional area occupied by necrotic core. [64]. Rodriguez-Granillo et al. defined a IVUS-derived TCFA as a lesion fulfilling the following criteria in at least 3 consecutive frames: necrotic core $\geq$10% without overlying fibrous tissue and plaque

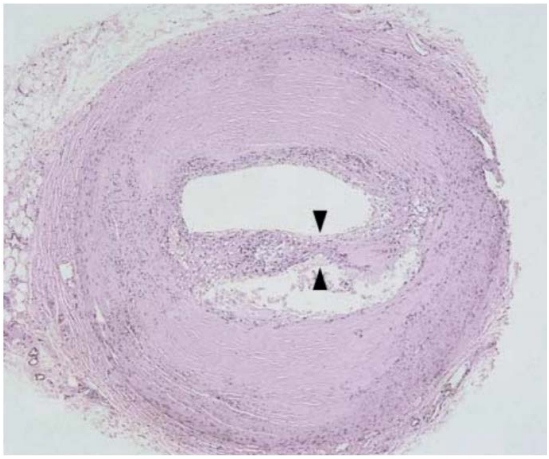

Figure 2.1: This is a cross-sectional photomicrograph of the epicardial coronary artery, showing a thin fibrous cap (arrows) overlying a lipid-rich or necrotic core [4].

burden $\geq$ 40% [50]. Maehara et al. expand the IVUS-derived TCFA definition by adding one more criterion: >30°of necrotic core abutting to the lumen in 3 consecutive frames [34]. All those observations attempted to mimic histopathologic findings and together formed the most widely used definition of IVUS-derived TCFA.

2.1.1 Limitations

This commonly used definition of IVUS-derived TCFA is mainly based on cut off for connected necrotic core (>10%) contacting lumen and extent of core-abutting-lumen proximity (>30°) as described above. But no compelling proof is provided for these cut off values and the determination has been proved to have a markedly higher interobserver variability [15, 56]. That is because spatial connectivity of confluent necrotic core and the criterion about how necrotic core touches the lumen in consecutive frames are not defined explicitly. Furthermore, in advanced lesion with heavy calcium coverage, the impact of calcium-associated acoustic shadowing may diminish the visibility of necrotic core behind areas of calcification due to echo loss. Last but not least, many studies rely on observer's personal experience to assess TCFA exis-

tence for lack of accurate quantitative tool. Therefore, this chapter focuses on the development of a comprehensive definition of IVUS-VH-derived TCFA by systematically varying features of standard definition and involving additional factors such as calcium impact. In addition, relationship between plaque rupture and other IVUS-VH-derived morphological features are also explored to better understand coronary plaque vulnerability.

2.2 Variations of thin-cap fibroatheroma (TCFA) definitions

A widely used standard IVUS-VH-derived definition of TCFA lesion is following two criteria in 3 consecutive frames:

- connected necrotic core (NC) in contact with lumen is $\geq$10% of plaque area.
- plaque burden (PB, plaque area divided by the adventitia cross-sectional area) is $\geq$ 40%

Note that IVUS-derived TCFA definition is based on environmental characteristics rather than features of cap itself. The motive behind it is that the axial resolution of IVUS (100-150 μm) is not good enough to detect TCFA (cap thickness $<$ 65 μm) directly. However, no persuasive evidence has been shown that this kind of definition is accurate. Therefore, we provide a total of 105 variations of current TCFA definition by giving more flexible arguments (**Fig**. 2.2):

- **TCFA Definition A (n=5)**:
  - NC in contact with lumen is $>$ 5/10/15/20/25% of plaque area. Note that "connected" limitation has been removed from original definition to allow a more general definition by involving all necrotic cores in plaque. Besides, cut off value is also varied by 5% interval to adopt more flexibilities.
  - PB is $\geq$ 40%, which represents the high-risk plaque and keeps unchanged.

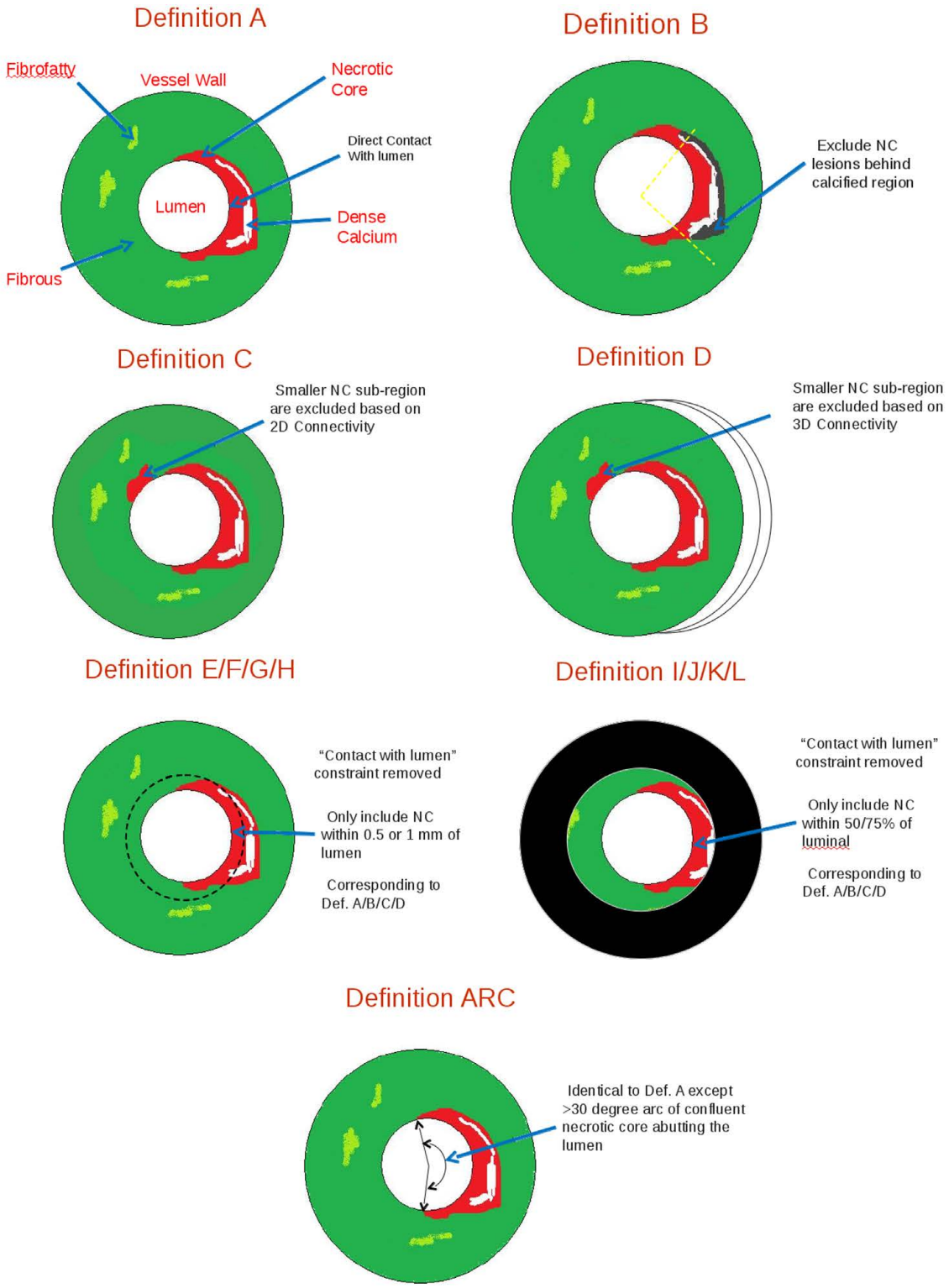

Figure 2.2: Variations of TCFA definitions

- **TCFA Definition B (n=5)**:
  - First 2 conditions are the same as Def. A.
  - NC lesions behind calcified region are excluded. It is known that heavy calcification would attenuate echo signal and influence the follow-up spectral analysis of backscattered radio frequency. There is a possibility that some areas identified as NC are artifacts behind calcium.
- **TCFA Definition C (n=5)**:
  - Re-define "connected NC": only largest 8-connective NC area in 2D space are counted. In original definition, judgment of NC confluence counts on the human eyes only.
  - Other conditions are the same as Def. A.
- **TCFA Definition D (n=5)**:
  - Re-define "connected NC": only largest 10-connective NC area in 3D space are counted.
  - Other conditions are the same as Def. A.
- **TCFA Definition E/F/G/H (n=40)**:
  - Constraint "in contact with lumen" is removed. Instead, only NCs within a constant ring — 0.5/1 mm from lumen border are counted. From Def. E to Def. L, only necrotic cores close to lumen are included considering luminal necrotic material are highly thrombogenic contents leading to blood clot formation. Additionally, removing lumen contact also provides more tolerance of lumen border tracing error.
  - Other conditions of E/F/G/H are corresponding to Def. A/B/C/D.

- **TCFA Definition I/J/K/L (n=40)**
  - "in contact with lumen" constraint is removed. Instead, only NCs within an adaptive ring — 50/75% of luminal plaque are counted.
  - Other conditions of I/J/K/L are corresponding to Def. A/B/C/D.
- **TCFA Definition ARC (n=5)**:
  - First 2 conditions are the same as Def. A.
  - NC arc abutting to the lumen is >30°. In contrast to Def. E to Def. L, this condition imposes a more strict requirement on definition of "touching" lumen by specifying at least 30°contact range as compulsory.

2.3 Patient population

To evaluate those 105 variations of TCFA definitions, 80 patients with stable angina (n = 37), unstable angina (n = 20), and myocardial infarction (n = 23) were selected for inclusion in this study based on the performance of preprocedure IVUS-VH imaging before culprit lesion modification and determination of high quality IVUS data with consistent and reliable automated pullback at least 30 mm in length, as described in [21]. For each patient, grayscale IVUS along with radio frequency based virtual histology was performed using IVUS phased array probe (Eagle Eye 20 MHz 2.9 F monorail; Volcano Corporation, Rancho Cordova, California), IVUS console, In-Vision Gold software, and automatic pullback at 0.5 mm/s (research pullback, model R-l00). A more detailed quantitative assessment on different plaque types — fibrous (F), fibro-fatty (FF), necrotic core (NC), and dense calcium (DC) was achieved using VH spectral analysis. Intraobserver variability of manual segmentation was assessed by randomly selecting 10 patients and measuring lumen (inner) and adventitia (outer) twice on 2 separate sessions. Intraobserver correlation coefficients for lumen and adventitia area are 0.98 and 0.96 respectively. Minimal lumen area has

0.08 mm^2 ($\pm$0.14 mm^2) difference while adventitia area has 0.25 mm^2 ($\pm$0.42 mm^2). Subsequently, grayscale IVUS, with manual segmentation of luminal and adventitia vessel wall, as well as corresponding color-coded IVUS-VH images were loaded and analyzed in our automated system.

2.4 Culprit and rupture

Total of 80 patients were divided into those with plaque rupture (n=15) and those without (n=65). When trying to evaluate the severity of coronary plaque, only the culprit lesion instead of whole vessel was analyzed. For patients without rupture, culprit frame was identified as frame with minimal lumen area. And for those experiencing rupture, culprit frame is of the largest rupture cavity, as shown in **Fig**. 2.3. Plaque rupture cavity was defined as residual area caused by the loss of plaque tissue after fibroatheroma cap tearing. As seen, this structural defect "expands" the original lumen area. To separate rupture cavity area from lumen area, the delineation was drawn by expert by connecting 2 lumen shoulder points representing the initial fibroatheroma cap locations before rupture, as demonstrated in **Fig**. 2.4. Based on rupture cavity concept, cavity angle is measured as well to indicate the angular extent of rupture. Furthermore, to better understand the relationship between axial plaque depth and development of plaque rupture, a circumferential analysis is proposed in this study in order to reveal the difference between the adluminal (near lumen) plaque and abluminal (away from lumen) plaque. One potential implementation difficulty is that the plaque is unevenly distributed rather than uniformly thickening. In other words, the plaque may have different accumulation rates on different axial angles. Thus, to compensate for such a circumferential unevenness, layers adaptive to plaque thickness (**Fig**. 2.4) are performed. In addition to axial direction, longitudinal environment of plaque rupture is also examined by defining proximal and distal reference frames as the closest non-ruptured frames (**Fig**. 2.5).

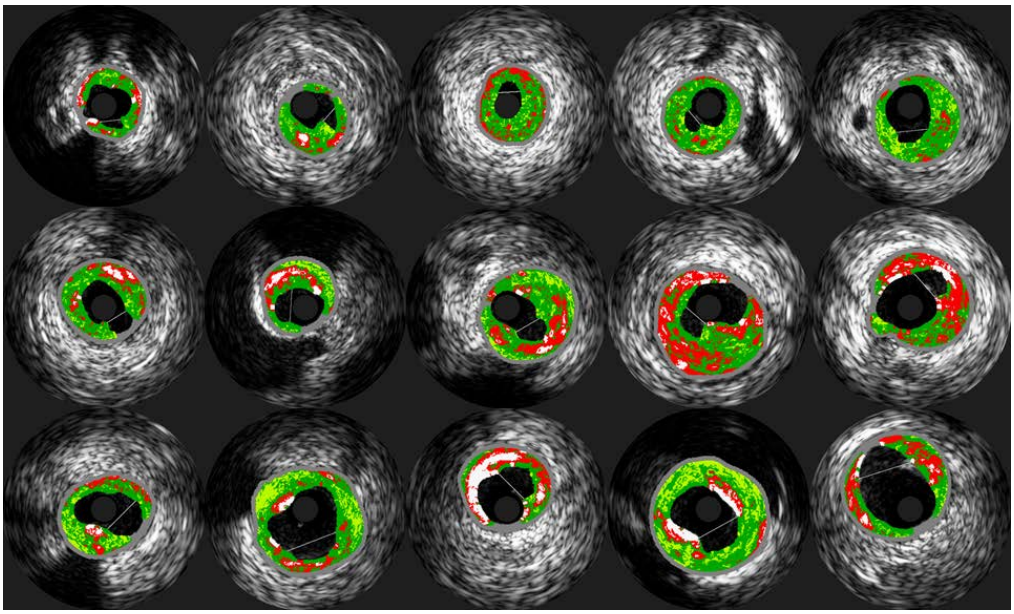

Figure 2.3: Cross-sectional IVUS-VH images of rupture plaque. Straight split lines specify the potential delineation between original lumen area and newly formed rupture cavity.

2.5 Results

The clinical demographic characteristics of all 80 patients are presented in **Table**. 2.1. There are no significant difference between rupture and non-rupture patients for demographics, clinical risk factors and medical treatment. As noted and expected, compared to non-rupture patients, more rupture patients experienced non-ST-elevation myocardial infarction (NSTEMI), which represents the ST segments on the electrocardiogram become elevated. NSTEMI is known as "full" heart attack and usually occurs by developing a partial or even complete occlusive coronary artery due to atherosclerosis.

For further comparison between rupture and non-rupture patients, morphological and compositional characteristics of coronary plaque are listed in **Table**. 2.2. Note that plaque burden here is defined as the ratio of plaque area to whole vessel cross-sectional area while eccentricity is defined as the ratio of minimal plaque thickness to

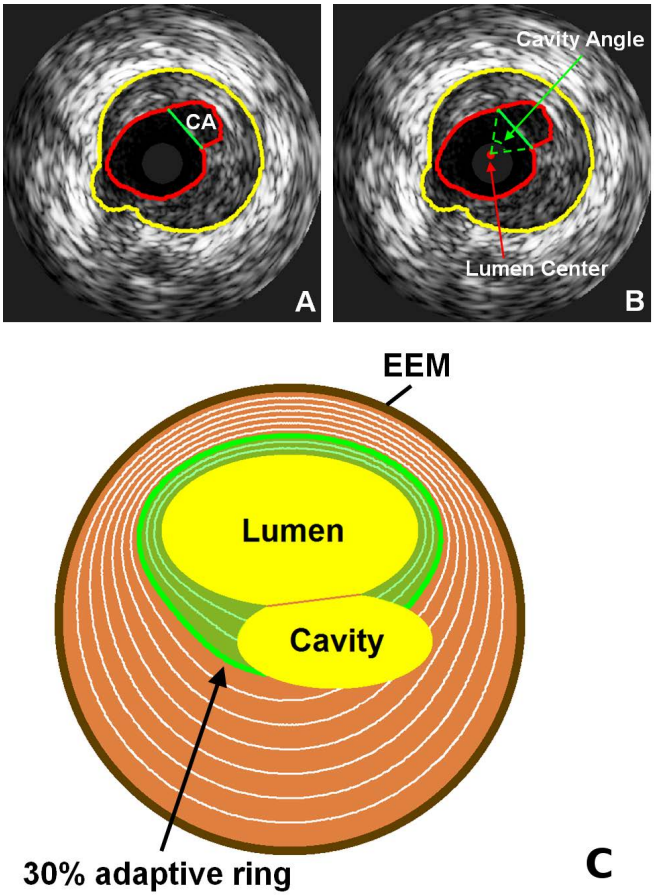

Figure 2.4: (A) Original IVUS image with plaque rupture with segmentation of lumen (red) and adventitia (yellow) borders. (B) Same image with lumen center and cavity delineation (green). Cavity angle is defined as the lumen-centered span between two shoulder points of delineation. (C) Schema of rings adaptive to plaque thickness.

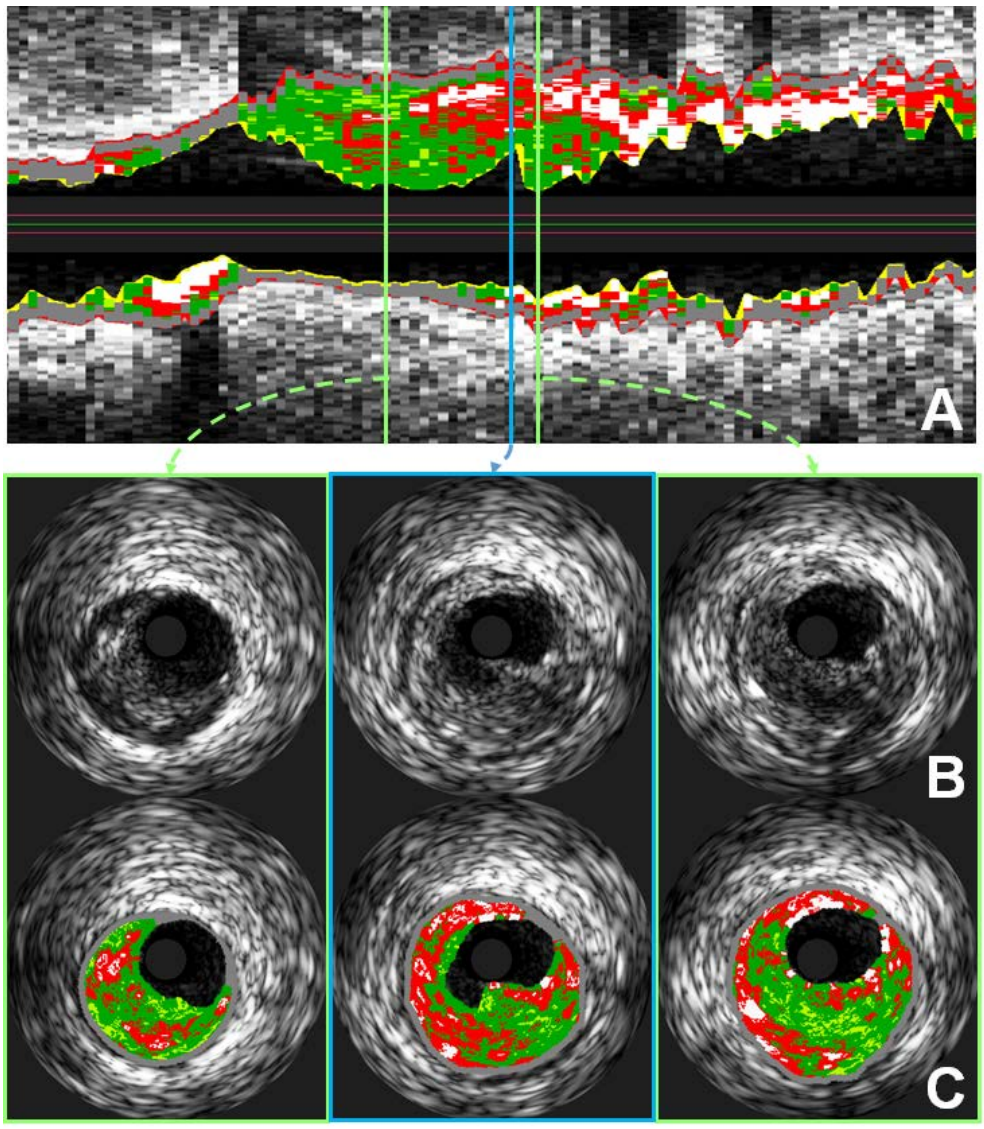

Figure 2.5: Proximal and distal reference frame without plaque rupture. (A) Longitudinal view of IVUS-VH pullback. Blue frame represents rupture culprit frame while left and right green frame represents the closest adjacent distal and proximal reference frames respectively. (B) Gray IVUS cross-sectional images. (C) Corresponding VH tissue classification results.

Table 2.1: Clinical demographic characteristics

	Total) (n=80)	Rupture (n=15)	Non-rupture (n=65)	p-value
Age	62 ± 10	63 ± 9	62 ± 11	0.57
Male	57 (72%)	9 (60%)	48 (74%)	0.35
White	46 (48%)	11 (73%)	35 (54%)	0.13
Clinical symptoms				
Stable angina	37 (47%)	5 (34%)	32 (49%)	0.39
Unstable angina	20 (25%)	2 (13%)	18 (28%)	0.24
NSTEMI	20 (24%)	7 (46%)	13 (20%)	**0.03**
STEMI	3 (4%)	1 (7%)	2 (3%)	0.50
Risk factors				
Hypertension	62/76 (82%)	12 (80%)	50/61 (82%)	0.86
Diabetes mellitus	30/76 (40%)	5/14 (36%)	25/62 (40%)	0.75
Hyperlipidemia	59/77 (77%)	11 (73%)	48/62 (77%)	0.73
End stage renal disease	6/76 (8%)	0 (0%)	6/61 (10%)	0.59
Chronic renal failure (Cre>1.5)	10/77 (13%)	2 (13%)	8/62 (13%)	1.00
Prior coronary artery disease	40 (50%)	8 (53%)	32 (49%)	0.14
Previous revascularization	30 (38%)	5 (33%)	25(39%)	0.18
Medications				
Ace inhibitor	45 (56%)	10 (67%)	35 (54%)	0.40
Aspirin	60 (75%)	11 (73%)	49 (75%)	1.00
Beta-blocker	44 (55%)	11 (73%)	33 (51%)	0.15
Thienopyridine	35 (44%)	8 (53%)	27 (42%)	0.57
Statins	54 (68%)	10 (67%)	44 (68%)	0.40

*NSTEMI stands for Non-ST-elevation myocardial infarction.

*STEMI stands for ST-elevation myocardial infarction.

maximal thickness for each frame. Similarly, no significant differences in lumen area and plaque components are found based on IVUS-VH cross-sectional findings.

Table 2.2: Morphological and compositional comparison of coronary plaque for culprit lesions based on IVUS-VH cross-sectional images.

	Rupture (n=15)	Non-rupture (n=65)	p-value
Lumen area (mm^2)	5.60 ± 3.30	5.20 ± 2.68	0.67
Plaque area (mm^2)	11.27 ± 3.83	10.79 ± 4.03	0.67
Plaque burden (%)	0.75 ± 0.13	0.78 ± 0.15	0.48
Eccentricity	0.69 ± 0.13	0.69 ± 0.16	0.95
Fibro-fatty	$11\% \pm 7\%$	$10\% \pm 10\%$	0.62
Fibrous	$59\% \pm 14\%$	$54\% \pm 24\%$	0.32
Necrotic core	$22\% \pm 11\%$	$18\% \pm 12\%$	0.22
Dense calcium	$8\% \pm 9\%$	$9\% \pm 11\%$	0.68

3-frame IVUS-VH computational analyses of 105 TCFA definitions are performed. As shown in **Table**. 2.3, the traditional criterion (Def. A with 10% NC threshold) used to define TCFA fails to differentiate plaque rupture lesions from non-rupture lesions: 87% of rupture culprit frames are identified as TCFA in comparison to 63% of non-rupture culprit frames (Fisher-exact test p = -0.125). Only 5 out of 105 variations are proved to have a different distribution between rupture and non-rupture patients based on Fisher-exact test. And only 2 of them (Def. A with 15% NC threshold and Def. L with 5% NC threshold and within 50% plaque ring) have a higher discriminating power for plaque rupture suggested by odds ratio analysis. Note that odds ratio is not applicable to Def. I (5% NC & 75% ring).

The association between plaque rupture area (cavity size) and layered plaque components (NC% and F%) are compared using each of 10 adaptive rings from 10% to 100% of plaque area as described in **Fig**. 2.5. The significant correlation coefficients (r value) for all rings are displayed in **Fig**. 2.6. As shown, NC% close to lumen especially

Table 2.3: IVUS-VH-derived thin-cap fibroatheroma comparison as predictors of plaque rupture based on variations of standard definition

	Rupture (n=15)	Non-rupture (n=65)	Fisher-exact p-value	Odds ratio p-value
Standard Def. A (10% NC)	13 (87%)	41 (63%)	0.125	0.09
Def. A (15% NC)	13 (87%)	36 (55%)	**0.037**	**0.04**
Def. D (10% NC)	14 (93%)	42 (68%)	**0.031**	0.06
Def. I (5% NC & 50% ring)	14 (93%)	42 (68%)	**0.031**	0.06
Def. I (5% NC & 75% ring)	15 (100%)	47 (72%)	**0.018**	NA
Def. L (5% NC & 50% ring)	14 (93%)	41 (63%)	**0.029**	**0.03**

from 20% to 40% rings is found to have the most positive correlation with rupture cavity area. No correlation is detected for NC% after 70% of plaque thickness from lumen border. Meanwhile, negative correlation between F% and rupture cavity area is found over the whole plaque area from 10% to 100% rings. 30% adaptive ring is chosen as representative for both cases and is displayed in detail in **Fig**. 2.6.

Further analysis of 30% ring by comparing rupture culprit frame of the largest cavity area with nearby intact reference frames is presented in **Fig**. 2.7. Rupture culprit frames show significantly less NC area (p=0.013) and F area (p=0.009) compared to proximal and distal reference frames, indicating that NC and F tissues tend to break out of plaque during rupture process.

2.6 Discussion and conclusion

Clinical investigation have shown that thin-cap fibroatheroma (TCFA) is recognized as a precursor for rapid plaque progression resulting in rupture and future acute coronary syndromes (ACS) and sudden cardiac death [9,56]. Intravascular ultrasound (IVUS) along with virtual histology (VH) using spectral analysis of radiofrequency is the gold standard for evaluation of coronary plaque morphology including TCFA for past decade. Due to IVUS incapability of visualizing TCFA of $< 65\mu$m under its the limited axial resolution (100-150 μm), several studies [34,50,64] used the necrotic

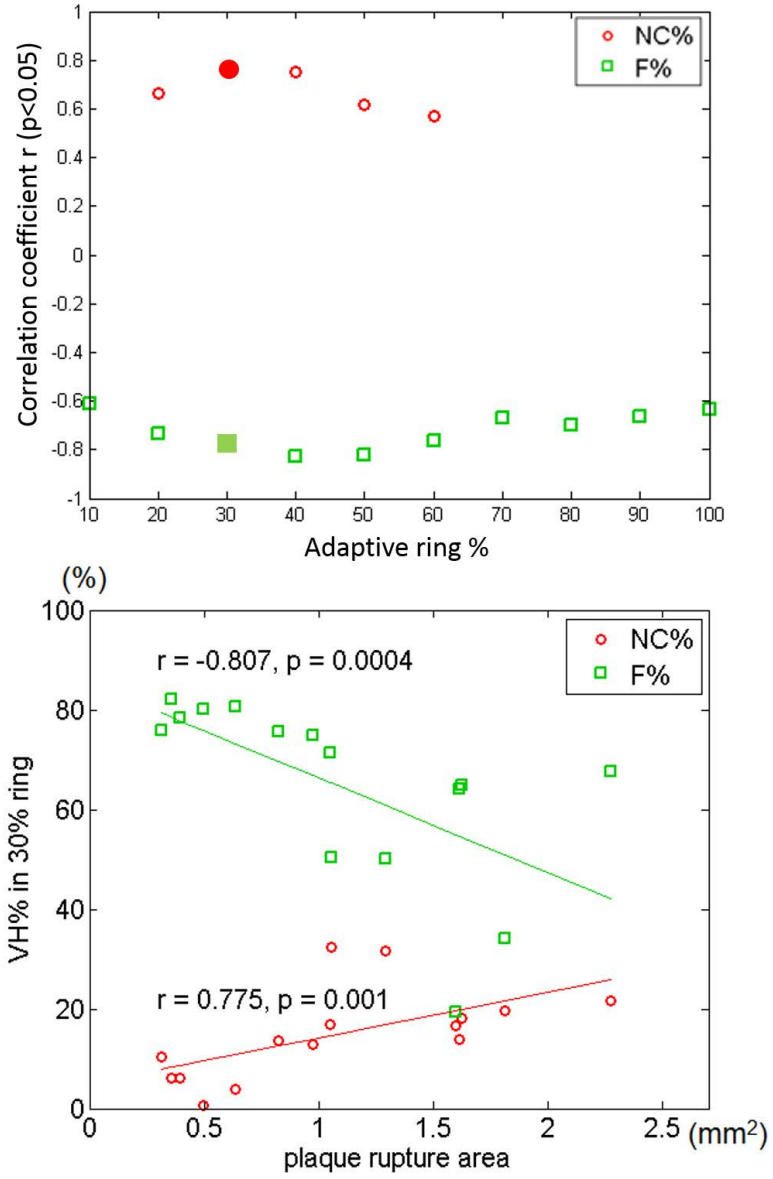

Figure 2.6: Significant correlation coefficients between plaque rupture area and plaque components (NC% and F%) for each adaptive ring are plotted on the top, while specific details in 30% adaptive ring indicating the greatest correlation are displayed on the bottom.

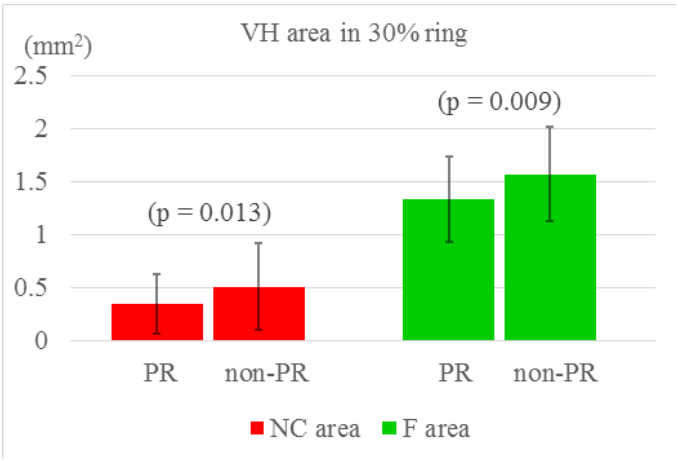

Figure 2.7: Necrotic core (NC) area and fibrous (F) area comparison between culprit frame with plaque rupture (PR) and reference frames without plaque rupture.

core tissues contacting the lumen to define IVUS-VH-derived TCFA and evaluate subsequent correlation with clinical outcomes. Nevertheless, less than 10% of IVUS-VH-derived TCFAs are associated with clinical event in most studies [5, 9, 56]. We provide 105 variations of IVUS-VH-derived TCFA definitions in an effort to improve event attribution and determine the best TCFA definition associated with plaque rupture process. In result, only 2 of them (Def. A with 15% NC threshold and Def. L with 5% NC threshold and within 50% plaque ring) have a better discriminating power to plaque rupture than widely used original definition, which fails to distinguish rupture from non-rupture at all. According to these 2 definitions, both rupture and non-rupture plaque frames have more than 60% presence of TCFA, which far exceeds TCFA frequency observed in similar autopsy study [10]. All these together suggests that IVUS-VH-derived TCFA prevalence may be overestimated and in return its association with plaque rupture is diluted owning to coarse axial resolution of IVUS and questionable ability of VH to differentiate lipid pool and necrotic core [63]. By contrast, new technique such as optical coherence tomography (OCT) with a resolution of 15 to 20 μm is far superior to identify thin caps of TCFA and assess plaque

vulnerability index.

Additionally, to evaluate the relationship between rupture cavity size and IVUS-VH-derived plaque morphology and components, quantitative analyses along both axial and longitudinal vessel direction are performed. By restricting analysis into a layered fashion adaptive to axial plaque thickness, increasing cavity size is revealed to be significantly correlated with more necrotic core and less fibrous tissue within near lumen range. Our observation provides a potential explanation to the well known association between higher incidence of acute coronary syndromes and larger necrotic core area [26,56]. Ohsima et al. has also proved that cavity volume of ruptured plaque is closely associated with higher incidence of post-infarction complications in patients with STEMI [44]. Our evaluation of cavity size of IVUS-VH may provide useful information for the prediction of such complications. As for the longitudinal analysis along the vessel, it is demonstrated that plaque rupture frames have less necrotic core and fibrous tissue compared with adjacent proximal and distal reference frames. It strongly implies that NC and F tissues tend to break out of plaque during rupture process. To our knowledge, this is first in vivo study that elucidated the potential loss of plaque material during rupture.

CHAPTER 3
COMPREHENSIVE SERIAL STUDY OF STATIN EFFECTS ON CORONARY LOCATION-SPECIFIC REMODELING

In this chapter, lipid-lowering medication effects on coronary remodeling has been evaluated comprehensively based on baseline and 1-year followup serial study using computer aided intravascular ultrasound imaging analysis (presented at SPIE 2016 [8]).

3.1 Introduction

Human coronary remodeling was originally described by Glagov et al. as a compensatory process to maintain vascular lumen patency in response to atherosclerotic plaque development based on necropsy material and histopathologic techniques [17]. And it is further supported and verified by in vivo, close-chested investigation using intravascular ultrasound [19]. Positive remodeling (PR) has since been defined as artery enlargement in response to plaque accumulation and is proved to have a paradoxical effect, both maintaining lumen size and promoting plaque vulnerability [62]. Intuitively, the remodeling concept has evolved to include artery shrinkage which is called negative remodeling (NR). NR has been related to luminal narrowing [48] and are associated with plaque stabilization processes and more stable phenotypes [51,53,62].

While coronary remodeling itself is a dynamic process pertaining to the development of atherosclerosis, earlier intravascular ultrasound (IVUS) studies [17,19,48,51, 62], owing to the lack of serial measurements over the different time, were forced to use an indirect index, which describes the magnitude and direction of remodeling as a ratio of identified cross-sectional vascular area to local reference area coming from the same vessel. This static index fails to avoid arterial tapering influence and causes problems if the reference area experiences notable changes due to the temporal development of coronary disease. Even when serial studies are available [53], the static remodeling index obtained at a single time point is still invariably used due to diffi-

culties of matching/registering individual lesions over time. Other serial studies [66] lack generalization and fail to assess the remodeling process over the entire length of the imaged vessel because only one single lesion frame from one vessel is matched manually and subsequently analyzed.

In autopsy studies, Pasterkamp et al. [46] found that arterial remodeling may vary among different individuals. Furthermore, Zarins et al. [76] proved that different segments of the same artery may respond differently to increasing atherosclerotic plaque. They mainly focus on the natural history of atherosclerotic arterial remodeling. Statin has be proved to be the most effective class of lipid-lowering medications, which improves survival in patients with coronary heart disease [18, 61]. In this paper, we try to resolve above-mentioned limitations and present an in vivo study to comprehensively examine statin effect on coronary dynamic remodeling at different segments of long vessels based on serial measurements at initial and 12-month follow-up time. Multiple imaging modalities, i.e., angiography, intravascular ultrasound (IVUS) and virtual histology (VH), are applied and analyzed by our computer-aided, semi-automatic system.

3.2 Method

3.2.1 Patient population

IVUS-VH image pullbacks from 61 patients were taken from the database of serial IVUS studies of patients with stable coronary artery disease enrolled at the Charles University Hospital, Prague, and were selected according to the inclusion criteria [30]: (1) native artery with 20∼50% stenosis on angiography had no indication for either percutaneous coronary intervention (PCI) or coronary artery bypass grafting (CABG); (2) segment length with plaque burden $> 20\%$ was greater than 20 mm on IVUS; (3) coronary artery with the longest plaque during angiography was selected. All patients agreed to routine elective follow-up examinations of one coronary artery per patient at 12.3 months (11.9 $\sim$ 12.9 months) after the initial enrollment and

baseline imaging. In other words, a repeat IVUS-VH examination of the same vessel segment is performed after 1-year statins treatment. 25 mm long mutual overlap between baseline and followup pullbacks are prerequisite. 48 out of 61 patients received statin lipid-lowering therapy before enrollment and all of them received statin treatment after enrollment (45 of them received aggressive treatment — atorvastatin 80 mg, ezetimibe 10 mg). Demographic characteristics of patients are shown in Table 3.1. The 61 imaged vessel segments have a median length of 38.0 mm (30.3 $\sim$ 48.4 mm).

Table 3.1: Demographic characteristics

Characteristics	**Total (n=61)**
Age, mean±sd	62.1 ± 9.9
Sex, male, n (%)	47 (77.0%)
Current smokers, n (%)	42 (68.9%)
Previous smokers, n (%)	37 (60.7%)
Family history of coronary disease, n (%)	33 (54.1%)
Arterial hypertension, n (%)	56 (91.8%)
Diabetes mellitus, n (%)	17 (27.9%)
Myocardial infarction in past, n (%)	36 (59.0%)
Prior statins treatment, n (%)	48 (78.7%)
Aggressive lipid lowering therapy, n(%)	45 (73.8%)
Artery	
Right coronary, n (%)	27 (44.3%)
Left anterior descending, n (%)	23 (33.7%)
Left circumflex, n (%)	11 (18.0%)
Baseline total cholesterol (mmol/l), mean±sd	4.29 ± 1.08
Followup total cholesterol (mmol/l), mean±sd	3.48 ± 1.00
Δtotal cholesterol (%), p-value	-18.9%, $p < 0.001$
Baseline LDL cholesterol (mmol/l), mean±sd	2.44 ± 0.91
Followup LDL cholesterol (mmol/l), mean±sd	1.90 ± 0.75
ΔLDL cholesterol (%), p-value	-22.5%, $p < 0.001$
Baseline HDL cholesterol (mmol/l), mean±sd	1.20 ± 0.36
Followup HDL cholesterol (mmol/l), mean±sd	1.19 ± 0.31
ΔHDL cholesterol (%), p-value	-0.01%, $p = 0.99$

*LDL indicates low-density lipoprotein
HDL indicates high-density lipoprotein

3.2.2 Acquisition and segmentation of intravascular ultrasound images

Grayscale B-mode IVUS images were acquired using 20MHz Eagle Eye probe and motorized research R-100 pullback made by Volcano Corporation (Rancho Cordova, CA, USA). Histological plaque components (necrotic core, dense calcium, fibrous and fibrofatty) were identified and color-coded by spectral analysis of IVUS radiofrequency signal [40]. To quantitatively assess morphological characteristics of the atherosclerotic plaque, luminal and external adventitial surfaces were automatically segmented in each frame of all IVUS pullbacks using our fully three-dimensional LOGISMOS graph-based approach [33, 74]. In brief, two surfaces were simultaneously segmented as the minimum-cost closed set in a weighted graph. Automatically determined surfaces were then reviewed and algorithmically refined by an expert cardiologist using an operator-guided computer-aided just-enough-interaction approach to generate high quality segmentation results [7, 57]. Figure 3.1 displayed the graphical user interface for IVUS segmentation and Figure 3.2 displayed some final segmentation results. This new automated segmentation method delivered significantly better results compared to the previous work in [12] (p-value < 0.02), and more importantly, it allowed the user to generate high quality segmentation results with the average operation time reduced from several hours to several minutes, making it feasible to involve more frames and more patients for a more comprehensive assessment in a limited resource.

Employing our previously-reported approach [71] to obtain accurate cross-sectional morphology, not depending on a perpendicular catheter orientation, geometrically correct 3D representation of the vascular wall surfaces was obtained via fusion of two-plane angiography and IVUS. Additionally, a database system for data and analysis handling, control, and maintenance was developed as well to allow comprehensive tracking of acquired and computed data. Our semi-automatic system has reduced the average time for tracing IVUS images from several hours to minutes while demon-

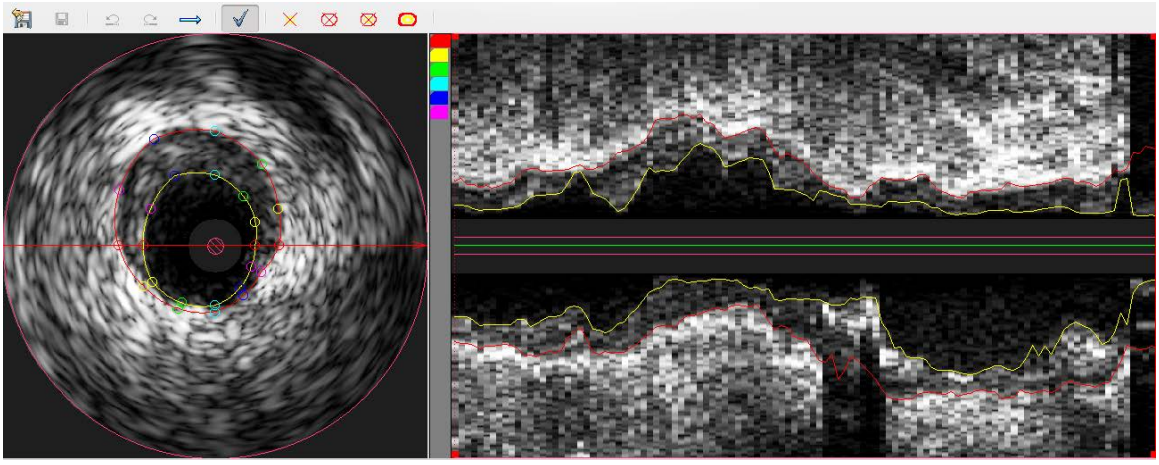

Figure 3.1: Interface for IVUS segmentation. The right panel is cross-sectional view while the left panel is longitudinal view on horizontal plane along the vessel. Lumen and adventitia border are displayed as red and yellow delineation respectively. The just-enough-interaction editing can be done efficiently on both cross-sectional and longitudinal view with inherent 3-D implementation.

strating excellent accuracy [7, 57].

3.2.3 Registration of serial IVUS data

Ideally, baseline and follow-up IVUS imaging would be performed under identical conditions with identical vessel segment coverage, catheter orientation, heart rate and pullback speed. However, this cannot be ensured in reality and both pullbacks need to be matched to provide accurate temporal changes of plaque. Using our recently reported 3D graph optimization approach [77], pairs of serial IVUS pullbacks of the same vessel were registered by implementing a cost function that jointly reflects similarity of vessel/plaque morphology and perivascular image appearance, which included shadow after calcified plaque, coronary branches, passing micro vessels etc. Consequently, global optimality of the resulting registration was achieved due to the employed cost function. The registration results were evaluated on well-identifiable landmarks determined by experts and were proved to be comparable to inter-observer

variability with mean distance errors ranging from 0.72 mm to 0.79 mm and mean rotational angle errors ranging from 7.3° to 9.3°. The IVUS images beyond the overlapping range were discarded. After registration as shown in Figure 3.2, dynamic serial coronary remodeling over the entire pullback length can be assessed and monitored.

3.2.4 Baseline predictive regression

This study is part of an ongoing predictive investigation of serial development of human coronary atherosclerosis. Thus, demographic data, clinical risk factors and baseline atherosclerotic plaque morphology and composition for each patient were obtained and defined here as baseline predictors, which represent the potential reasons for followup remodeling development. Arterial remodeling consists mainly of two types of tissue transformation – plaque accumulation and adventitia deformation, which together have been identified as the determinant of lumen size and may equally contribute to the luminal narrowing [47]. Therefore, relations between plaque/adventitia serial changes and baseline predictors were investigated by regression analysis in this study.

3.2.5 Statistical analysis

Discrete variables are presented as n (%) and continuous variables are denoted as mean (± standard deviation) or median (and interquartile range) as appropriate. All IVUS frames from the same vessel were analyzed, which could contribute to analysis bias due to clustered data. To correct for systematic errors introduced by clustering, generalized linear mixed model with patient as random effect was used to investigate the relationship between continuous response variables (e.g., change of plaque area) and categorical/continuous predictors. Moreover, mixed-effect logistic regression is used to investigate the association of binary response variables (e.g., direction of plaque area change) and baseline predictors. $p < 0.05$ was used to determine statis-

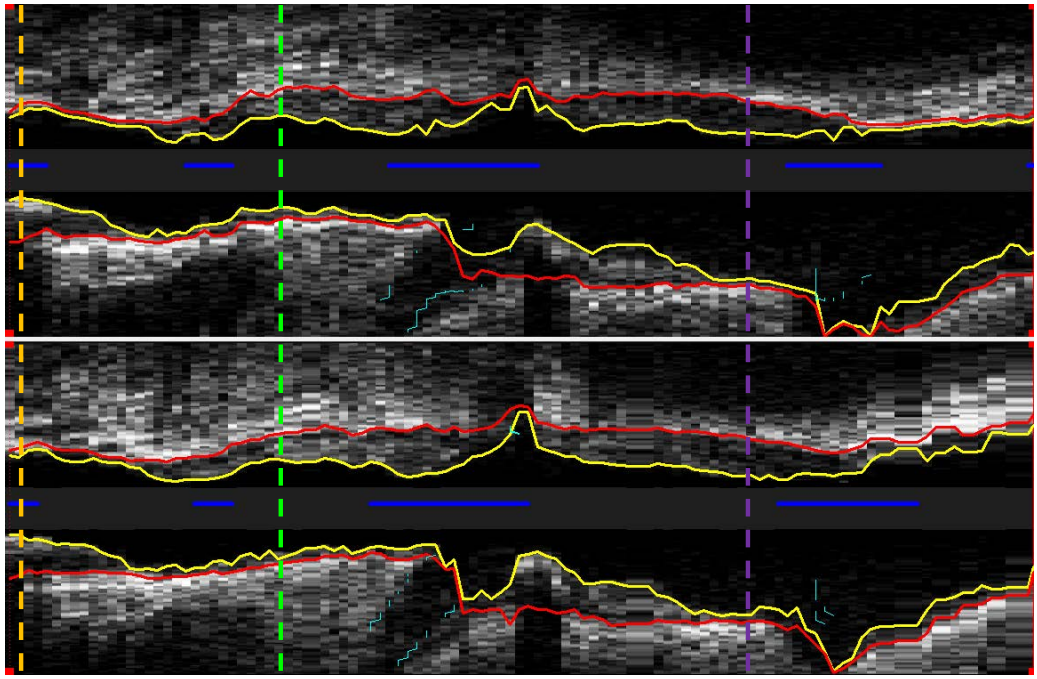

(a)

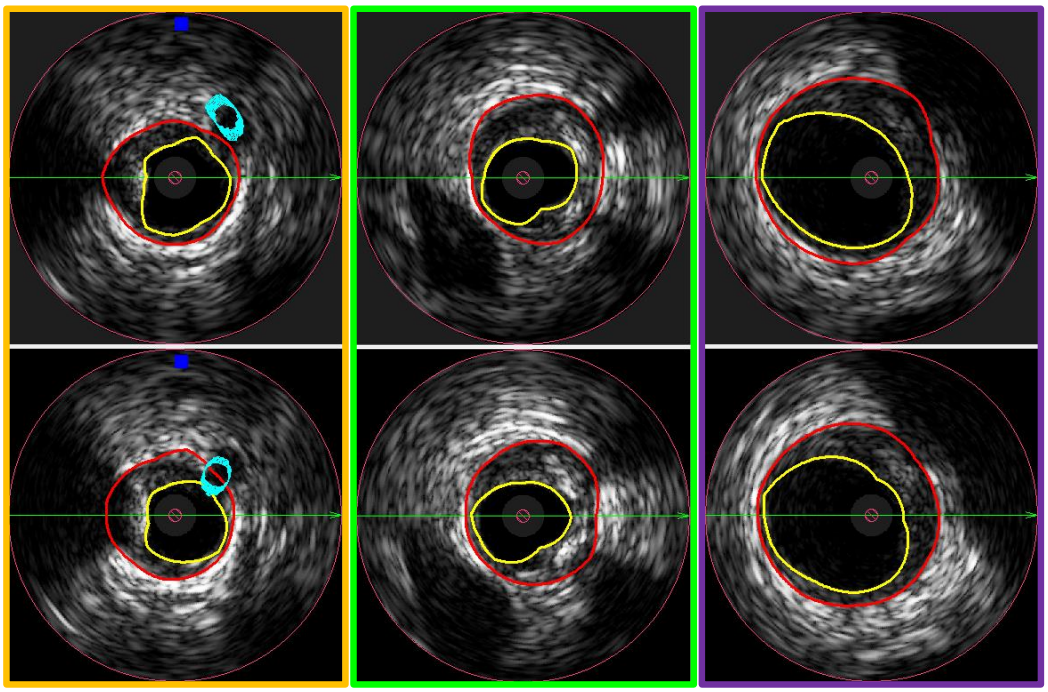

(b)

Figure 3.2: IVUS segmentation and registration. Longitudinal view of registered baseline and followup pullbacks are displayed on the upper and lower panels as shown in (a). Cross-sectional view presents the results of IVUS segmentation of lumen (yellow) and adventitia (red) as shown in (b). Dark blue horizontal bar in (a) and light blue mesh grid in (b) show the range and shape of branches, which are used as part of evaluation ground truth for assessing registration accuracy.

tical significance. All statistical tests were conducted in R (Version 3.1.1, Core Team 2014).

3.3 Results

Total of 5215 cross-sectional IVUS-VH frames from 61 pullbacks were matched and analyzed from baseline to followup.

3.3.1 Direction of plaque development

Frame-level analysis: Most frames (about 58.6%) experienced decreased plaque cross-sectional area (CSA) from baseline to followup while 41.4% of frames experienced the opposite during statins treatment. According to the frequency distribution of plaque CSA changes shown in Table 3.2, plaque regression (baseline plaque CSA > followup plaque CSA) is more likely to happen during lipid lowering therapy.

Table 3.2: Frequency distribution of plaque cross-sectional area changes (total frames n = 5215)

Decreased Plaque CSA (mm^2)	< 0	< -1	< -2	< -3	< -4	< -5
n (%)	3058 (58.6%)	1129 (21.6%)	407 (7.8%)	181 (3.5%)	92 (1.8%)	43 (0.8%)
Increased Plaque CSA (mm^2)	> 0	> 1	> 2	> 3	> 4	> 5
n (%)	2157 (41.4%)	579 (11.1%)	136 (2.6%)	39 (0.7%)	14 (0.3%)	3 (0.1%)

The relationship between binary plaque CSA response (progression or regression) from baseline to followup and baseline predictors (plaque burden, plaque CSA, adventitia CSA, etc.) was presented in Table 3.3 through mixed-effect logistic regression. As shown, plaque CSA developing direction is negatively associated with baseline plaque burden, plaque CSA and fibrous CSA. In other words, statin treatment would lead to plaque regression at vessel sites of greater plaque burden, greater plaque CSA and greater fibrous CSA. Further analysis specified that compared to vessel frames undergoing plaque progression at followup, frames undergoing plaque regression ini-

tially had 3.47% ± 0.34% greater plaque burden, 0.82 ± 0.07 mm^2 greater plaque CSA and 0.40 ± 0.03 mm^2 greater fibrous area. All p-values were $\ll 0.001$. In fact, risk ratio of plaque regression occurring for frames with baseline plaque burden $> 50\%$, plaque CSA $> 8mm^2$ or fibrous area $> 2.5mm^2$ were 1.29 (CI: 1.24 to 1.35, p $\ll 0.001$), 1.29 (CI: 1.24 to 1.35, p $\ll 0.001$) and 1.40 (CI: 1.34 to 1.46, p $\ll 0.001$) respectively.

Table 3.3: Mixed-effect logistic regression between binary plaque/adventitia CSA followup response direction and baseline predictors

	Plaque CSA Response direction			**Adventitia CSA Response direction**		
	β	95% CI	p-value	β	95% CI	p-value
Baseline predictors:						
Plaque burden (%)	-0.03	-0.036 to -0.024	< **0.001**	-0.02	-0.024 to -0.011	< **0.001**
Eccentricity	0.20	-0.276 to 0.672	0.41	0.62	0.122 to 1.126	**0.01**
TCFA	0.08	-0.130 to 0.297	0.44	0.12	-0.095 to 0.344	0.26
Adventitia CSA (mm^2)	0.01	-0.013 to 0.031	0.44	-0.01	-0.030 to 0.016	0.55
Plaque CSA (mm^2)	-0.18	-0.215 to -0.144	< **0.001**	-0.12	-0.162 to -0.088	< **0.001**
Fibrofatty CSA (mm^2)	0.18	-0.022 to 0.378	0.08	0.18	-0.032 to 0.391	0.10
Fibrous CSA (mm^2)	-0.37	-0.464 to -0.276	< **0.001**	-0.37	-0.464 to -0.267	< **0.001**
Dense calcium CSA (mm^2)	0.15	-0.060 to 0.355	0.16	0.01	-0.196 to 0.219	0.91
Necrotic core (mm^2)	-0.15	-0.314 to 0.021	0.09	0.10	-0.061 to 0.269	0.22

*TCFA indicates thin-cap fibroatheroma.

*For binary response direction, "0" means regression while "1" means progression.

Patient-level analysis: Plaque regression percentage for each patient was defined as number of frames experiencing plaque CSA decrease at followup divided by the length of whole pullback. Thus, plaque progression % per patient simply equaled to (100% - plaque regression %). In result, plaque regression % for all 61 patients had a mean value of 58.2% (± 25.1%). Based on multivariate regression related to patients biomarkers, plaque regression % per patient was negatively associated with patient smoking history and diabetes mellitus status. More specifically, patients smoking in past had significantly less plaque regression % than patients not smoking

in past (52.5% ± 26.0% vs. 67.0% ± 21.1%, p = 0.02); similarly, diabetes patients had significantly less plaque regression % than non-diabetes patients (40.4% ± 27.2% vs. 65.1% ± 20.7%, p < 0.01). On the contrary, plaque regression % per patient was further proved to be positively associated with baseline high density lipoprotein (HDL) level (R = 0.31, p = 0.01) and baseline apolipoprotein A1 (ApoA1) level (R = 0.31, p = 0.02).

3.3.2 Magnitude of plaque development

Frame-level analysis: According to plaque regression % per patient, different segments of the same artery had different plaque CSA developing directions during statin treatment. To better analyze plaque CSA magnitude changes, we divided all frames (n=5215) into two groups – plaque regression (n=2157) and plaque progression (n=3058) based on plaque CSA developing direction.

The relative magnitude changes were used and defined as (baseline CSA - followup CSA) / baseline CSA. Relative Δplaque CSA in plaque progression group was 14.4% ± 18.2% from baseline to followup while relative Δplaque CSA in plaque regression group was -13.4% ± 11.4 %. Mixed-effect model presented that the unsigned changes of plaque CSA were significantly different between these two groups ($p \ll 0.01$).

The relationship between unsigned Δplaque CSA and baseline predictors including frame morphology and plaque composition was investigated through mixed-effect linear regression. Table 3.4 presented the results for plaque progression group. As shown, if plaque progression happened, plaque CSA increasing magnitude was negatively associated with baseline plaque burden, plaque CSA and fibrous area, and was positively associated with baseline eccentricity, adventitia CSA. That was to say that if progression happened, statin treatment would slow down the plaque CSA increasing rate at vessel sites of greater plaque burden, plaque CSA and fibrous area, but accelerate the increasing rate at vessel sites of more eccentric plaque distribution and greater adventitia CSA. Table 3.5 presented the results for plaque regression

group. Conversely, if plaque regression happened, unsigned plaque CSA decreasing magnitude was positively associated with baseline plaque burden, plaque CSA, and fibrous.

From baseline to followup, plaque progression group experienced averaged 0.35 mm^2 Δfibrous, 0.18 mm^2 Δfibrofatty, -0.01 mm^2 Δnecrotic core and -0.02 mm^2 Δdense calcium. Meanwhile, plaque regression group experienced averaged -0.34 mm^2 Δfibrous, -0.08 mm^2 Δfibrofatty, -0.23 mm^2 Δnecrotic core and -0.05 mm^2 Δdense calcium. As observed, fibrous changed dramatically at the same direction of plaque development on both cases; necrotic core didn't contribute to plaque progression at all but underwent second most changes in plaque regression group.

Table 3.4: Mixed-effect linear regression between Δplaque/Δadventitia progression CSA (%) and baseline predictors

	Plaque CSA Progression magnitude (%)			**Adventitia CSA Progression magnitude (%)**		
	β	95% CI	p-value	β	95% CI	p-value
Baseline predictors:						
Plaque burden (%)	-0.23	-0.294 to -0.169	< **0.001**	0.04	0.012 to 0.072	**0.01**
Eccentricity	18.63	13.750 to 23.502	< **0.001**	-1.11	-3.556 to 1.331	0.37
Adventitia CSA (mm^2)	0.24	0.011 to 0.474	**0.04**	-0.36	-0.475 to -0.253	< **0.001**
Plaque CSA (mm^2)	-1.35	-1.729 to -0.978	< **0.001**	0.12	-0.065 to 0.299	0.21
Fibrofatty CSA (mm^2)	0.30	-1.938 to 2.542	0.79	2.86	1.832 to 3.893	< **0.001**
Fibrous CSA (mm^2)	-2.32	-3.406 to -1.242	< **0.001**	-0.98	-1.466 to -0.497	< **0.001**
Dense calcium CSA (mm^2)	-0.57	-2.816 to 1.669	0.62	0.51	-0.448 to 1.461	0.30
Necrotic core CSA (mm^2)	0.07	-1.964 to 2.106	0.95	-0.09	-0.909 to 0.730	0.83

Patient-level analysis: Plaque progression magnitude for each patient was defined as the average of frame-based plaque progression magnitude per patient. Plaque regression magnitude for each patient was defined similarly. In result, plaque progression magnitude for 61 patients was 11.4% ± 7.8% while unsigned plaque regression magnitude was 11.4% ± 7.1%. Based on multivariate regression analysis related to

Table 3.5: Mixed-effect linear regression between unsigned Δplaque/Δadventitia regression CSA (%) and baseline predictors

	Plaque CSA Regression magnitude (%)			**Adventitia CSA Regression magnitude (%)**		
	β	95% CI	p-value	β	95% CI	p-value
Baseline predictors:						
Plaque burden (%)	0.05	0.017 to 0.074	**0.002**	0.05	0.041 to 0.066	< **0.001**
Eccentricity	-1.71	-4.034 to 0.610	0.15	-0.18	-1.191 to 0.831	0.73
Adventitia CSA (mm^2)	-0.01	-0.117 to 0.094	0.84	-0.17	-0.220 to -0.121	< **0.001**
Plaque CSA (mm^2)	0.39	0.227 to 0.559	< **0.001**	0.30	0.231 to 0.375	< **0.001**
Fibrofatty CSA (mm^2)	0.35	-0.559 to 1.260	0.45	1.11	0.686 to 1.531	< **0.001**
Fibrous CSA (mm^2)	0.87	0.487 to 1.257	< **0.001**	-0.00	-0.177 to 0.175	0.99
Dense calcium CSA (mm^2)	-0.08	-1.026 to 0.875	0.88	-0.03	-0.489 to 0.439	0.92
Necrotic core CSA (mm^2)	-0.08	-0.754 to 0.597	0.82	0.33	-0.001 to 0.655	0.05

patients biomarkers, patient-based plaque progression magnitude was positively correlated with beta blockers usage (12.7% ± 8.3% vs. 8.0% ± 5.2%, p = 0.01) and apolopoprotein B (ApoB) level (R = 0.60, p ≪ 0.001) and negatively correlated with total cholesterol level (R = -0.32, p = 0.01). Unsigned plaque regression magnitude was positively correlated with ApoA1 level (R = 0.28, p = 0.038) and negatively correlated with diabetes status (7.8% ± 5.0% vs. 12.8% ± 7.4%, p = 0.004).

3.3.3 Direction of adventitia development

Frame-level analysis: 61.1% of all frames underwent decreasing adventitia CSA from baseline to followup while 38.9% underwent increasing. A closer inspection about relationship between adventitia and plaque CSA development was shown in Table 3.6. It appeared that majority of frames (48.2% and 28.5%) experienced adventitia CSA changes in the "same" direction of plaque CSA changes (p ≪ 0.001). As shown in Table 3.3, adventitia and plaque CSA response direction shared the same negative baseline predictors – plaque burden, plaque area and fibrous area. Besides, adventitia CSA response direction had a positive predictors – eccentricity. Therefore, frames with more eccentric plaque distribution was more likely to get adventitia CSA

progression at followup.

Patient-level analysis: Adventitia regression percentage for each patient was defined as number of frames experiencing adventitia CSA decrease at followup divided by the length of whole pullback. Adventitia regression percentage and plaque regression percentage (defined previously) for all patients were positively correlated (R=0.76, $p \ll 0.001$) as displayed in Figure 3.3. Mixed-effect regression related to patients biomarkers proved that diabetes patients had less adventitia regression percentage than non-diabetes patients (44.0% ± 27.6% vs. 67.1% ± 25.9%, p = 0.006).

Table 3.6: Directional relationship between baseline-to-followup Δadventitia area and Δplaque area

	Adventitia regression n (%)	Adventitia progression n (%)
Plaque regression	2515 (48.2%)	543 (10.4%)
Plaque progression	670 (12.8%)	1487 (28.5%)
Chi-squared Test	**$p \ll 0.001$**	

3.3.4 Magnitude of adventitia development

Frame-level analysis: Besides the development direction, the magnitude of Δadventitia CSA is important to quantitatively assess the remodeling process. Relative magnitude over baseline value was used here. Magnitude development relationship between adventitia and plaque CSA was investigated by linear mixed regression. If plaque and adventitia CSA developed at the same direction:

- Unsigned adventitia CSA regression magnitude (8.1% ± 8.6%) was positively associated with unsigned plaque CSA regression magnitude ($\beta = 0.21, p \ll 0.001$).
- Adventitia CSA progression magnitude (9.6% ± 12.0%) was positively associ-

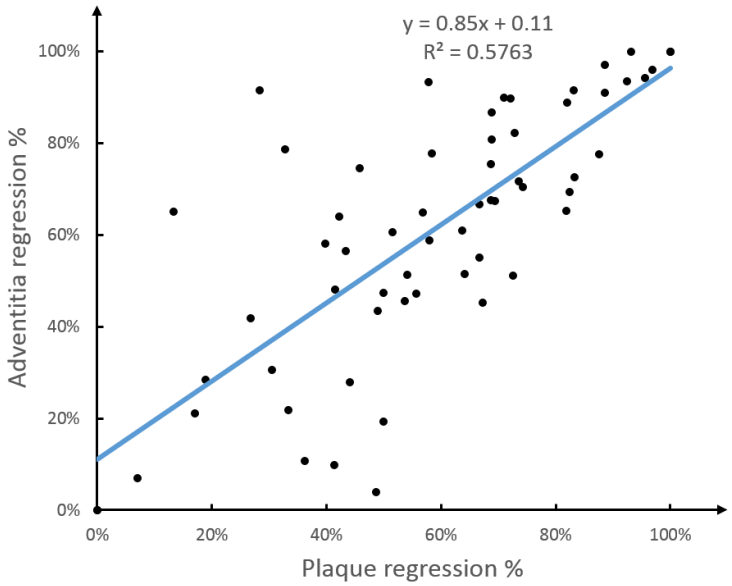

Figure 3.3: Correlation between patient-based adventitia regression % and plaque regression %. Just as its name implies, adventitia regression % per patient is defined as the percentage of frames experiencing adventitia CSA decrease at followup along whole pullback. Plaque regression % is defined in a similar pattern.

ated with plaque CSA progression magnitude ($\beta = 0.29, p \ll 0.001$).

If plaque and adventitia CSA developed at the opposite direction:

- Unsigned Adventitia CSA regression magnitude (3.9% $\pm$ 3.5%) was slightly associated with plaque CSA progression magnitude ($\beta = 0.02, p = 0.01$).
- Adventitia CSA progression magnitude (5.1% $\pm$ 7.4%) was not associated with plaque CSA regression magnitude (p = 0.17).

Table 3.4 and Table 3.5 displayed baseline predictors associated with adventitia progression CSA and regression CSA respectively. Note that baseline plaque burden and adventitia CSA had different influence on plaque and adventitia progression: statin treatment would slow down Δplaque progression and speed up Δadventitia progression for frames with greater baseline plaque burden and less baseline adventitia CSA.

Patient-level analysis: Adventitia progression magnitude for each patient was defined as the average of frame-based adventitia progression magnitude per patient. Adventitia regression magnitude was calculated as well. Adventitia and plaque development magnitude for all patients were positively correlated as displayed in Figure 3.4. Based on multivariate regression related to patients biomarkers, patient-based adventitia progression magnitude was positively correlated with ApoB level ($R = 0.35$, $p = 0.01$). Meanwhile, unsigned adventitia regression magnitude was positively correlated with LDL level ($R = 0.32$, $p = 0.01$).

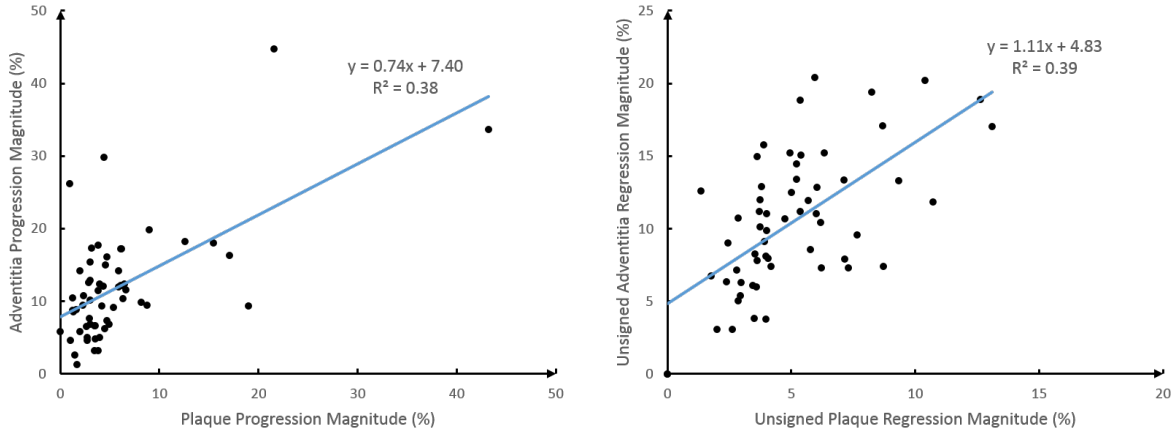

Figure 3.4: Correlation between patient-based adventitia development magnitude and plaque development magnitude. Relative magnitude (%) is used here and defined as ΔCSA from baseline to followup over baseline CSA.

3.4 Discussion

Previous serial VH-IVUS analysis [22, 41, 43] showed that statin treatments were associated with plaque volume changes and plaque components development at non-culprit/culprit lesions. However, lesions may not represent the distinguishing morphological characteristics of whole vessel. Prevalence and morphological presentation of arterial remodeling may differ depending on vessel location [47, 76]. Pasterkamp

et al. [47] stated that The mechanisms that underlie the direction of arterial remodeling was still unclear. In this randomised study, we are trying to provide reliable assessment of statin effects on direction and magnitude of arterial remodeling. And the predictive analysis further proved relationship between followup remodeling process and initial baseline morphological and biomedical characteristics. We aimed to minimized system errors due to subjective selection of target sites and reference sites. Therefore, instead of applying traditional remodeling index, we analyzed the overall development of plaque area and corresponding response of adventitia area over the whole pullback.

Observations shown in Table 3.1 help to demonstrate the expected statin effects on relative reductions of total and LDL cholesterol (18.9% and 22.5% respectively). As illustrated in Table 3.2, plaque-stabilizing therapy with statin lead to plaque regression at 58.6% of included vessel frames. It is further proved by multivariate regression that the response direction of followup plaque area is associated with baseline plaque burden, plaque CSA and fibrous CSA. More specifically, plaque regression risk ratio during statin treatment for frames with baseline plaque burden $> 50\%$, plaque CSA $> 8mm^2$ or fibrous area $> 2.5mm^2$ are 1.29, 1.29 and 1.40 respectively. It is shown in [29] and Chapter 4 that pathologic intima thickening plaque phenotypes which contain the most fibrous area exhibited the most significant followup changes of plaque morphology. Following from this premise, our results indicate that statin treatment mainly works on advanced vessel of large plaque volume and flexible vessel of large fibrous area. In addition, plaque development magnitude analysis provides consistent observations: such advanced and flexible vessels would have less plaque increasing area if plaque progression happened and more decreasing area if regression happened.

As for plaque composition, fibrous changed dramatically in the same direction of plaque development in both regression and progression groups, which have confirmed flexibility of fibrous tissue during lipid-lowering treatment. Meanwhile, statin

treatment suspended necrotic core advancement in plaque progression group and activated necrotic core shrinkage in plaque regression group. In comparison to previous lesion studies, Hong et al. reported significant decrease in necrotic core volume under statin treatment [22] while Nasu et al. reported unchanged necrotic core volume during followup period [41]. Beside diversity of patient population and variations of statin usage, our findings about different responses of necrotic core to statin medication regarding different plaque development may be another explanation for previous paradoxical results.

Several biomarkers including smoking history, diabetes mellitus and baseline HDL level are found as predictors for plaque response direction. Patients smoking in past or with diabetes have significantly less plaque regression % over the whole pullback while plaque regression % is proved to be positively associated with baseline HDL level ($R = 0.31$, $p = 0.01$) and baseline ApoA1 level ($R = 0.31$, $p = 0.02$). This result is in a good agreement with previous studies [1, 38, 52] suggesting that cigarette smoking and diabetes mellitus continues to be a health hazard during lipid-lowering therapy and would slightly offset statin effect of plaque stabilization. On the other hand, the result also implies that initially high level of HDL and ApoA1 would promote statin effect on plaque regression and contribute to cardiovascular benefits as demonstrated in Tani et al. study [59]. Similar correlations are observed in plaque magnitude development analysis. Unsigned plaque regression magnitude was positively correlated with ApoA1 level ($R = 0.28$, $p = 0.038$) and negatively correlated with diabetes status ($7.8\% \pm 5.0\%$ vs. $12.8\% \pm 7.4\%$, $p = 0.004$). On the contrary, ApoB level were positively associated with plaque progression magnitude. Beta blocker usage which indirectly indicates the advanced severity of coronary disease [14] was also proved to be positively associated with plaque progression. This may reflect inevitability of plaque progression process once the disease has developed into a critical stage.

The essence of coronary remodeling is adventitia area corresponding response

to atherosclerotic plaque development. In our case, 76.7% of 5215 cross-sectional IVUS-VH frames (48.2% regression and 28.5% progression) experienced adventitia CSA changes in the same direction of plaque CSA changes. Multivariate regression analysis further confirm that adventitia followup response direction shares with plaque followup response the same negative baseline predictors – plaque burden, plaque area and fibrous area. Frame-based changing magnitude analysis also presents significant association between adventitia and plaque CSA if they develop in the same direction. Moreover, adventitia regression % for each patient is significantly correlated with plaque regression % (R = 0.76, $p \ll 0.001$); adventitia regression magnitude for each patient is also significantly correlated with plaque regression magnitude (R = 0.85, $p \ll 0.001$). Our results provide a potential implication that coronary remodeling is more of a plaque-intrigued, adventitia-followed process. Because plaque development is the leading cause here, ApoB level is not only positively correlated with plaque progression (R = 0.60, p $\ll$ 0.001) but also with adventitia progression (R = 0.35, p = 0.01). In like manner, this explains why diabetes patients have not only less plaque regression % but also less adventitia regression % over the whole pullback for each patient.

There are still dissociation between plaque and adventitia development. Beside shared predictors and plaque area development itself, adventitia CSA response direction has a unique baseline predictors – eccentricity. In other words, vessel expansion tends to appear at sites of more eccentric plaque distribution, which is in line with previous studies [62,67]. Furthermore, as shown in Table 3.4, baseline plaque burden along with initial adventitia CSA status has opposite influence on plaque and adventitia progression magnitude: statin treatment would slow down Δplaque progression and speed up Δadventitia progression for frames with less baseline adventitia CSA and greater baseline plaque burden. To be more specific, even though plaque and adventitia tend to develop at the same direction, they don't progress at the same pace:

adventitia progression magnitude is promoted while plaque progression magnitude is repressed at relatively small but advanced atherosclerotic vessel sites. And we can speculate that this process would efficiently prevent luminal narrowing in such vessel sites. However, it is also postulated that there is a higher risk of rupture in vessel of eccentric plaque distribution and greater plaque burden. There findings support the association between positive remodeling and plaque vulnerability and justify why plaque rupture frequently occurs with mild arterial stenosis.

Patient-based analysis shows that there are mixed plaque progression and regression frames with the same patient. Adventitia corresponding response to plaque growth or shrinkage shows a great deal of varieties as well for each patient. Both together clearly demonstrate that statin effect on plaque and adventitia development is location specific and determined by initial vessel morphology and composition in conjunction with patient biomedical conditions and clinical characteristics. This observation of heterogeneity of coronary remodeling among individuals patterns itself upon previous studies [39, 76].

3.5 Study limitations

Present study includes patients in a relatively early stage. Thus, the relationship between statin medication and prevention of major adverse cardiac events are not investigated due to lack of clinical events. Our findings related to lipid-lowering treatment may not reflect the natural history of atherosclerosis disease.

3.6 Conclusion

In summary, our comprehensive serial study indicates that statin treatment leads to plaque regression at most vessel sites but its effect varies among individual patients and is associated with vessel location-specific characteristics and patient clinical status. We also find that lipid-lowering treatment primarily works on advanced vessel of large plaque volume and flexible vessel of large fibrous area by promoting plaque

regression and shrinking necrotic core area. Moreover, arterial remodeling is proved to be a plaque-intrigued adventitia-followed process. While adventitia development is destined to follow the plaque developing direction, positive remodeling with less plaque changing magnitude and greater adventitia changing magnitude can be expected at small and advanced vessel sites. As far as we know, this is the first in vivo serial study that investigates coronary remodeling on both segmental and patient levels in terms of both changing the remodeling direction and changing the remodeling extent to reflect the truly dynamic nature of artery wall development under lipid-lowering medication.

CHAPTER 4
NOVEL QUANTITATIVE APPROACHES ASSESSING PLAQUE PHENOTYPE SERIAL PROGRESSION BASED ON INTRAVASCULAR ULTRASOUND

In this chapter, coronary plaque morphological development of different phenotypes has been evaluated comprehensively based on baseline and 1-year followup serial study using computer aided intravascular ultrasound imaging analysis (published at [29]).

4.1 Introduction

Recall that virtual histology (IVUS-VH) has been developed to assess plaque composition by processing raw radiofrequency signal from intravascular ultrasound (IVUS) and distinguish four plaque types (fibrous tissue F, fibro-fatty tissue FF, necrotic tissue NC and dense calcification DC). To better understand coronary plaque development, a comprehensive morphological classification scheme is widely used to categorize the lesions on the basis of plaque composition. These categories include no-lesion, pathologic intima thickening (PIT), fibrous plaque (FP), fibrocalcified plaque (FcP), thick-cap fibroatheroma (ThCFA) and thin-cap fibroatheroma (TCFA) and can be determined by IVUS-VH images. They correspond to the sequence of evolution of atherosclerotic lesions described by American Heart Associations Committee [55]. Previously most of efforts in this field are consumed by analyzing fibroatheroma including TCFA and ThCFA, which are believed to be predictive risk factors for cardiac events, while other phenotypes are buried in oblivion as being considered stable [31, 56]. Recent studies [11, 49] reported that plaques with PIT phenotype also developed greater progression and were more likely to transform into fibroatheroma. In this chapter, baseline to 1-year followup serial development of different plaque phenotypes are examined in patients with stable coronary disease.

4.2 Method

4.2.1 Patient population

This study shares the same patient cohort with previous study described in Chapter 3. IVUS-VH image pullbacks from 61 patients were taken from the database of serial IVUS studies of patients with stable coronary artery disease enrolled at the Charles University Hospital, Prague, and were selected according to the inclusion criteria [30]. After the initial enrollment and baseline imaging, a repeat IVUS-VH examination of the same vessel segment is performed after 1-year treatment for each patient. 25 mm long mutual overlap between baseline and followup pullbacks are prerequisite. All of them received statin treatment after enrollment (45 of them received aggressive treatment).

4.2.2 Image segmentation, registration and segmental analysis

IVUS image acquisition and segmentation along with baseline-followup registration was performed following the same protocol as Chapter 3. After image processing, frame-based morphological and compositional features were computed. Each pullback was then divided into continuous 5mm baseline/followup registered vessel segments by averaging the frame-based quantitative characteristics. 5mm vessel segment was introduced here to be more representative of plaque development and less susceptible to local variations (noise) compared to vessel frame. Segmental analysis would compensate for small registration errors as well. Vessel and plaque measurement morphologic indices included: external adventitia cross-sectional area (CSA), lumen CSA, plaque burden PB ($adventitia\ CSA - lumen\ CSA/adventitia\ CSA$), eccentricity ($max.\ plaque\ thickness - min.\ plaque\ thickness)/max.\ plaque\ thickness$).

4.2.3 Plaque phenotype classification scheme

Morphological classification scheme used to categorize the lesions on the basis of plaque burden and plaque composition is shown in Figure 4.1. Here are pathological

explanations of 6 atherosclerosis phenotypes:

- **No lesion:** represents all frames of $< 40\%$ plaque burden.
- **PIT:** was first introduced by Virmani et al. [65] to indicate an early-stage preatherosclerotic coronary lesion, which consists mainly of fibrofatty tissues and has no apparent necrosis and calcium.
- **FP:** is similar to PIT but has less fibrofatty tissues.
- **FcP:** is fibrous plaque that has large portion of dense calcium and may also contain a small mount of necrotic core. Dense calcium is frequently observed at advanced stage of plaque and therefore, represents a late stage of atherosclerosis.
- **ThCFA & TCFA:** are both fibroatheromas that contain lots of confluent necrotic core abutting the lumen. The difference is, compared to ThCFA, TCFA usually has a diffuse necrotic core distribution, which implies a prone-to-rupture thin cap near the lumen.

Examples of 6 phenotypes from our patient population were listed in Figure 4.2, where the VH images are color coded as red (NC), white (DC), light green (FF), and dark green (F). Each vessel frame was categorized into one of 6 phenotypes and 5mm segment phenotype was determined by the most severe frame within it in order of TCFA, ThCFA, PIT, FcP, FP and no-lesion.

4.2.4 Statistical analysis

Mean values $\pm$ standard deviations were calculated for all numerical variables while median with interquartile range was used if necessary. Mixed-effect ANOVA was used to correct for morphological comparison such as plaque area change by designating patient as random effect. As for 6-level plaque phenotype comparison, we focused on serial change from baseline to followup for each phenotype instead of

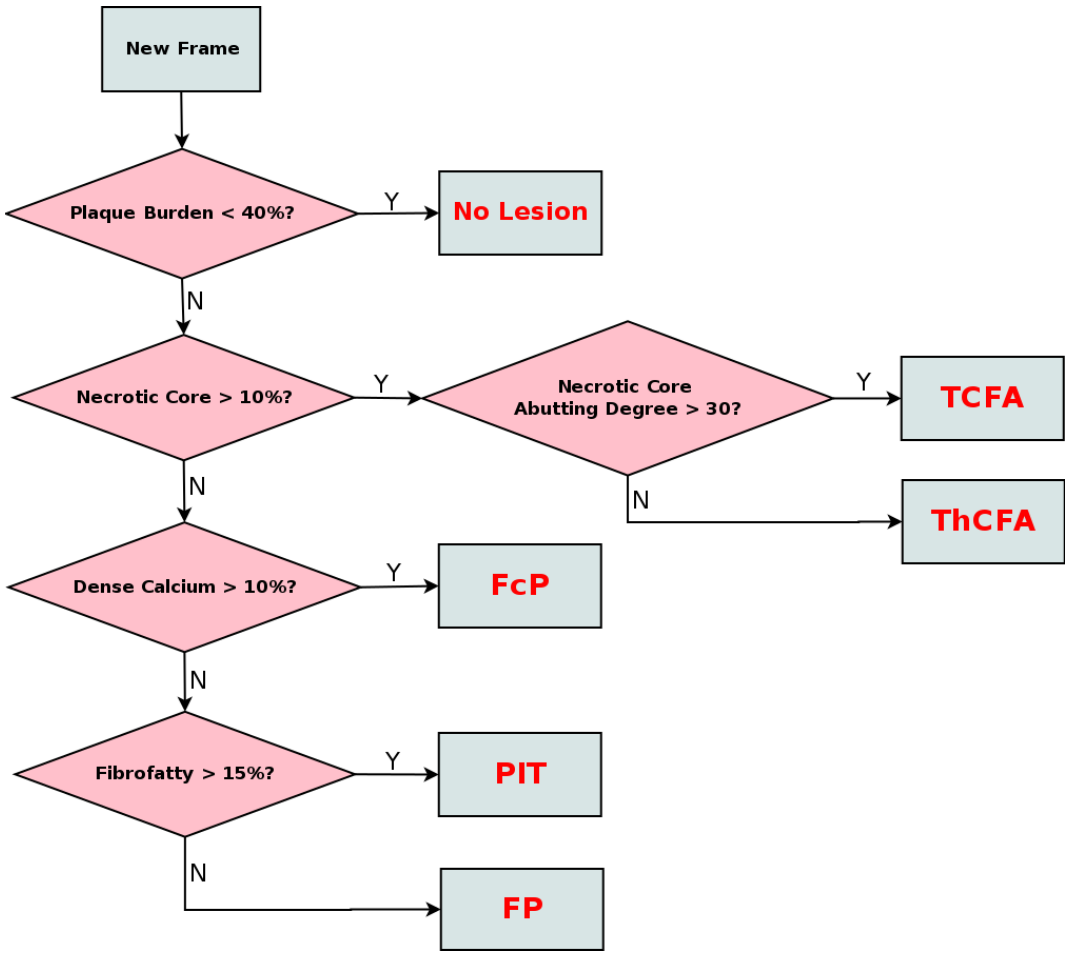

Figure 4.1: **Plaque phenotypes classification scheme.** PIT, pathologic intimal thickening; FcP, fibrocalcified plaque; FP, fibrous plaque; TCFA, thin cap fibroatheroma; ThCFA, thick cap fibroatheroma.

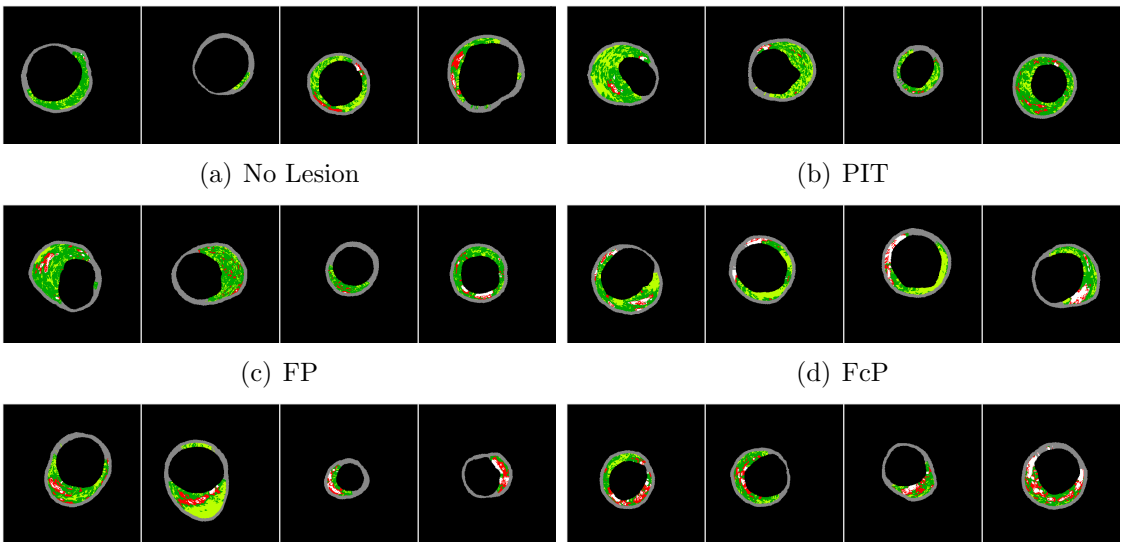

(a) No Lesion (b) PIT

(c) FP (d) FcP

(e) ThCFA (f) TCFA

Figure 4.2: **Plaque phenotypes VH examples.**

comparing different phenotypes directly. In this case, mixed model was used for each phenotype analysis. For categorical variables, contingency tables were used to display frequency distributions. Statistical significance was calculated by Fisher's exact test.

4.3 Results

Total of 693 5mm longitudinal vessel segments from 61 pullbacks were matched and analyzed from baseline to followup.

4.3.1 Morphological changes in phenotypes

Among 693 segments, there are 317 TCFA segments (45.7%), 65 ThCFA segments (9.4%), 49 FP segments (7.1%), 89 PIT segments and 170 segment without lesion (24.5%). Morphological development for all plaque phenotypes was shown in Table 4.1. TCFA segments experienced significant decrease of plaque burden while both PIT and FP segments demonstrated plaque CSA decrease. A significant negative remodeling defined as -0.97 $\pm$ 1.91 mm regression of adventitia area is found in PIT segments as well.

Table 4.1: Morphological development for all phenotypes.

	No.Lesion	PIT	FP	FcP	ThCFA	TCFA
Number of vessel segments	170	89	49	3	65	317
BL plaque burden	0.29 ± 0.07	0.45 ± 0.08	0.50 ± 0.09	0.46 ± 0.02	0.46 ± 0.09	0.52 ± 0.09
FU plaque burden	0.30 ± 0.08	0.44 ± 0.09	0.47 ± 0.10	0.46 ± 0.05	0.46 ± 0.09	0.50 ± 0.10
ΔPlaque burden	0.00 ± 0.05	-0.01 ± 0.05	-0.03 ± 0.04	0.01 ± 0.04	0.00 ± 0.04	-0.01 ± 0.05
p-value	0.545	0.493	0.116	0.75	0.941	**0.035**
BL lumen CSA (mm^2)	11.39 ± 4.63	10.17 ± 3.48	7.64 ± 3.14	7.47 ± 2.64	8.10 ± 2.67	7.94 ± 3.19
FU lumen CSA (mm^2)	11.13 ± 4.62	9.77 ± 3.30	7.64 ± 3.14	7.41 ± 2.59	7.98 ± 2.60	8.09 ± 3.23
ΔLumen CSA (mm^2)	-0.26 ± 1.60	-0.40 ± 1.13	0.00 ± 1.33	-0.06 ± 0.21	-0.12 ± 0.81	0.15 ± 0.95
p-value	0.324	0.171	0.997	0.964	0.688	0.445
BL adventitia CSA (mm^2)	16.09 ± 6.29	18.68 ± 5.92	15.22 ± 5.48	13.64 ± 4.39	14.99 ± 4.62	16.37 ± 5.26
FU adventitia CSA (mm^2)	15.80 ± 6.18	17.71 ± 5.50	14.43 ± 4.75	13.91 ± 4.65	14.72 ± 4.23	16.24 ± 5.25
ΔAdventitia CSA (mm^2)	-0.29 ± 1.96	-0.97 ± 1.91	-0.78 ± 2.81	0.27 ± 0.56	-0.27 ± 0.99	-0.13 ± 1.33
p-value	0.38	**0.003**	0.234	0.853	0.429	0.633
BL plaque CSA (mm^2)	4.71 ± 2.28	8.51 ± 3.26	7.58 ± 2.85	6.17 ± 1.80	6.89 ± 2.66	8.44 ± 2.96
FU plaque CSA (mm^2)	4.67 ± 2.20	7.94 ± 3.06	6.79 ± 2.37	6.49 ± 2.32	6.74 ± 2.40	8.15 ± 2.98
ΔPlaque CSA (mm^2)	-0.04 ± 0.98	-0.57 ± 1.34	-0.78 ± 1.81	0.32 ± 0.77	-0.15 ± 0.83	-0.29 ± 1.07
p-value	0.771	**0.019**	**0.025**	0.4	0.511	0.077
BL eccentricity	0.66 ± 0.17	0.65 ± 0.15	0.70 ± 0.14	0.73 ± 0.19	0.78 ± 0.13	0.71 ± 0.15
FU eccentricity	0.66 ± 0.15	0.63 ± 0.16	0.67 ± 0.15	0.70 ± 0.24	0.78 ± 0.14	0.72 ± 0.15
ΔEccentricity	-0.00 ± 0.14	-0.02 ± 0.09	-0.03 ± 0.07	-0.02 ± 0.06	0.00 ± 0.08	0.02 ± 0.08
p-value	0.861	0.325	0.077	0.565	0.77	0.076

* BL, baseline; FU, followup; CSA, cross-sectional area.
* PIT, pathologic intimal thickening; FcP, fibrocalcified plaque; FP, fibrous plaque; TCFA, thin cap fibroatheroma; ThCFA, thick cap fibroatheroma.
* Significant p-values are highlighted as boldface.

4.3.2 Compositional changes in phenotypes

Relative changes of plaque composition was shown in Figure 4.3. FcP segments were not listed due to small segment count (n=3). Relative changes were computed as $(followup\ value - baseline\ value)/followup\ value$. Both baseline PIT and FP segments exhibited significant progression of necrotic cores and dense calcium, which are considered as advanced plaque components. The massive decrease of fibrous tissues in PIT and FP segments was corresponding to above-mentioned significant regression of plaque CSA in both phenotypes. In contrast, TCFA and ThCFA had opposite changes of plaque tissues. Angular range of necrotic core abutting the lumen in a frame is one of criterion for IVUS-VH-derived TCFA definition and indicates the severity of atherosclerosis as demonstrated in Chapter 2. Its serial changes for all phenotypes were displayed in Figure 4.4. Similarly, both PIT and FP segments exhibited significant increase of abutting angles (+22.0°and +17.9°) while TCFA segments exhibited opposite changes of abutting angles (-15.1°).

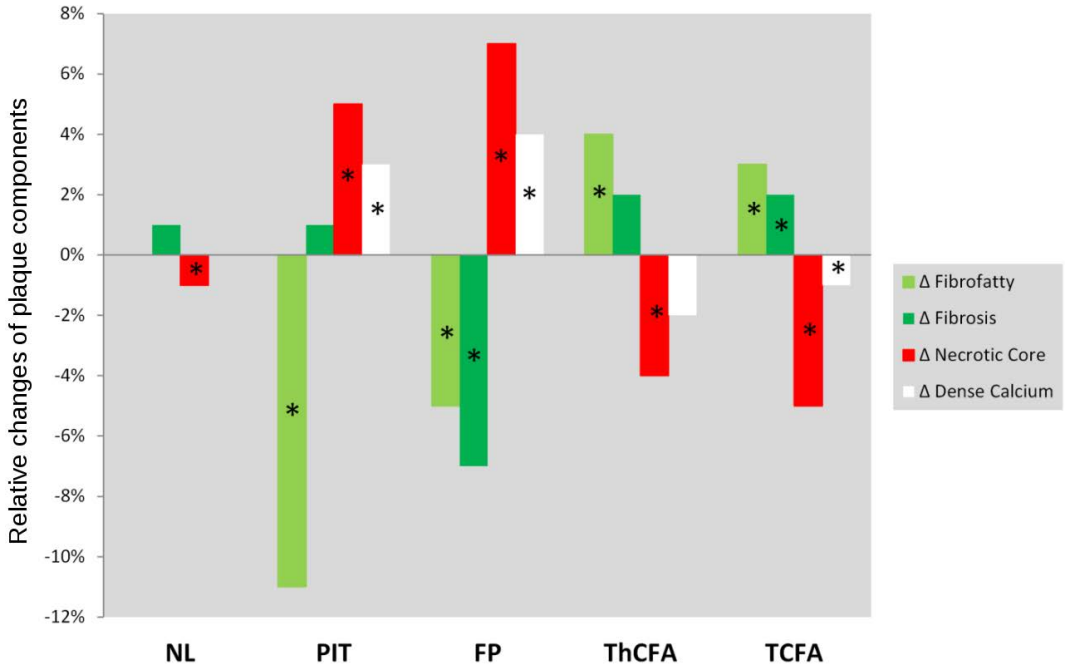

Figure 4.3: **Relative compositional changes for all baseline phenotypes.** Significant changes were marked by asterisk.

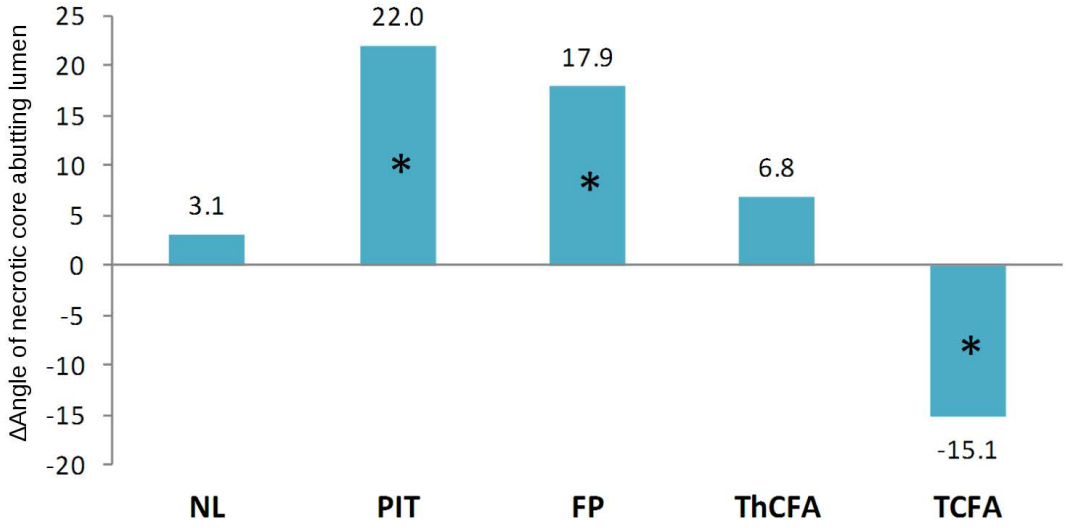

Figure 4.4: **Angular changes of necrotic core touching lumen for all baseline phenotypes.** Significant changes were marked by asterisk.

4.3.3 Phenotype transition

Phenotype transition from baseline to followup was presented in Table 4.2. PIT and FP were the most dynamic phenotypes as 91.8% of PIT segments and 75.5% of FP segments transformed into other phenotypes in followup. Meanwhile, no-lesion and TCFA were the most passive phenotypes as 81.8% of no-lesion and 73.5% of TCFA segments kept unchanged. Further analysis of followup TCFA segment sources (Figure 4.5) proved that PIT made the biggest contrition to emerging TCFA in followup.

For patient-based analysis, phenotype % was defined as the proportion of specific phenotype segment over the whole pullback. For example, the PIT% for all 61 patients increased from baseline 12.3% ± 18.3% to followup 18.3% to 10.8%. Serial changes of each phenotype % was then correlated with lipid-lowering treatment as shown in Table 4.3. As you see, 18% reduction of PIT% accompanied 20% growth of TCFA% during standard treatment, implying the transition between two phenotypes. On the contrary, aggressive treatment stabilized both PIT and TCFA segments. As a result, some example images showing transition from PIT to TCFA were displayed in Figure 4.6.

Table 4.2: **Phenotype transition from baseline to followup**. Segment numbers (n) and percentage (%) of transformed phenotypes were presented for each baseline phenotype.

	TCFA, n(%)	ThCFA, n(%)	FcP, n(%)	FP, n(%)	PIT, n(%)	No lesion, n(%)
Baseline, n	317	65	3	49	89	170
Followup TCFA	233 (73.5%)	28 (43.1%)	2 (66.7%)	25 (51.0%)	37 (41.6%)	11 (6.5%)
Followup ThCFA	50 (15.8%)	25 (38.5%)	0 (0.0%)	5 (10.2%)	5 (5.6%)	12 (7.1%)
Followup FcP	4 (1.3%)	0 (0.0%)	0 (0.0%)	3 (6.1%)	4 (4.5%)	0 (0.0%)
Followup FP	6 (1.9%)	2 (3.1%)	0 (0.0%)	12 (24.5%)	21 (23.6%)	2 (1.2%)
Followup PIT	24 (7.6%)	10 (15.4%)	1 (33.3%)	4 (8.2%)	22 (24.7%)	6 (3.5%)
Followup No lesion	0 (0.0%)	0 (0.0%)	0 (0.0%)	0 (0.0%)	0 (0.0%)	139 (81.8%)

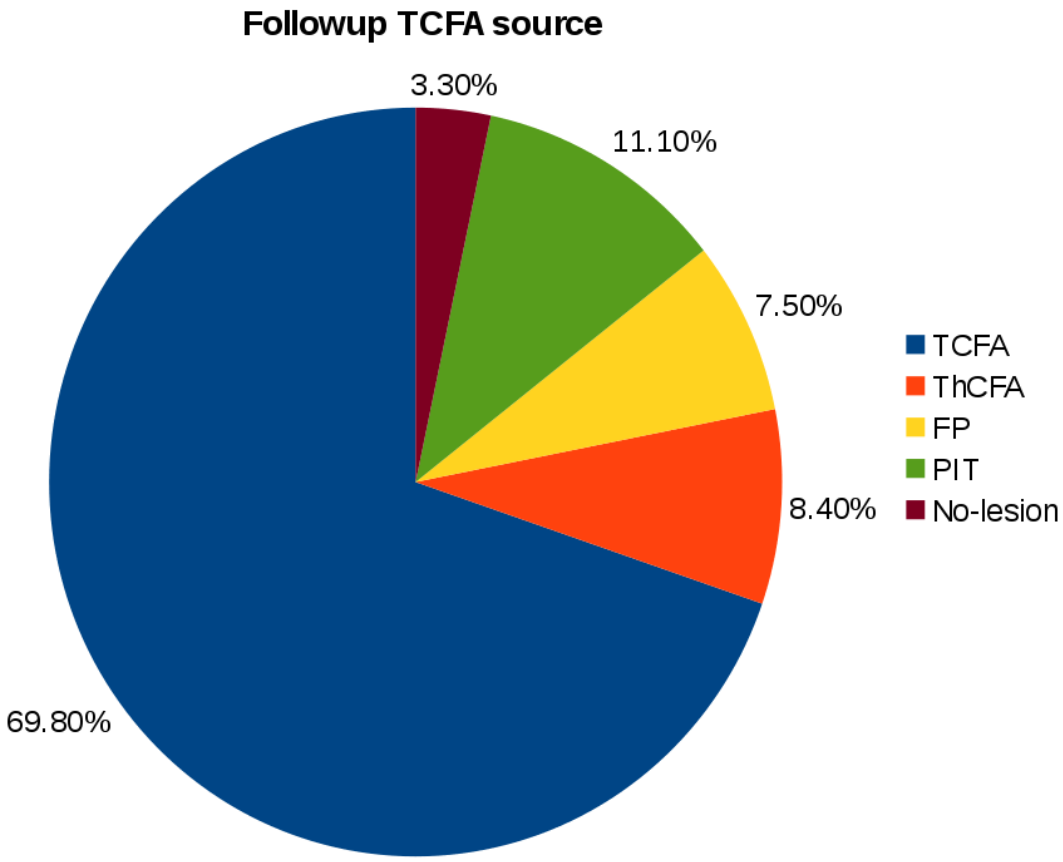

Figure 4.5: **Followup TCFA source.**

Table 4.3: **Phenotype percentage and lipid-lowering treatment correlation.**

	ΔTCFA%	ΔThCFA%	ΔFP%	ΔPIT%	ΔNo lesion%
Aggressive treatment	0.02+/-0.23	0.01+/-0.13	-0.01+/-0.11	0.02+/-0.20	-0.05+/-0.07
Standard treatment	0.20+/-0.24	0.04+/-0.11	-0.02+/-0.28	-0.18+/-0.18	0.06+/-0.07
p-value	**0.017**	0.46	0.87	**0.022**	0.568

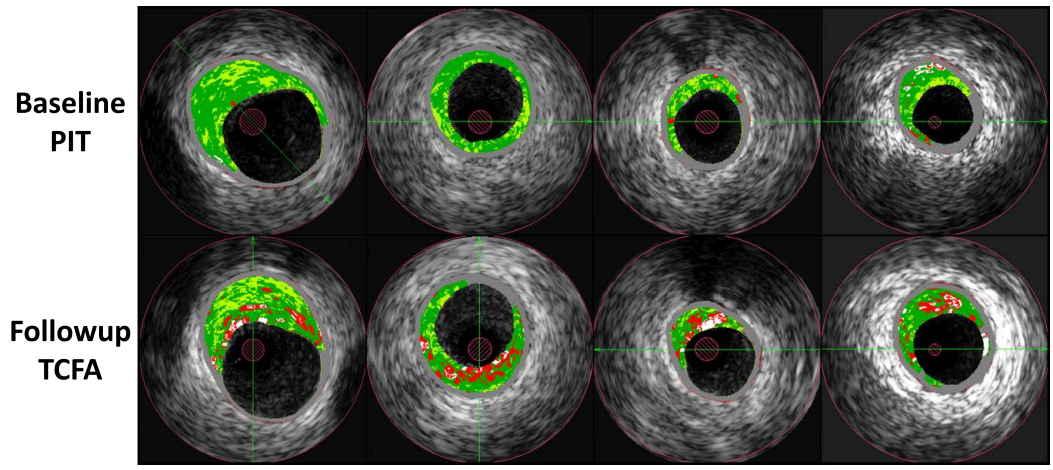

Figure 4.6: **Examples of baseline PIT transition to followup TCFA.**

4.4 Discussion and conclusion

Using intravascular imaging techniques to characterize plaque composition, and an established classification scheme for plaque phenotype determination, we sought to investigate the serial changes of different plaque phenotypes in patients with stable coronary artery disease by lipid-lowering treatment. We found that there was an increasing proportion of necrotic cores in PIT (also seen in FP phenotype) as compared to a decrease of necrotic cores with other plaque phenotypes. Among all phenotypes, PIT segments also experienced the most significant decrease of fibrofatty tissues. Furthermore, angles of necrotic core abutting lumen in PIT segments had the largest increment from baseline to followup. All those findings together proves PIT is the most dynamic phenotype of highest compositional changes from baseline to 1-year followup. Corban et al. [11] and Puri et al. [49] report similar findings that PIT most likely changed phenotype during their 6-month study. As to phenotype transition, 91.8% of PIT segments transformed into other phenotypes with 41.6% continuing to progress to a higher risk profile – TCFA. PIT also served as the main source of new TCFA emerging at followup (11.1% of all followup TCFA and 35.9% of newly developed TCFA). The decreasing PIT% and increasing TCFA%

for patients with standard treatment implied the transition between PIT and TCFA segments as well. Combined with compositional changes, those findings suggest that PIT is not a stable phenotype as previously reported and could be a more vulnerable or risky phenotype as the major precursor of fibroatheromas. This also confirms our findings in Chapter 3 that lipid-lowering treatment primarily works on advanced plaque phenotypes like fibroatheroma by shrinking necrotic core area but does not prevent plaque progression at early stage of atherosclerosis like PIT. In conclusion, with our automatic segmentation, registration and segmental analysis resulting in a more representative and comprehensive quantitative assessment of coronary morphology, pathological intimal thickening is observed as the most active plaque phenotype in terms of plaque composition changes and plaque vulnerability progression, in spite of presence of lipid-lowering therapy.

CHAPTER 5
MULTI-LAYER SEGMENTATION OF CORONARY INTRAVASCULAR OPTICAL COHERENCE TOMOGRAPHY IMAGES

In this chapter, an interactive refinement framework for intravascular optical coherence tomography (IVOCT) images segmentation was utilized and validated.

5.1 Introduction

Coronary allograft vasculopathy (CAV) is a frequent complication of heart transplantation (HTx), occurring in more than 50% of patients in the first post-transplant years. According to the Registry of the International Society for Heart and Lung Transplantation [20], CAV is the leading cause of death between 1 and 3 years after heart transplantation surgery. Unlike focal and eccentric conventional atherosclerosis, allograft vasculopathy is an accelerated coronary artery disease of concentric progressive intima thickening and diffuse luminal narrowing along the entire length of coronary vessels. Treatment of CAV is limited for the lack of early clinical symptoms. Therefore, this challenging complexity and silent fatality of CAV proves the importance of early determination of layer-specific coronary wall thickening using intravascular imaging modality.

Recall that intravascular optical coherence tomography (IVOCT) is an optical method of similar operation to IVUS, used to obtain high resolution ($\sim 10 mu$m) cross-sectional tomographic images of coronary arteries. IVOCT employs infrared light with central wavelength between 1,250 and 1,350 nm. Infrared light emitted by IVOCT catheter will be reflected or back-scattered from the coronary tissues and then the time delay of light will be measured using interferometry technique. A-line which is signal intensity as a function of delay time or depth within the tissue is determined. Coronary vessel wall microstructure in vivo can be visualized at an unprecedented level of detail by rotating the catheter optics to scan across the cross-sectional sample. It has been reported that precise measurement of intimal thickness could be evaluated

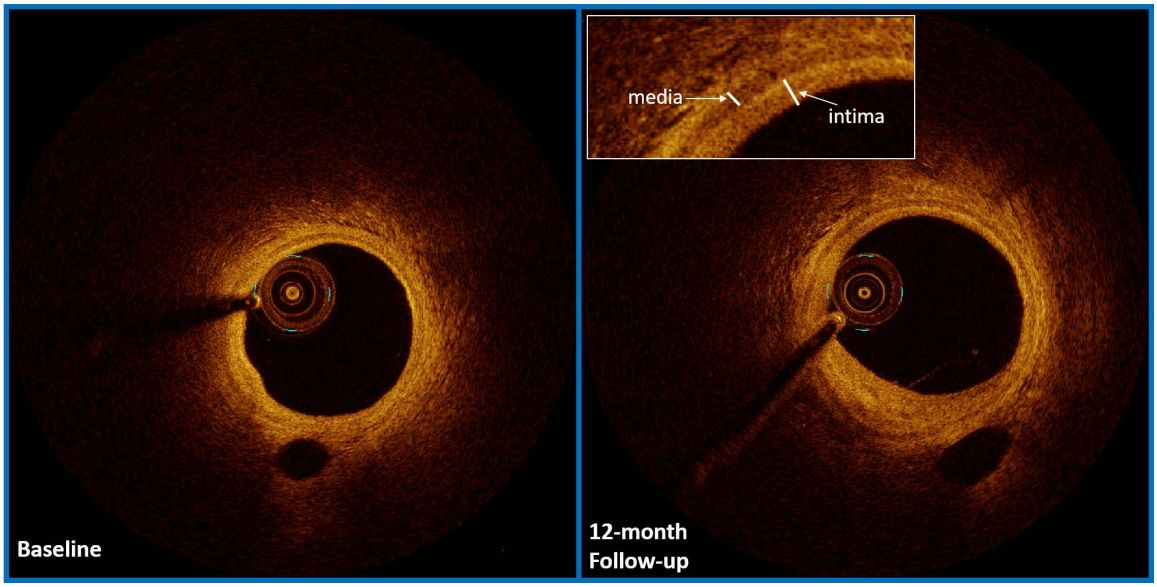

Figure 5.1: **Intravascular optical coherence tomography.** Baseline and matched 12-month followup cross-sectional images obtained by IVOCT are displayed on left and right panel respectively. Artery wall shows a 3-layered structure, comprising high backscattering intima and low backscattering media and heterogeneous adventitia.

by IVOCT and correlated well with histological examination [32]. Thus, IVOCT is supremely qualified for quantitative assessment of early CAV (see Figure 5.1).

5.2 Motivation

Compared to other intravascular imaging modality like ultrasound, IVOCT has multiple common artifacts duo to light characteristics making IVOCT segmentation a challenging task: (1) when blood is inadequately cleared in the field of view, residual blood attenuates the OCT light signal and may reduce brightness of the vessel wall, especially at large radial distances from the catheter; (2) due to the high resolution of IVOCT, previously indistinguishable guide-wire artifacts are recognized during coronary imaging, and these lower the visibility of artery wall layers and increase the discontinuities of target surface; (3) when the catheter is very near to or touching the artery wall, the tissue close to the catheter may have brighter gray scale value

blurring the delineation of lumen area. Moreover, the target layers (intima and media) are of very thin thickness especially before CAV. The intimal thickness measured by histology ranged from 0.10 to 0.89 mm while the intima and media combined thickness ranged from 0.21 to 1.20 mm in previous reported study [32]. The subtleness of coronary wall layer after heart transplantation makes it even more difficult to perform a thickness assessment.

Because of above-mentioned difficulties, current clinical CAV researches [6, 24, 28] heavily relied on the manual tracing on discrete frames or short segments, which still required substantial effort and time to be devoted. However, previous studies [60, 73, 75] related to IVOCT imaging segmentation mainly focused on the determination of well-defined lumen border and classification of coronary tissues for atherosclerosis. Motivated by the need, we aim to present an automated approach for the 3-D segmentation of IVOCT images based on layered optimal graph image segmentation of multiple objects and surfaces (LOGISMOS) framework [33, 74]. LOGISMOS allows for optimal and simultaneous segmentation of multi-layer 3-D structure for the whole IVOCT pullback in a robust and computationally efficient manner. Furthermore, a computer-aided just-enough-interaction refinement method is proposed as well to help achieve fully satisfactory 3-D segmentation of IVOCT images. We believe this is first work that intends to provide a fast, efficient and accurate solution for IVOCT multi-layer assessment in the context of CAV.

5.3 Method

5.3.1 Preprocessing

Prior to applying the multi-layer segmentation, several preliminary processing including removal of IVOCT catheter, guide-wire and stationary artifact were implemented. First of all, a constant circular mark of diameter 0.8mm was automatically applied over the OCT catheter. Thus, the layer-like structure of catheter would not affect following segmentation. Secondly, the guide-wire is needed to be masked out

as well for it not only drops in signal intensity causing shadows on the abluminal side but also distorts lumen segmentation due to its high brightness. A fixed mask would not work because the guide-wire position varies frame by frame due to the bouncing and rotational movement of catheter. As observed in [73], the accumulative intensity of all pixels in A-scan of guide-wire would have significantly low value compared to normal artery wall. Besides, guide-wire positions has a good 3-D connectivity and rarely change dramatically in adjacent frames. Therefore, the beginning and ending angles of guide-wire can be determined through accumulative pixel map of all A-scans as seen in Figure 5.2-A. Dynamic programming was used to identify the shadow path in the map by combining magnitude gradient and intensity value as cost function. Note that original method [73] only chose gradient cost, which in practice was prone to overestimate the guide-wire range and caused lots of false positive masking. Thus, intensity value was added to compensate. In return, the guide-wire was not concealed completely but its layered structure was not preserved anymore, which makes our following layer segmentation robust. Last but not least, stationary image components that may contain a gain offset or stationary artifacts such as the catheter "halo" and caliber marks were removed by subtracting the average pullback frame from each image. The average frame was computed on a pixel-wise basis over the entire pullback length, and the introduction of artifacts was avoided by limiting the results of the subtraction to a value of zero. The final image after all preprocessing was presented in Figure 5.2.

5.3.2 Lumen segmentation

Lumen border would be segmented at first, which was used subsequently for graph construction of multi-layer segmentation. To speed up the this pre-segmentation process, single-surface LOGISMOS framework was utilized considering the excellent visibility of lumen border in IVOCT image [33, 74]. A multi-column graph was required for LOGISMOS approach by unfolding the lumen surface into a terrain-like surface

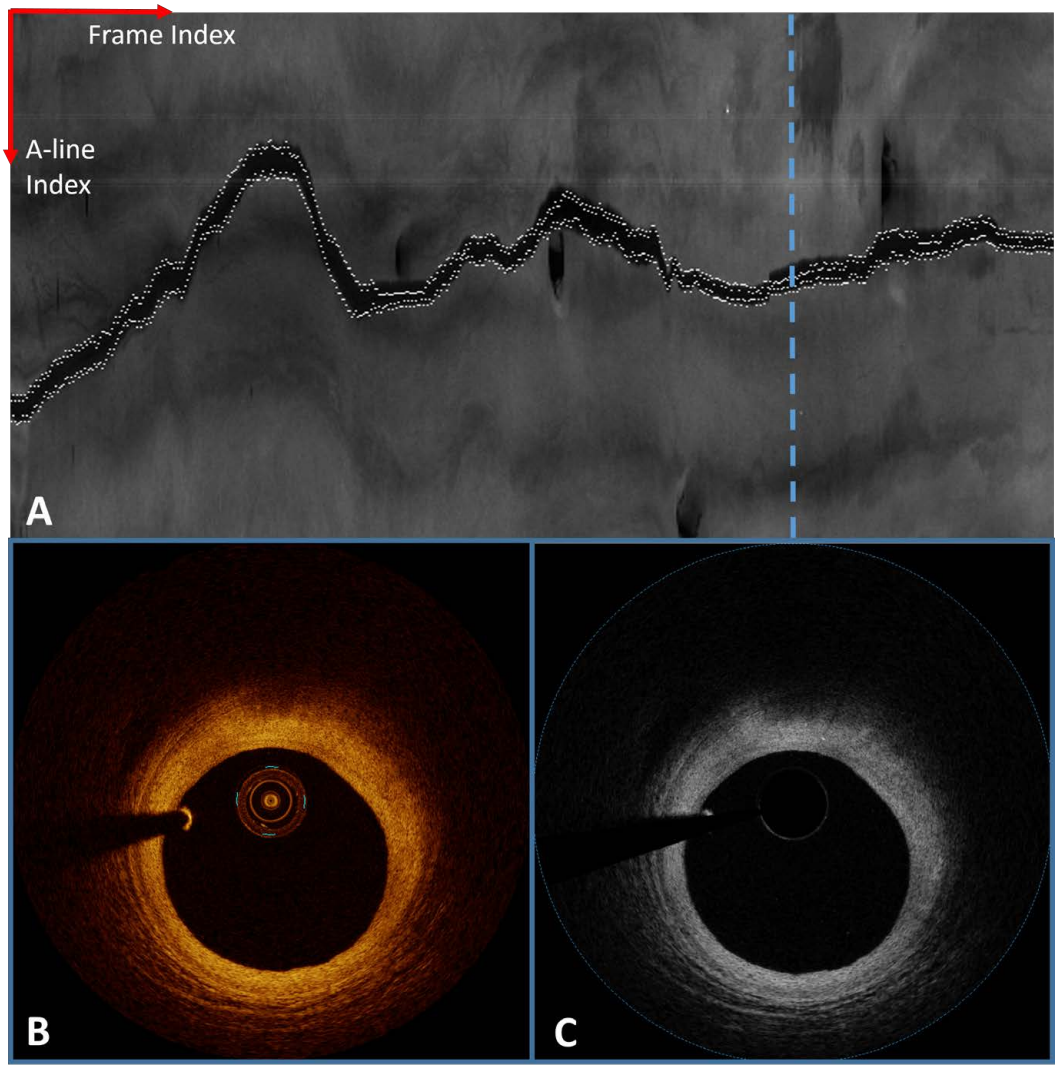

Figure 5.2: **Preprocessing of intravascular optical coherence tomography image.** **(A)** Accumulative pixel map of all A-scans along the pullback. Every single point in the map represents the intensity sum of all pixels at one A-scan for a frame. Blue dashed line represents the frame shown in (B) and two white dotted lines represent the segmented range of guide-wire. **(B)** An IVOCT image example. **(C)** IVOCT image after preprocessing.

along pullback direction.

IVOCT image center, i.e. catheter center was not preferred to unfold the original frame into polar coordinate. That is because when the catheter is extremely out of center, for example, touching the artery lumen (it's not uncommon in reality), the interval between adjacent columns in unfolded graph would correspond to highly uneven distance in physical space. Therefore, the lumen center was estimated roughly first by thresholding the frame using Otsu's method [45] and then obtaining center of mass(Figure 5.3).

A multi-column weighted graph G = (V,A) was then constructed based on these centers, where V is a graph node set and A is a graph arc set. $v \in V$ is a graph node on a column, associated with a image voxel I(x,y,z) if original pullback is viewed as a 3-D matrix. Each frame is represented as a subgraph $G_i \in G$ with $i = 1, 2, ..., N$ where N is total number of image frames. Within each subgraph G_i, n_p columns of length l_p are created starting from centers along the radial direction (Figure 5.3-C. The angular interval between columns is determined by $\theta_p = 360/n_p$. The distance between adjacent nodes within the same column is d_n. For IVOCT lumen segmentation, $n_p = 120, \theta_p = 30°, d_n = 1$ were used. In other words, 120 columns with node distance matched with image resolution were created for each frame. The column length l_p was set as A-scan length, which contained the potential positions of lumen border.

Then, intra-column edges are added to connect adjacent nodes on a column. Additionally, the inter-column edges connecting nodes between adjacent columns on the same frame are added to enforce the intra-frame smoothness constraints Δ_a. To implement 3-D connectivity, the inter-column edges connecting nodes between corresponding columns on adjacent frames are added to enforce the inter-frame smoothness constraint Δ_b. Figure 5.4-A and Figure 5.4-B provide a graphic illustration of how intra- and inter-column edges enforcing graph constraints are added. Δ_a and Δ_b

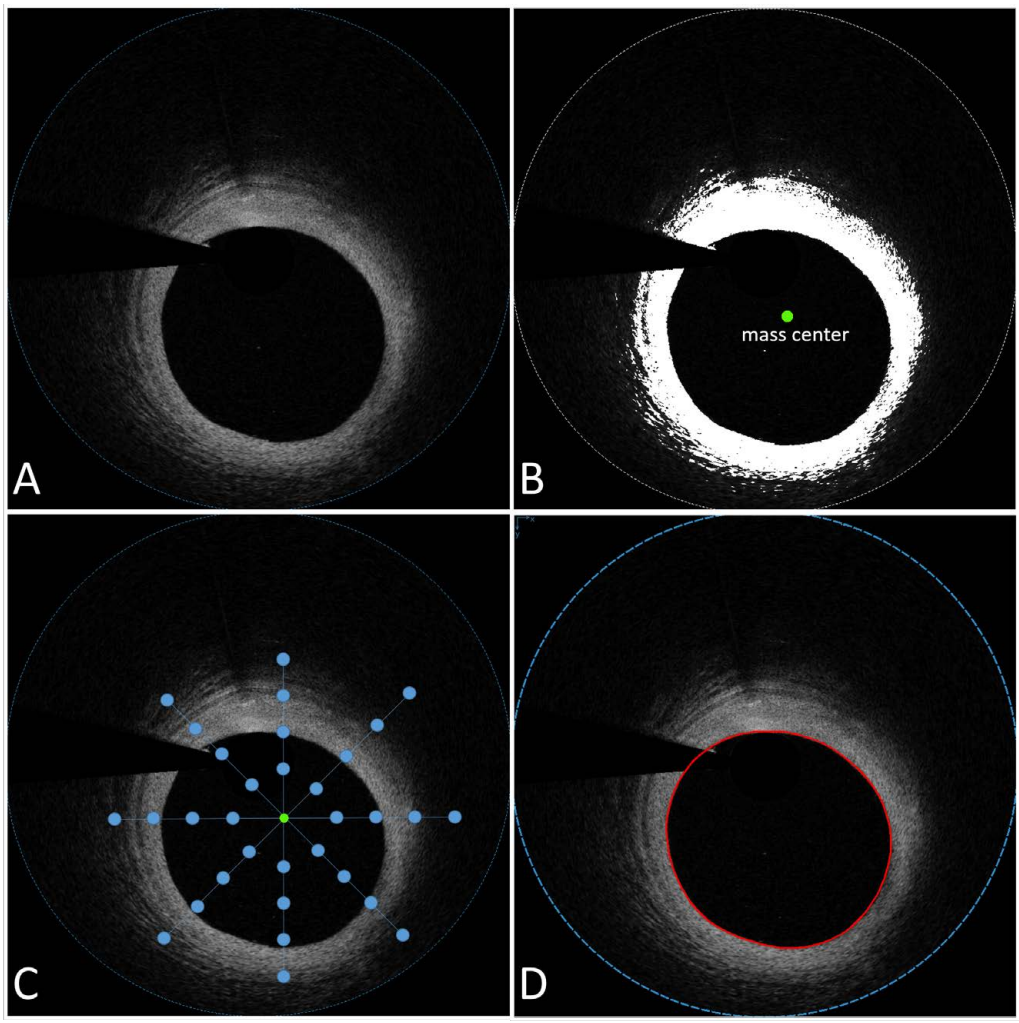

Figure 5.3: **Lumen segmentation.** **(A)** Original IVOCT image. **(B)** Thresholded image with center of mass (green). **(C)** Image with pseudo multi-columns model (blue). There are much more columns in real model and each column is much longer and denser with much more nodes. **(D)** Image with lumen segmentation (red).

represent the allowed search scope for feasible surface point when moving from one point to its neighboring point in within-frame direction and between-frame direction respectively. For IVOCT lumen segmentation, $\Delta_a = 6, \Delta_b = 5$ were determined by experimenting on 2 pullbacks, which were excluded from evaluation datasets.

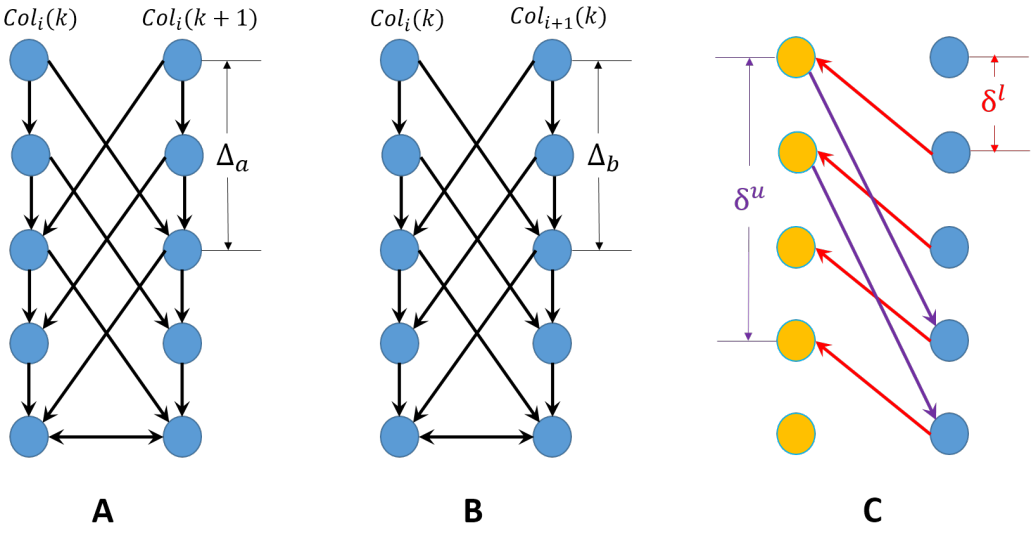

Figure 5.4: **Illustration of graph constraints for LOGISMOS graph construction. (A)** Edges connect nodes between adjacent columns ($Col_i(k)$, $Col_i(k+1)$) on the same frame (subgraph G_i) enforcing intra-frame smoothness constraints, where k is the column index. **(B)** Edges connect nodes between corresponding columns ($Col(k)$) on adjacent frames (subgraph G_i, G_{i+1}) enforcing inter-frame smoothness constraints. **(C)** Edges connect surface subgraphs enforcing the inter-surface constraints.

A key innovation of LOGISMOS is to transform the surface segmentation problem into an optimization problem aiming to find a minimum closed set in a node weighed graph. Let's denote C as graph node weight set, in which the cost of each node will reflect local image characteristics. The minimum closed set problem is to search for a closed set with the minimum cost. The directional derivative g_i along the A-scan starting from center at each pixel location for each subgraph G_i was computed. The

following cost $c(k,m)$ was assigned to each node $n(k,m)$, where k is column index and m is node index in a column:

$$c_i(k,m) = \begin{cases} -g_i(k,m) & \text{if } g_i(k,m) > 0 \\ 0 & \text{otherwise} \end{cases} \tag{5.1}$$

The dark-to-bright gradient representing lumen layer was preserved and inverted and other gradients were set to 0 as maximum cost. Finally, the actual minimum-cost closed set satisfying two smooth constraints was found by finding minimum-cost s-t cut in this node weighted graph. Max-flow algorithm with search tree reuse as described [3,33] was used to find minimum-cut s-t cut. A resulting lumen segmentation was shown in Figure 5.3-D.

5.3.3 Multi-layer segmentation

In this step, multi-layer segmentation was implemented by aligning pullback along real lumen centerlines, flattening all graph columns then based on pre-segmented lumen surface and solving new LOGISMOS weighted graph at last.

It is known that motion of the artery with respect to the catheter can result in disruption of the continuity of the pullback. In this case, 3-D connectivity of adjacent frames centered at catheter would be weakened, which in result would affect the performance of 3D-based LOGISMOS approach. To solve this problem, pre-segmented lumen borders were used to obtain the real lumen centerlines to replace the estimated mass centers. Subsequently, all cross-sectional frames were re-centered and aligned as shown in Figure 5.5. This lumen-centered alignment brought multiple benefits: 1) better 3D-connectivity of multi-layers along the pullback was achieved; 2) more intuitive visualization of pullback at longitudinal view was made for following just-enough-interaction editing; 3) consequential layer thickness was lumen centered as well so that clinically meaningful results could be obtained easily from segmentation

[27].

Instead of constructing multi-column graph from centerlines as previously lumen segmentation, we created the graph for multi-layer segmentation starting from pre-segmented lumen surface to provide a more consistent shape for segmentation. This process was originally termed as flattening [16] because terrain-like lumen surface would be a flat plane in resulting graph. In addition to providing consistent shape, flattening the volumetric graph made it possible to truncate the original image dramatically in the A-scan direction. If taking into account the limited tissue penetration depth (about 2.0 mm) of IVOCT light, even more truncation can be done. In practice, the flattening of graph was performed as starting from 0.2 mm inside the pre-segmented lumen surface (towards the center) to allow a more accurate re-segmentation of lumen. The truncation was ended at 2.0 mm outside the pre-segmented lumen surface (away from the center). In the end, the flattening shortened the graph search space for multi-layers from 3.5 mm (A-scan depth) to 2.2 mm, thereby reducing considerably computer memory and computation time required for LOGISMOS approach. Figure 5.5-C displayed cross-sectional frame and longitudinal pullback after flattening and truncation with pseudo columns showing the range of column. Note that the columns in the real graph had more nodes matched with image resolution.

The surfaces on the flattened and truncated volumetric images at unfolded polar coordinate were segmented based on the same LOGISMOS framework with some modifications. 4 sub-graphs $G_s, s = 1, 2, 3, 4$ representing 4 surfaces (lumen, upper intima, upper media and adventitia) are constructed with $\Delta - a$ and Δ_b smooth constraints following the same protocol in lumen pre-segmentation. Beside intra- and inter-column edges within frame and between frames, inter-surface edges connecting corresponding columns in adjacent constructed graphs G_s and G_{s+1} are added to enforce the lower-limit (δ^l) and upper-limit (δ^u) separation constraints (Figure 5.4-

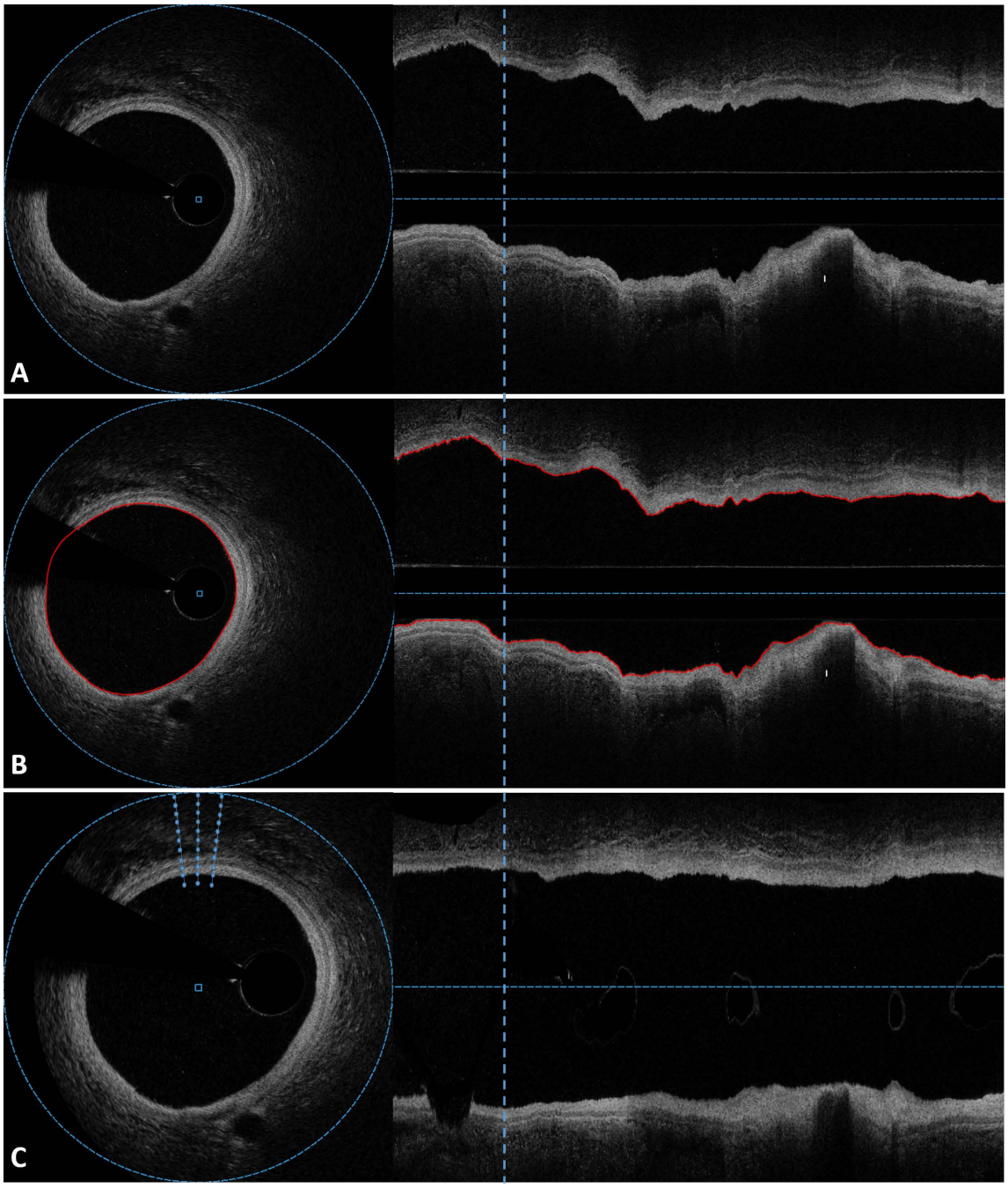

Figure 5.5: **Alignment and flatten based on pre-segmented lumen surface.** **(A)** Original image at both cross-sectional and longitudinal view. **(B)** Image with pre-segmented lumen border (red). **(C)** Aligned and flattened image based on lumen border. 3 pseudo columns are presented to demonstrate subsequent graph construction. In real model, there are more columns and the columns are much denser with more nodes.

C). As the name implies, separation constraints δ^l and δ^u indicate the minimum and maximum distances allowed between two adjacent surfaces.

For node weight, the directional derivative g_i along the A-scan at each pixel location was still used. Graph node weights for surface 1 and 3 (lumen and upper media) were set as shown in Equation 5.1 while weights for surface 2 and 4 (upper intima and adventitia) were set according to:

$$c_i k, m = \begin{cases} g_i(k,m) & \text{if } g_i(k,m) < 0 \\ 0 & \text{otherwise} \end{cases} \tag{5.2}$$

For multi-layer segmentation, other graph parameters were set as follows:

- $\Delta_a = 4, \Delta_b = 4$ for all surfaces.
- $\delta^l = 2, \delta^u = 10$ for between surface 2 and 3 as well as between surface 3 and 4.
- $\delta^2 = 2, \delta^u = 50$ for between surface 1 and 2 to allow large intima variations due to intima thickening [2, 20].

Those parameters were determined by experimenting on 3 pullbacks, which were excluded from evaluation datasets. A resulting multi-layer segmentation after finding minimum-cost s-t cut was shown in Figure 5.6.

5.3.4 Just-enough-interaction refinement

Our Just-enough-interaction (JEI) refinement method utilizes the same graph structure built in Section 5.3.3. The topology of the underlying graph structure was preserved during the interactive refinement. The information obtained from user interactive behavior only affected the graph node weight set [57]. JEI editing an automatic segmented image involved the following steps:

- identify the segmentation error in cross-sectional view or longitudinal view for a specific layer (Figure 5.7-A).

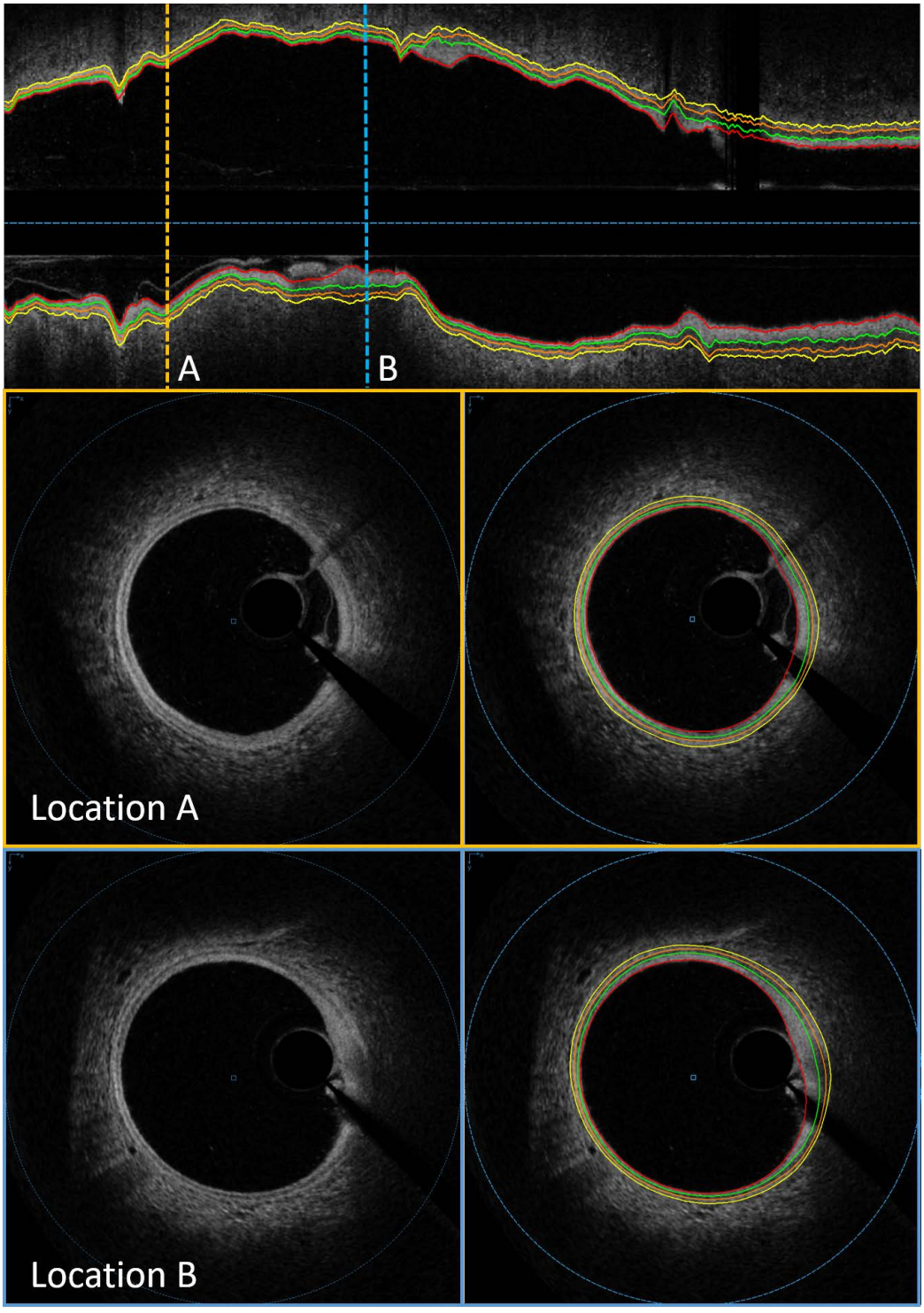

Figure 5.6: **Automated IVOCT multi-layer segmentation example.**

- draw a polygon line to roughly locate the potential boundary matching the true surface (Figure 5.7-B). To create a polygon line, click repeatedly with mouse in our graphic user interface to create line segments.

- utilize above polygon line to identify the nearest graph columns and nodes; update corresponding node costs locally for affected columns.

- find the new minimum closed set in the updated weighted node graph.

- refreshing new surfaces visually (Figure 5.7-C).

More specifically, given the line segments from user interaction, the polygon line was created by connecting all editing points and unfolded into polar coordinate to match the graph structure. only locations inside the graph coverage were considered. Then, the polygon line was converted to a set of intersection nodes with graph that defines the target surface should pass through. Note that only one interaction node can be generated in each affected column in theory based on LOGISMOS framework. Let's denote $c_k(i)$ as cost of affected column and p_k as index of interaction nodes, where k is column index and i is node index within column. Three strategies to update node costs for affected columns were listed on the order of expected refinement strength:

- **Low:** apply a step function with range r and magnitude w centered at p_k along the column:

$$c_k(i) = \begin{cases} w * c_k(i) & \text{if } p_k - r < i < p_k + r \\ 0 & \text{otherwise} \end{cases} \tag{5.3}$$

  when $w = 1$, the original cost profile of nodes within the step range ($r = 4$) was preserved while costs of out-of-range nodes were set to 0 (maximum cost value). The updated column cost would provide a possible range for desired surface to pass through with priority corresponding to original cost profile.

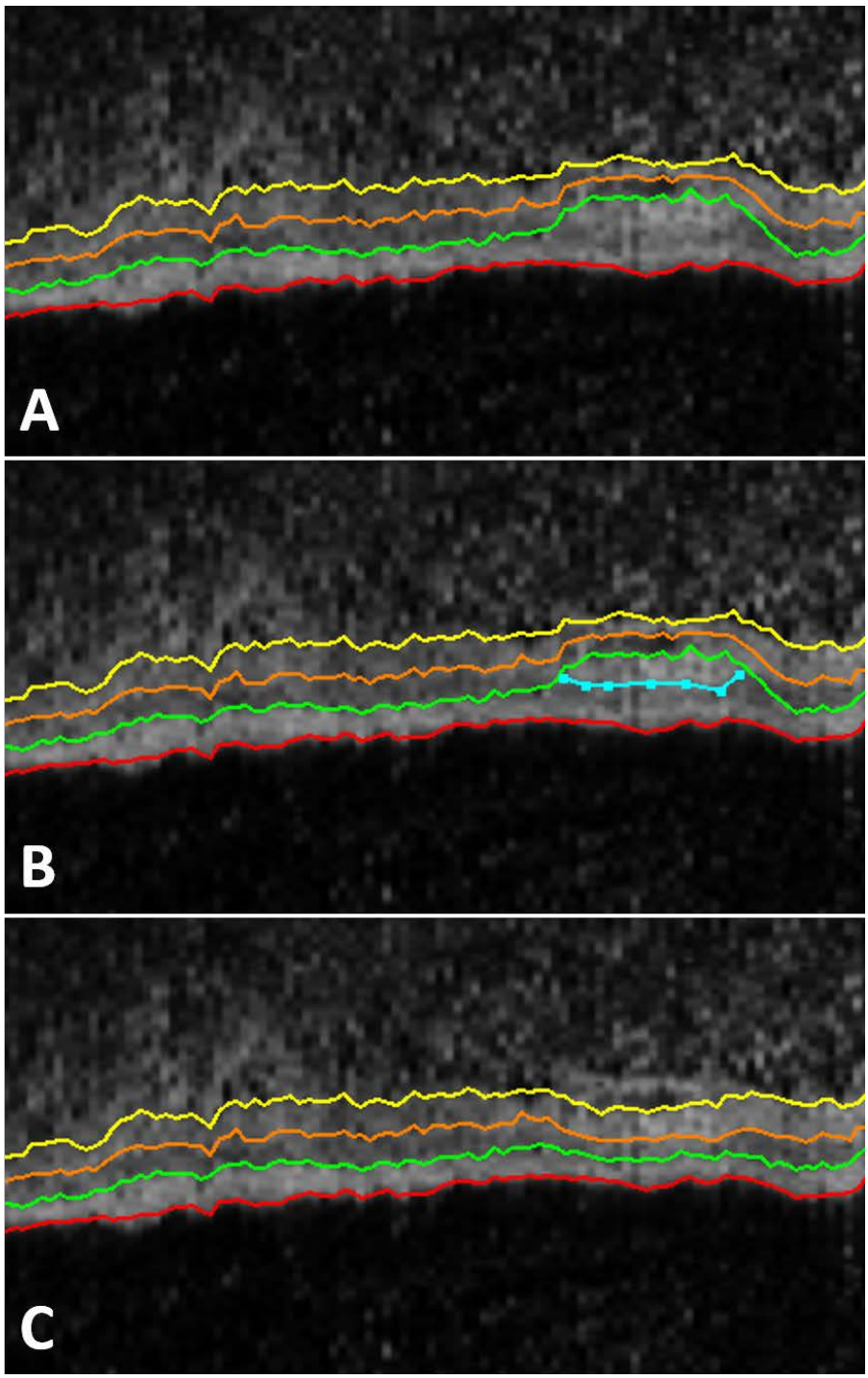

Figure 5.7: **IVOCT multi-layer segmentation with JEI refinement. (A)** Automated multi-layer segmentation with inaccuracy due to layer-like microstructure out of adventitia (surface 4). **(B)** The polygon line (blue) drawn roughly by user to identify the desired location of surface 3. **(C)** Resulting surfaces after refinement. Surface 1,2 and 3 were all corrected simultaneously even though only surface 3 was specified by user.

- **Medium:** apply a Gaussian function with respect to node distance from p_k along the column:

$$c_k(i) = \begin{cases} c_k(i) * e^{-\frac{d(i,p_k)^2}{2\sigma^2}} & \text{if } p_k - 1.96\sigma < i < p_k + 1.96\sigma \\ 0 & \text{otherwise} \end{cases} \tag{5.4}$$

  where $d(i, p_k)$ represented the distance from node i to node p_k while $\sigma = 2$ represented the locality of function. The updated column cost would provide a possible range for desired surface to pass through with priority corresponding to Gaussian-shaped cost profile centered at node p_k.

- **High:** apply a peak function centered at p_k along the column:

$$c_k(i) = \begin{cases} c_{peak} & \text{if } i = p_k \\ 0 & \text{otherwise} \end{cases} \tag{5.5}$$

  where c_{peak} represented possible minimum cost value. The updated column cost would provide the highest possibility for desired surface to pass through the specified node p_k.

Note that only affected columns in user specified surface were modified while other surfaces were kept unchanged. The simultaneous changes for all surfaces during JEI in Figure 5.7-C were achieved due to inter-surface connections and constraints in LOGISMOS graph.

By now, the current JEI refinement was limited in single cross-sectional frame or one longitudinal plane. Considering the similarity between adjacent frames along pullback and between adjacent columns in the same frame, the JEI refinement range can be expanded into a 3-D wedge sector (Figure 5.8):

- In cross-sectional JEI editing scenario, current frame with previous and after

adjacent two frames were formed as the 3-D wedge sector. The corresponding columns in additional frames would be updated following the same strategy.

- In longitudinal JEI editing scenario, current column with previous and after adjacent two columns were formed as the 3-D wedge sector. The span degree of sector was 12°. Cost of new columns would be updated accordingly.

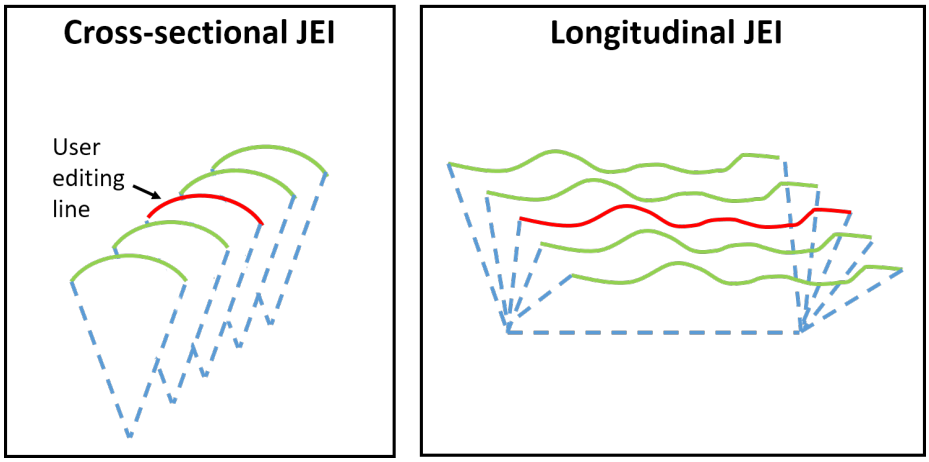

Figure 5.8: **IVOCT JEI refinement influence range.** The red line represents the polygon line derived from user interactive points while the green lines represent additional neighboring columns affected in 3-D space for cross-sectional or longitudinal view.

By adopting above framework, a graphical user interface designed for JEI refinement was built (see Figure 5.9).

5.4 Experimental method

5.4.1 Subject data

3-D intravascular OCT volumes (704 x 704 x 539) in this study were obtained from commercially available Fourier-Domain OCT system (St. Jude Medical) with C7 Dragonfly IVOCT catheter. Pullback of length ~54mm was generated with motorized

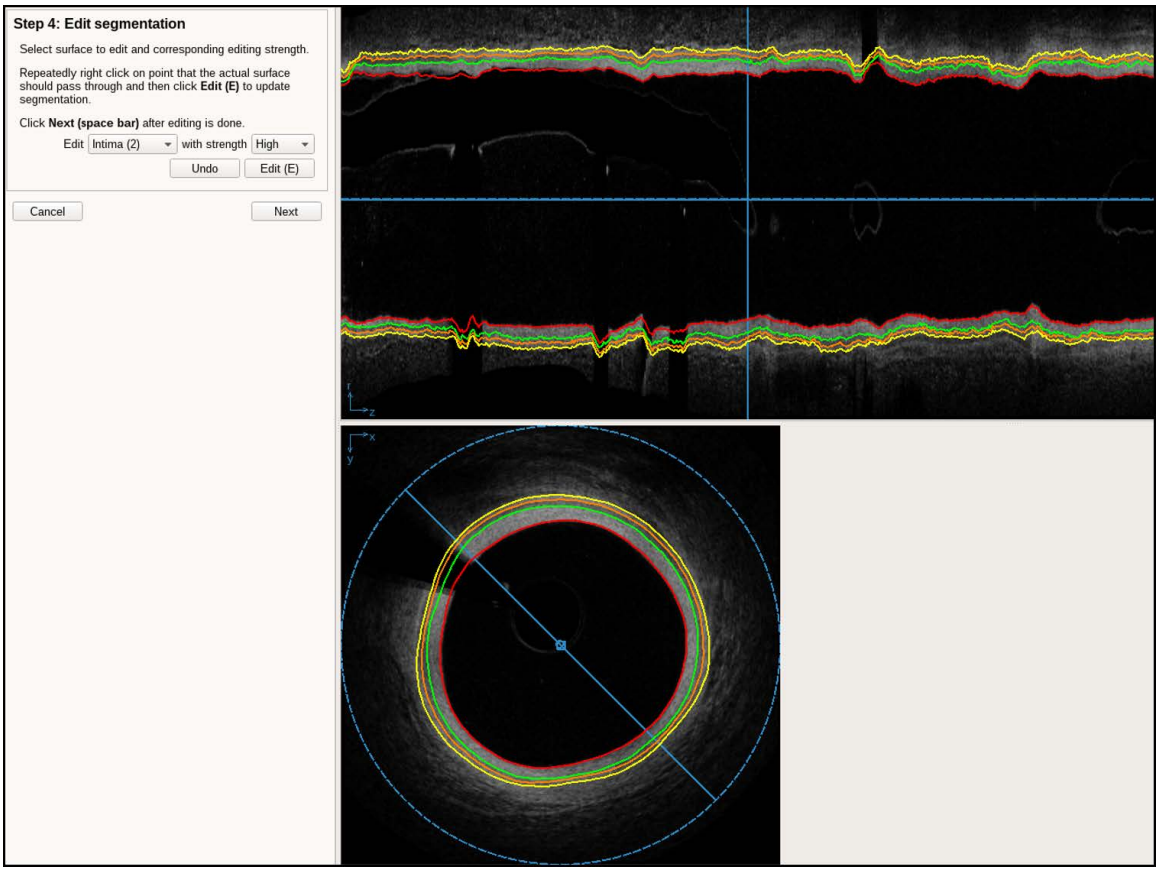

Figure 5.9: **Graphical user interface for IVOCT JEI refinement.**

pullback speed of 20mm/sec, 100 frames per second and 54,000 A-scans per second. Automated simultaneous multi-layer segmentation was performed in 38 IVOCT pullbacks from 20 HTx patients for a total of ∼20,480 frames. Computational time was recorded for each automated segmentation process. Afterwards, an expert inspected the automatic segmentation results and corrected segmentation inaccuracy by JEI refinement of high strength.

5.4.2 Independent standard

lumen surface and intimal/media thickness were evaluated separately on different datasets. The outermost surface adventitia was not evaluated because: (1) its delineation was too ambiguous at most cases; (2) it may disappear completely as intimal thickness progressed; (3)it was of less clinical importance in CAV research compared to intimal and media thickness. Thus, adventitia surface was used as support surface only to guide other surfaces segmentation.

As for naturally well-defined lumen border, 135 frames from 6 pullbacks (∼22 frames per pullback) were selected randomly. 2 experts blind to each other's criterion and also blind to automated segmentation results were asked to trace the lumen border manually.

As for relatively blurred intima/media layers, 394 frames from all 38 pullbacks (∼10 frames per pullback) were selected randomly. Another 2 experts determined manually the intima thickness (layer thickness between surface 1 and 2) and media thickness (layer thickness between surface 2 and 3) for each frame. Note that due to various artifacts like residual blood and guide-wire shadowing, not all layered structures are visible in each frame. Therefore, the overlapped angular range of each frame from two experts tracing were identified for later comparison. At least 40 minutes (4 minutes per frame) were devoted to trace intima and media layer manually for each pullback. Total tracing time for 394 frames from 38 pullbacks was around 25 hours.

5.4.3 Segmentation accuracy evaluation

The lumen segmentation accuracy was assessed by comparing automatic segmented border to manual traced surface. Both unsigned and signed positioning errors for each frame was averaged and compared. Dice coefficient of lumen area was also utilized to reflect the similarity.

To evaluate more dedicate intima/media thickness, more detailed comparison was performed by extracting continuous points from target surface at one-degree interval in polar coordinate, resulting 54,312 points from 392 frames. Therefore, point-based and frame-based intima/media thickness were compared with corresponding independent standard.

5.5 Results

Compared to independent standard (Manual1 and Manual2), the unsigned and signed positioning errors of automated lumen border along with lumen area Dice coefficient was displayed in Table 5.1. Inter-observer variability was listed at last for comparison.

Table 5.1: **IVOCT lumen segmentation evaluation**.

	Auto. vs. Manual1	Auto. vs. Manual2	Manual1 vs. Manual2
Unsigned error (μm)	29.69 ± 18.97	28.49 ± 17.78	31.54 ± 8.43
Signed error (μm)	13.70 ± 19.38	-2.22 ± 18.61	-15.92 ± 10.88
Dice coefficient	98.9% ± 0.7%	98.9% ± 0.6%	98.8% ± 0.4%

* All values were presented as mean ± standard deviation.

The required time for automated segmentation process of 38 pullbacks including preprocessing, lumen pre-segmentation, graph flattening and multi-layer segmentation were 95.70 ± 13.36 sec. For total of 20,480 frames, the required time per frame was 0.18 ± 0.02 sec. Table 5.2 and Table 5.3 displayed the point-based differences

intimal and media thickness among automated segmentation, JEI segmentation and manual tracing. Meanwhile, Table 5.4 and Table 5.5 displayed frame-based differences.

Table 5.2: Point-based IVOCT segmented intimal thickness accuracy evaluation.

	Intimal thickness		
	Unsigned error (μm)	Signed error (μm)	Correlation (R^2)
Auto. vs. Manual1	27.40+/-40.93	-2.06 +/- 49.21	0.97
JEI vs. Manual1	16.53+/-16.38	0.81+/-23.26	0.99
Auto. vs. Manual2	26.46+/-40.87	-0.47+/-48.69	0.97
JEI vs. Manual2	15.31+/-15.29	2.39+/-21.50	0.99
Manual2 vs. Manual1	13.42+/-12.05	3.91+/-17.61	0.99

* All values were presented as mean ± standard deviation.

Table 5.3: Point-based IVOCT segmented media thickness accuracy evaluation.

	Media thickness		
	Unsigned error (μm)	Signed error (μm)	Correlation (R^2)
Auto. vs. Manual1	23.28+/-19.18	-0.90+/-30.15	0.97
JEI vs. Manual1	20.52+/-15.91	2.92+/-25.80	0.99
Auto. vs. Manual2	20.82+/-18.37	-4.36+/-27.42	0.97
JEI vs. Manual2	17.84+/-14.61	-0.55+/-23.06	0.99
Manual2 vs. Manual1	16.61+/-14.37	3.48+/-21.69	0.99

* All values were presented as mean ± standard deviation.

5.6 Discussion and conclusion

The lumen segmentation accuracy was quantified both on a pixel-wise error and on a regional manner. Unsigned positioning errors and Dice coefficients (Table 5.1) of our automated lumen segmentation were comparable to both independent standards. With respect to inter-observer variability, signed errors demonstrated the stability of

Table 5.4: Frame-based IVOCT segmented intimal thickness accuracy evaluation.

	Intima thickness		
	Unsigned error (μm)	Signed error (μm)	Correlation (R^2)
Auto. vs. Manual1	24.61+/-39.99	-4.68+/-46.74	0.98
JEI vs. Manual1	11.21+/-10.16	0.10+/-15.14	0.99
Auto. vs. Manual2	23.24+/-38.94	-2.78+/-45.28	0.98
JEI vs. Manual2	9.88+/-9.61	1.99+/13.64	0.99
Manual2 vs. Manual1	7.79+/-6.73	3.58+/-9.66	0.99

* All values were presented as mean ± standard deviation.

Table 5.5: Frame-based IVOCT segmented media thickness accuracy evaluation.

	Media thickness		
	Unsigned error (μm)	Signed error (μm)	Correlation (R^2)
Auto. vs. Manual1	19.25+/-15.94	-2.20+/-24.92	0.97
JEI vs. Manual1	16.17+/-11.77	2.56+/-19.85	0.99
Auto. vs. Manual2	18.18+/-16.32	-5.34+/-23.86	0.97
JEI vs. Manual2	14.83+/-11.20	-0.58+/-18.58	0.99
Manual2 vs. Manual1	10.37+/-7.76	3.16+/-12.57	0.99

* All values were presented as mean ± standard deviation.

our lumen segmentation approach. These excellent lumen segmentation results have laid a good foundation for following multi-layer segmentation.

Table 5.2, Table 5.3 Table 5.4 and Table 5.5 displayed that both automated intimal and media segmentation correlated well with independent standards. Visually, our automated multi-layer segmentation for IVOCT was shown to be robust and free from disturbance of various artifacts (Figure 5.10). However, multiple factors including layer-like micro-structure outside adventitia and advanced plaque tissue would mislead segmentation algorithm as well. That's the place where JEI refinement should be involved. JEI provided a significantly better improvement for intimal thickness ($p < 0.01$) and slightly better improvement for media thickness, making the final segmentation results even more comparable to independent standards. Note that the media thickness accuracy was always lower than the intima thickness accu-

racy, which was expected due to the fact that the visibility of media surface would be diminished as the CAV disease progressed.

It's important to mention that at least 40 minutes were required to trace 10 frames for each pullback. It is unrealistic to expect an expert to trace the whole pullback of ∼539 frames to perform a thickness assessment. Even if the expert finishes the tracing after devoting more than 30 hours per pullback, it's not guaranteed that the tracing accuracy could be maintained with much more frames to trace. In contrast, only 95.70 ± 13.36 sec were required for our automated process to segment the whole pullback. This was achieved by many efforts including: 1) pre-segmenting lumen to allow subsequent alignment (which was done in less than 15 seconds), 2) flattening the graph to narrow down the search range, and 3) adopting relative simple cost function. Besides, inherent superiority of LOGISMOS framework for simultaneous multi-layer segmentation problem played an essential role as well. The fast automated segmentation process was also important in our interactive work-flow, shortening the user's waiting time for refinement step.

As for JEI refinement, 2 to 15 minutes per pullback were required depending on structural complexity of artery wall, which was still superior to fully manual tracing. The advantages of JEI refinement are summarized as follows:

- JEI provided near-instant response after editing line is drawn by reusing pre-built graph structure in automation step.
- Editing line is not required to be exactly matched with true border. Rough matching was allowed due to the dynamic nature of underlying graph, which offers great conveniences for users considering the subtleness of intima and media.
- Simultaneous multi-layer editing is feasible even if inaccuracy of only one surface was specified and fixed, which is another advantage of LOGISMOS framework.

- Editing is more efficient and resulting surfaces are more likely to be 3-D connected with less discontinuity, both crediting to inherently three-dimensional implementation of refinement on both cross-sectional and longitudinal views.

To the best of our knowledge, this is first study to report a simultaneous multi-layer segmentation method for IVOCT images to facilitate accurate layer-specific quantification of coronary wall thickness after heart transplantation. Evaluated on 38 in vivo pullbacks, our new highly automated method offers performance statistically indistinguishable from that of expert tracing. The proposed approach also provides a fast and efficient interactive environment with computer-aided just-enough-interaction refinement to achieve a even more accurate and comprehensive quantification of coronary layered structure. This could provide a useful aid for future study related to coronary allograft vasculopathy and could be easily expanded to other IVOCT-based coronary researches with some minor modifications.

5.7 Initial translational research studies performed using IVOCT segmentation

The IVOCT segmentation approach reported above was employed for two preliminary studies of CAV in a heart-transplant population as presented below.

5.7.1 Should we pharmacologically modulate ReninAldosteroneAngiotensin System (RAAS) to attenuate cardiac allograft vasculopathy? - A prospective study using highly automated coronary optical coherence tomography segmentation software in 3D

Introduction: Calcineurin inhibitor (CNI) therapy and graft denervation was proved to augment RAAS activity after heart transplant (HTx). This neurohormonal imbalance may have a detrimental effect on cardiac allograft vasculopathy (CAV).

Methods: This is a prospective and observational study consisted of 15 consecutive HTx patients. OCT imaging and aldosterone level measurements were performed

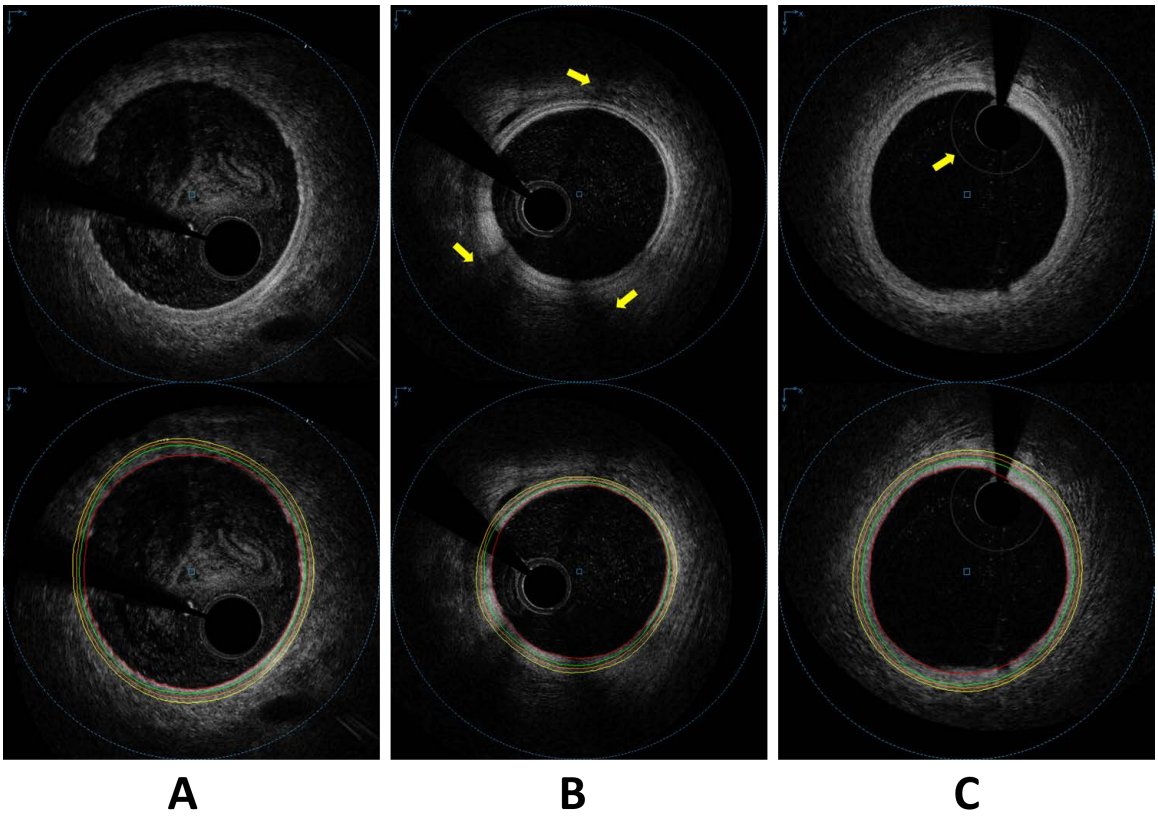

Figure 5.10: **Multi-layer segmentation for IVOCT images with artifact.** **(A)** Segmentation results for image with residual blood. **(B)** Segmentation results for image with shadowing (yellow arrow) caused by tissue adherent to the catheter. **(C)** Segmentation results for image with circular reflection (yellow arrow) likely caused by multiple facets of the catheter.

in 1st and 12th month after HTx. Our highly automated segmentation software simultaneously identifies luminal, intimal, inner-medial, and outer-medial surfaces in the entire 3D OCT pullback, quantifying location-specific intimal thickening between two imaging sessions. To overcome the inherent limitation of OCT imaging that is unable to depict full intimal layer in thick plaques due to insufficient penetration of the imaging beam, considering that CAV is a diffuse process, intimal thickening was measured within a 90 angular sector surrounding the location of minimal intimal thickness in each OCT frame. This measure of intimal thickness around the minimal thickness served as a surrogate intimal thickness (SIT) for progression assessment.

Results: A total number of 16115 corresponding frames from 15 paired 1-month and 12-month pullbacks [LAD (n=12), RCx (2), RCA (1)] were grouped into 276 3-mm segments for assessment of intimal thickness changes. We have identified a mean per-segment-change of SIT as 24.4 ± 5.2m. Strong correlation was found between high levels of aldosterone 1 month after HTx and SIT-determined progression of intimal thickness (R=0.62, p=0.014) as shown in Figure 5.11.

Conclusion: Using our 3D quantitative assessment of OCT intimal thickness changes, high levels of aldosterone 1 month after HTx strongly correlated with SIT increase, which represents the overall level of intimal thickness progression. Further evaluation of RAAS role in CAV development is warranted.

5.7.2 Increased heart rate after heart transplant is not associated with early progression of cardiac allograft vasculopathy (CAV) A prospective study using highly automatic coronary optical coherence tomography segmentation software in 3D

Introduction: Previous experimental and clinical data suggested that sustained elevation of heart rate may contribute to the pathogenesis of vascular disease. A hypothesis was formed that sinus tachycardia in heart transplant (HTx) patients resulting from cardiac denervation may be one of the contributing factors for development

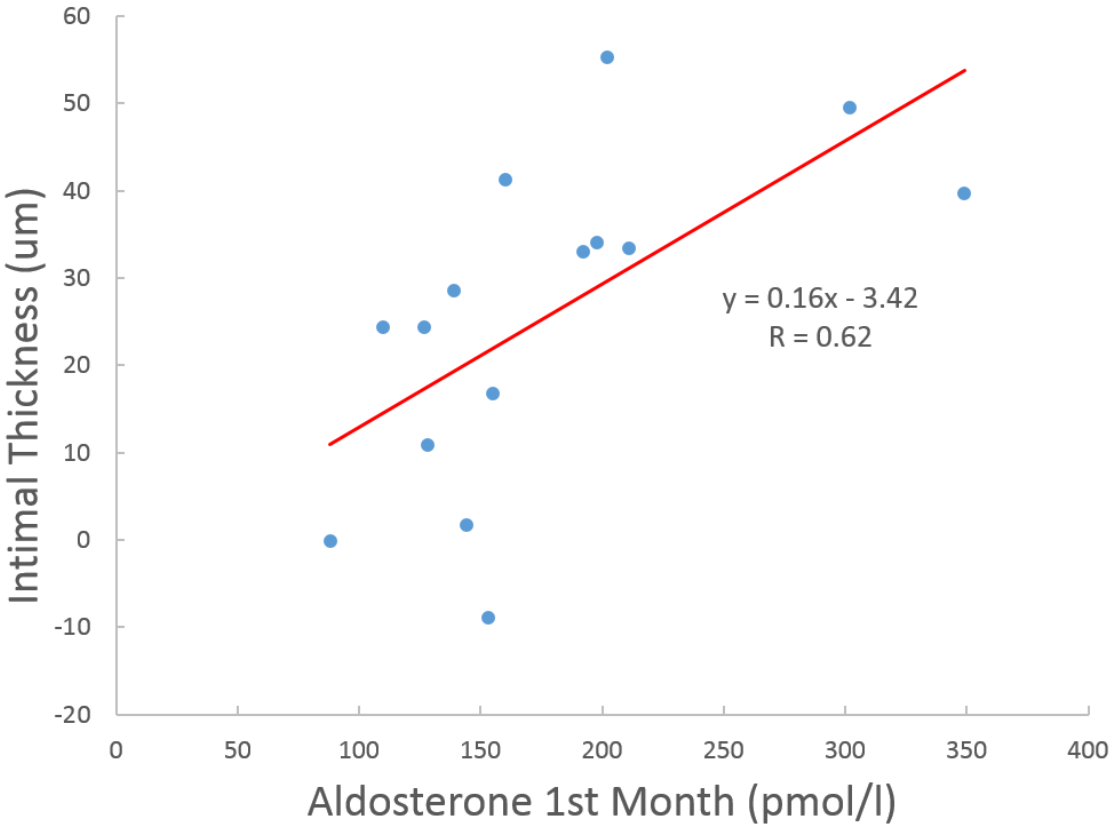

Figure 5.11: **Correlation between aldosterone and intimal thickening.**

of CAV. However, contradictory data exist in the HTx population.

Methods: In a prospective, observational, multi-centre study consisting of 33 consecutive patients who underwent HTx between 2014-2015 in IKEM Prague and St. Anna hospital in Brno, Czech Republic. OCT imaging and 24 hour ECG Holter monitoring was performed in 1st and 12th months after HTx. Highly automated in-house developed segmentation software allowed quantitative analysis of intimal thickening in the entire 3D pullback. To overcome the inherent limitation of OCT imaging that is unable to depict full intimal layer in thick plaques due to insufficient penetration of the imaging beam and utilizing the assumption that CAV is a diffuse process, intimal thickening was measured within a 90 angular sector surrounding the location of minimal intimal thickness in each OCT frame. This measure of intimal thickness around the minimal thickness served as a surrogate intimal thickness (SIT) for progression assessment.

Results: A total number of 28448 corresponding frames from paired 1-month and 12-month pullbacks [LAD (n=25), RCx (5), RCA (3)] were grouped into 501 3-mm segments for progression of SIT. Mean change of the per-segment SIT was 23.7±21.1m. Mean heart rate was 80.3±8.6 min-1 in the 1st month after HTx, 84.2±10.6 min^{-1} in the 12th month with the average heart rate in both periods of 82.2±8.0 min^{-1}. No correlation between heart rate and progression of intimal thickness within 12 months after HTx was found in either of the groups (R=0.14, p=0.45 in month 1, R=-0.18, p=0.33 in month 12; R= -0.04, p=0.81 for averaged heart rate).

Conclusion: Our results based on accurate fully 3D analysis of intimal thickness changes do not support the hypothesis that high heart rate is contributing to early development of CAV. This finding may impact the use of beta blockers in HTx patients and preferably administer them to those with hypertension and/or arrhythmia.

5.7.3 Summary

Based on our automated and interactive IVOCT segmentation environment, the correlation between high levels of aldosterone 1 month after HTx strongly and SIT progression, and the correlation between 1-month and 12-month heart rate and SIT progression were evaluated. The results provided some insights to diagnosis and treatment of CAV disease. With more patients and clinical information involved, more comprehensive researches of clinical significance can be expected in the near future.

CHAPTER 6
CONCLUSION AND FUTURE DIRECTIONS

6.1 Conclusions

When talking about coronary atherosclerosis, indirect IVUS-VH-derived TCFA is one of most widely used concepts to identify the potential risk factors of plaque rupture. But no compelling evidence has ever been provided for the definition and the determination has been shown to have a markedly higher inter-observer variability. To address this issue, 105 novel and comprehensive variations of IVUS-VH-derived TCFA was designed and evaluated in Chapter 2 (Aim 1). As a result, the overestimated prevalence of IVUS-VH-derived TCFA was proved. That's not the first report questioning the credibility of IVUS-VH-derived TCFA. However, to our knowledge, this is the first study to use computational analysis to explore the possibility of a better TCFA definition. Additionally, no previous in vivo study that has investigated the association between ruptured cavity and plaque components in a novel layered analysis.

In Chapter 3 (Aim 2.1), we reached a comprehensive understanding of real dynamic nature of remodeling under lipid-lowering treatment. With the help of automated segmentation and registration, we resolved some major limitations of previous studies:

- Patient-based and continuous segmental-based assessment was performed instead of discrete frame-based or lesion-based.
- Serial and dynamic development of remodeling was quantified instead of static changes with indirect quantitative indices.
- Both changing direction and changing magnitude of remodeling were considered.

As far as we know, there is no other study with the same scale of comprehensiveness.

In Chapter 4 (Aim 2.2), pathological intimal thickening, which previously was

considered innocent and was buried in oblivion most of the time, was observed as the most active plaque phenotype in terms of plaque composition changes and plaque vulnerability progression. Beside inherent comprehensiveness of this study, the observation itself has certain innovation and can serve as an important reference to predict future plaque rupture.

The LOGISMOS framework is a powerful approach and has been previously applied to a number of medical image segmentation problems. However, the difficulties of IVOCT segmentation of subtle multiple layers made it quite challenging to design a fully automated LOGISMOS framework working on all occasions. Therefore, as a necessary and beneficial supplement to original LOGISMOS framework, computer-aided just-enough-interaction refinement was implemented to help achieve fully satisfactory 3-D segmentation of IVOCT images in Chapter 5 (Aim 3). We believe this is first work that provides a fast, efficient and accurate solution for IVOCT multi-layer assessment in the context of CAV disease.

The methodology and framework designed in this thesis have a few potential applications and future directions:

6.2 Future image analysis direction

Fluid dynamics analysis of blood flow. With segmentation of IVUS, fusion of IVUS and angiography and modeling of side branches, the 3-D luminal reconstruction can be achieved and then used to analyze the blood flow profiling due to changes of coronary artery geometry, thereby identifying risk factors for progression of coronary disease.

Coronary TCFA segmentation based on IVOCT and comparison with IVUS. Current JEI work-flow in Chapter 5 can be easily expanded with some minor modifications to segmentation of IVOCT coronary TCFA, which can be visualized directly due to the high resolution of IVOCT. Currently, TCFA ground truth is only available through ex-vivo examination of cadaver heart. With the in vivo TCFA

identified in IVOCT, the study in Chapter 2 can also be continued to generate the best IVUS-VH-derived TCFA criterion matching IVOCT-derived TCFA.

Serial IVOCT registration and different modalities registration. With baseline and followup IVOCT datasets for CAV disease, the quantification of intimal thickness progression requires serial registration between baseline and followup IVOCT pullback. For same patient, if both IVOCT and IVUS images are required one after another, the registration between IVOCT and IVUS pullback could be possible as well. The potential difficulty is that images of two modalities may be at different heart phases, leading to different luminal shape. Ungated IVOCT pullback vs. gated IVUS pullback could be another obstacle.

Automated identification of IVOCT visible angles. Recall that not all of IVOCT layers at 360 degrees are visible due to multiple artifacts. In this cases, accurate assessment of layered thickness should be based on visible range only. Thus, the automated identification of circular visibility for each frame is required. Classification based on the context features could be utilized. Emerging deep learning technique is also a possible solution.

6.3 Future clinical application direction

Serial studies related to specific disease and clinical events. Baseline and followup datasets of IVUS-VH images can also be analyzed and correlated to specific disease like diabetes. The results could provide useful guidance and predictive power to diagnose future disease. Moreover, if more followup datasets with major adverse cardiac events can be collected, the association between plaque serial changes of morphology and clinical events could also be assessed.

CAV disease studies utilizing quantitative assessment of intimal and media thickness. By utilizing quantitative assessment of intimal and media thickness obtained from our IVOCT JEI work-flow, a number of clinical analysis for CAV disease can be done. For example, the donor hearts before transplantation can be

evaluated by looking to intimal and media thickness along with presence of plaque; predictors of CAV progression in baseline and follow-up paired datasets could be determined by correlating biomarkers and demographic information to intimal progression; time series forecasting can be modeled to predict future intimal thickness value based on previously observed value.

REFERENCES

[1] J. A. Ambrose and R. S. Barua, "The pathophysiology of cigarette smoking and cardiovascular disease: an update," *Journal of the American college of cardiology*, vol. 43, no. 10, pp. 1731–1737, 2004.

[2] R. K. Avery, "Cardiac-allograft vasculopathy," *New England Journal of Medicine*, vol. 349, no. 9, pp. 829–830, 2003.

[3] Y. Boykov and V. Kolmogorov, "An experimental comparison of min-cut/max-flow algorithms for energy minimization in vision," *IEEE transactions on pattern analysis and machine intelligence*, vol. 26, no. 9, pp. 1124–1137, 2004.

[4] A. P. Burke, A. Farb, G. T. Malcom, Y.-h. Liang, J. Smialek, and R. Virmani, "Coronary risk factors and plaque morphology in men with coronary disease who died suddenly," *New England Journal of Medicine*, vol. 336, no. 18, pp. 1276–1282, 1997.

[5] P. A. Calvert, D. R. Obaid, M. O'Sullivan, L. M. Shapiro, D. McNab, C. G. Densem, P. M. Schofield, D. Braganza, S. C. Clarke, K. K. Ray, *et al.*, "Association between ivus findings and adverse outcomes in patients with coronary artery disease: the viva (vh-ivus in vulnerable atherosclerosis) study," *JACC: Cardiovascular Imaging*, vol. 4, no. 8, pp. 894–901, 2011.

[6] A. Cassar, Y. Matsuo, J. Herrmann, J. Li, R. J. Lennon, R. Gulati, L. O. Lerman, S. S. Kushwaha, and A. Lerman, "Coronary atherosclerosis with vulnerable plaque and complicated lesions in transplant recipients: new insight into cardiac allograft vasculopathy by optical coherence tomography," *European heart journal*, p. eht236, 2013.

[7] Z. Chen, A. Wahle, R. Downe, S. Sun, K. Porcaro, A. Agrawal, T. Hirai, V. Rangarajan, J. Kaminski, S. Hawn, T. Kovernik, M. Sonka, and J. Lopze, "Quantitative comparison of plaque in coronary culprit and non-culprit vessel segments using intravascular ultrasound," *Joint MICCAI-Workshops on Computing and Visualization for Intravascular Imaging and Computer Assisted Stenting*, 2014.

[8] Z. Chen, A. Wahle, L. Zhang, T. Kovarnik, J. J. Lopez, and M. Sonka, "Comprehensive serial study of dynamic remodeling of atherosclerotic coronary arteries using ivus," in *SPIE Medical Imaging*. International Society for Optics and Photonics, 2016, pp. 97 880Y–97 880Y.

[9] J. M. Cheng, H. M. Garcia-Garcia, S. P. de Boer, I. Kardys, J. H. Heo, K. M. Akkerhuis, R. M. Oemrawsingh, R. T. van Domburg, J. Ligthart, K. T. Witberg, *et al.*, "In vivo detection of high-risk coronary plaques by radiofrequency

intravascular ultrasound and cardiovascular outcome: results of the atheroremoivus study," *European heart journal*, vol. 35, no. 10, pp. 639–647, 2014.

[10] P. K. Cheruvu, A. V. Finn, C. Gardner, J. Caplan, J. Goldstein, G. W. Stone, R. Virmani, and J. E. Muller, "Frequency and distribution of thin-cap fibroatheroma and ruptured plaques in human coronary arteries: a pathologic study," *Journal of the American College of Cardiology*, vol. 50, no. 10, pp. 940–949, 2007.

[11] M. T. Corban, P. Eshtehardi, J. Suo, M. C. McDaniel, L. H. Timmins, E. Rassoul-Arzrumly, C. Maynard, G. Mekonnen, S. King, A. A. Quyyumi, *et al.*, "Combination of plaque burden, wall shear stress, and plaque phenotype has incremental value for prediction of coronary atherosclerotic plaque progression and vulnerability," *Atherosclerosis*, vol. 232, no. 2, pp. 271–276, 2014.

[12] R. Downe, A. Wahle, T. Kovarnik, H. Skalicka, J. Lopez, J. Horak, and M. Sonka, "Segmentation of intravascular ultrasound images using graph search and a novel cost function," in *Proceedings of 2nd MICCAI Workshop on Computer Vision for Intravascular and Intracardiac Imaging, New York, NY*, 2008, pp. 71–79.

[13] F. H. Epstein, V. Fuster, L. Badimon, J. J. Badimon, and J. H. Chesebro, "The pathogenesis of coronary artery disease and the acute coronary syndromes," *New England Journal of Medicine*, vol. 326, no. 4, pp. 242–250, 1992.

[14] N. Freemantle, J. Cleland, P. Young, J. Mason, and J. Harrison, "β blockade after myocardial infarction: systematic review and meta regression analysis," *Bmj*, vol. 318, no. 7200, pp. 1730–1737, 1999.

[15] H. M. Garca-Garca, G. S. Mintz, A. Lerman, D. G. Vince, P. Margolis, G.-A. Van Es, M.-A. Morel, A. Nair, R. Virmani, A. Burke, G. Stone, and P. W. Serruys, "Tissue characterization using radiofrequency data analysis: recommendations for acquisition, analysis, interpretation and reporting," *EuroIntervention*, 2009.

[16] M. K. Garvin, M. D. Abràmoff, X. Wu, S. R. Russell, T. L. Burns, and M. Sonka, "Automated 3-d intraretinal layer segmentation of macular spectral-domain optical coherence tomography images," *IEEE transactions on medical imaging*, vol. 28, no. 9, pp. 1436–1447, 2009.

[17] S. Glagov, E. Weisenberg, C. K. Zarins, R. Stankunavicius, and G. J. Kolettis, "Compensatory enlargement of human atherosclerotic coronary arteries," *New England Journal of Medicine*, vol. 316, no. 22, pp. 1371–1375, 1987.

[18] S. S. S. S. Group *et al.*, "Randomised trial of cholesterol lowering in 4444 patients with coronary heart disease: the scandinavian simvastatin survival study (4s)," *The Lancet*, vol. 344, no. 8934, pp. 1383–1389, 1994.

[19] J. B. Hermiller, A. N. Tenaglia, K. B. Kisslo, H. R. Phillips, T. M. Bashore, R. S. Stack, and C. J. Davidson, "In vivo validation of compensatory enlargement of atherosclerotic coronary arteries," *The American journal of cardiology*, vol. 71, no. 8, pp. 665–668, 1993.

[20] M. I. Hertz, D. O. Taylor, E. P. Trulock, M. M. Boucek, P. J. Mohacsi, L. B. Edwards, and B. M. Keck, "The registry of the international society for heart and lung transplantation: nineteenth official report2002," *The Journal of heart and lung transplantation*, vol. 21, no. 9, pp. 950–970, 2002.

[21] T. Hirai, Z. Chen, L. Zhang, S. Baaj, T. Kovarnik, K. Porcaro, J. Kaminski, S. Hawn, A. Agrawal, N. Makki, *et al.*, "Evaluation of variable thin-cap fibroatheroma definitions and association of virtual histology-intravascular ultrasound findings with cavity rupture size," *The American Journal of Cardiology*, 2016.

[22] M.-K. Hong, D.-W. Park, C.-W. Lee, S.-W. Lee, Y.-H. Kim, D.-H. Kang, J.-K. Song, J.-J. Kim, S.-W. Park, and S.-J. Park, "Effects of statin treatments on coronary plaques assessed by volumetric virtual histology intravascular ultrasound analysis," *JACC: Cardiovascular Interventions*, vol. 2, no. 7, pp. 679–688, 2009.

[23] J. Hosenpud, G. Shipley, and C. Wagner, "Cardiac allograft vasculopathy: current concepts, recent developments, and future directions." *The Journal of heart and lung transplantation: the official publication of the International Society for Heart Transplantation*, vol. 11, no. 1 Pt 1, pp. 9–23, 1991.

[24] J. Hou, H. Lv, H. Jia, S. Zhang, L. Xing, H. Liu, J. Kong, S. Zhang, B. Yu, and I.-K. Jang, "Oct assessment of allograft vasculopathy in heart transplant recipients," *JACC: Cardiovascular Imaging*, vol. 5, no. 6, pp. 662–663, 2012.

[25] D. Huang, E. A. Swanson, C. P. Lin, J. S. Schuman, W. G. Stinson, W. Chang, M. R. Hee, T. Flotte, K. Gregory, C. A. Puliafito, *et al.*, "Optical coherence tomography," *Science (New York, NY)*, vol. 254, no. 5035, p. 1178, 1991.

[26] I.-K. Jang, G. J. Tearney, B. MacNeill, M. Takano, F. Moselewski, N. Iftima, M. Shishkov, S. Houser, H. T. Aretz, E. F. Halpern, *et al.*, "In vivo characterization of coronary atherosclerotic plaque by use of optical coherence tomography," *Circulation*, vol. 111, no. 12, pp. 1551–1555, 2005.

[27] D. Jin, K. S. Iyer, C. Chen, E. A. Hoffman, and P. K. Saha, "A robust and efficient curve skeletonization algorithm for tree-like objects using minimum cost paths," *Pattern recognition letters*, vol. 76, pp. 32–40, 2016.

[28] S. J. Khandhar, H. Yamamoto, J. J. Teuteberg, M. A. Shullo, H. G. Bezerra, M. A. Costa, F. Selzer, J. S. Lee, O. C. Marroquin, D. M. McNamara, *et al.*, "Optical coherence tomography for characterization of cardiac allograft vasculopathy after heart transplantation (octcav study)," *The Journal of Heart and Lung Transplantation*, vol. 32, no. 6, pp. 596–602, 2013.

[29] T. Kovarnik, Z. Chen, A. Wahle, L. Zhang, H. Skalicka, A. Kral, J. J. Lopez, J. Horak, M. Sonka, and A. Linhart, "Pathologic intimal thickening plaque phenotype: Not as innocent as previously thought. a serial 3d intravascular ultrasound virtual histology study," *Revista Española de Cardiología (English Edition)*, 2016.

[30] T. Kovarnik, G. S. Mintz, H. Skalicka, A. Kral, J. Horak, R. Skulec, J. Uhrova, P. Martasek, R. W. Downe, A. Wahle, *et al.*, "Virtual histology evaluation of atherosclerosis regression during atorvastatin and ezetimibe administration-heaven study," *Circulation Journal*, vol. 76, no. 1, pp. 176–183, 2012.

[31] T. Kubo, A. Maehara, G. S. Mintz, H. Doi, K. Tsujita, S.-Y. Choi, O. Katoh, K. Nasu, A. Koenig, M. Pieper, *et al.*, "The dynamic nature of coronary artery lesion morphology assessed by serial virtual histology intravascular ultrasound tissue characterization," *Journal of the American College of Cardiology*, vol. 55, no. 15, pp. 1590–1597, 2010.

[32] T. Kume, T. Akasaka, T. Kawamoto, N. Watanabe, E. Toyota, Y. Neishi, R. Sukmawan, Y. Sadahira, and K. Yoshida, "Assessment of coronary intima-media thickness by optical coherence tomography comparison with intravascular ultrasound," *Circulation Journal*, vol. 69, no. 8, pp. 903–907, 2005.

[33] K. Li, X. Wu, D. Z. Chen, and M. Sonka, "Optimal surface segmentation in volumetric images-a graph-theoretic approach," *IEEE transactions on pattern analysis and machine intelligence*, vol. 28, no. 1, pp. 119–134, 2006.

[34] A. Maehara, E. Cristea, G. S. Mintz, A. J. Lansky, O. Dressler, S. Biro, B. Templin, R. Virmani, B. de Bruyne, P. W. Serruys, *et al.*, "Definitions and methodology for the grayscale and radiofrequency intravascular ultrasound and coronary angiographic analyses," *JACC: Cardiovascular Imaging*, vol. 5, no. 3s1, pp. S1–S9, 2012.

[35] R. Medina, A. Wahle, M. E. Olszewski, and M. Sonka, "Volumetric quantification of coronary arteries reconstructed by fusion between intravascular ultrasound

and biplane angiography," in *Biomedical Imaging, 2002. Proceedings. 2002 IEEE International Symposium on.* IEEE, 2002, pp. 891–894.

[36] ——, "Three methods for accurate quantification of plaque volume in coronary arteries," *The international journal of cardiovascular imaging*, vol. 19, no. 4, pp. 301–311, 2003.

[37] ——, "Curvature and torsion estimation for coronary-artery motion analysis," in *Medical Imaging 2004.* International Society for Optics and Photonics, 2004, pp. 504–515.

[38] H. J. Milionis, E. Rizos, and D. P. Mikhailidis, "Smoking diminishes the beneficial effect of statins: observations from the landmark trials," *Angiology*, vol. 52, no. 9, pp. 575–587, 2001.

[39] G. S. Mintz, K. M. Kent, A. D. Pichard, L. F. Satler, J. J. Popma, and M. B. Leon, "Contribution of inadequate arterial remodeling to the development of focal coronary artery stenoses an intravascular ultrasound study," *Circulation*, vol. 95, no. 7, pp. 1791–1798, 1997.

[40] A. Nair, B. D. Kuban, E. M. Tuzcu, P. Schoenhagen, S. E. Nissen, and D. G. Vince, "Coronary plaque classification with intravascular ultrasound radiofrequency data analysis," *Circulation*, vol. 106, no. 17, pp. 2200–2206, 2002.

[41] K. Nasu, E. Tsuchikane, O. Katoh, N. Tanaka, M. Kimura, M. Ehara, Y. Kinoshita, T. Matsubara, H. Matsuo, K. Asakura, *et al.*, "Effect of fluvastatin on progression of coronary atherosclerotic plaque evaluated by virtual histology intravascular ultrasound," *JACC: Cardiovascular Interventions*, vol. 2, no. 7, pp. 689–696, 2009.

[42] S. E. Nissen and P. Yock, "Intravascular ultrasound novel pathophysiological insights and current clinical applications," *Circulation*, vol. 103, no. 4, pp. 604–616, 2001.

[43] T. Nozue, S. Yamamoto, S. Tohyama, S. Umezawa, T. Kunishima, A. Sato, S. Miyake, Y. Takeyama, Y. Morino, T. Yamauchi, *et al.*, "Statin treatment for coronary artery plaque composition based on intravascular ultrasound radiofrequency data analysis," *American heart journal*, vol. 163, no. 2, pp. 191–199, 2012.

[44] K. Ohshima, S. Ikeda, H. Kadota, K. Yamane, N. Izumi, H. Kawazoe, K. Ohshima, and M. Hamada, "Cavity volume of ruptured plaque is an independent predictor for angiographic no-reflow phenomenon during primary an-

gioplasty in patients with st-segment elevation myocardial infarction," *Journal of cardiology*, vol. 57, no. 1, pp. 36–43, 2011.

[45] N. Otsu, "A threshold selection method from gray-level histograms," *Automatica*, vol. 11, no. 285-296, pp. 23–27, 1975.

[46] G. Pasterkamp, C. Borst, M. J. Post, W. P. Mali, P. J. Wensing, E. J. Gussenhoven, and B. Hillen, "Atherosclerotic arterial remodeling in the superficial femoral artery individual variation in local compensatory enlargement response," *Circulation*, vol. 93, no. 10, pp. 1818–1825, 1996.

[47] G. Pasterkamp, Z. S. Galis, and D. P. De Kleijn, "Expansive arterial remodeling: location, location, location," *Arteriosclerosis, thrombosis, and vascular biology*, vol. 24, no. 4, pp. 650–657, 2004.

[48] G. Pasterkamp, P. J. Wensing, M. J. Post, B. Hillen, W. P. Mali, and C. Borst, "Paradoxical arterial wall shrinkage may contribute to luminal narrowing of human atherosclerotic femoral arteries," *Circulation*, vol. 91, no. 5, pp. 1444–1449, 1995.

[49] R. Puri, P. Libby, S. E. Nissen, K. Wolski, C. M. Ballantyne, P. J. Barter, M. J. Chapman, R. Erbel, J. S. Raichlen, K. Uno, *et al.*, "Long-term effects of maximally intensive statin therapy on changes in coronary atheroma composition: insights from saturn," *Eur Heart J Cardiovasc Imaging*, vol. 15, no. 4, pp. 380–388, 2014.

[50] G. A. Rodriguez-Granillo, H. M. García-García, E. P. Mc Fadden, M. Valgimigli, J. Aoki, P. de Feyter, and P. W. Serruys, "In vivo intravascular ultrasound-derived thin-cap fibroatheroma detection using ultrasound radiofrequency data analysis," *Journal of the American College of Cardiology*, vol. 46, no. 11, pp. 2038–2042, 2005.

[51] G. A. Rodriguez-Granillo, P. W. Serruys, H. M. García-García, J. Aoki, M. Valgimigli, C. A. van Mieghem, E. McFadden, P. de Jaegere, and P. de Feyter, "Coronary artery remodelling is related to plaque composition," *Heart*, vol. 92, no. 3, pp. 388–391, 2006.

[52] N. Sattar, D. Preiss, H. M. Murray, P. Welsh, B. M. Buckley, A. J. de Craen, S. R. K. Seshasai, J. J. McMurray, D. J. Freeman, J. W. Jukema, *et al.*, "Statins and risk of incident diabetes: a collaborative meta-analysis of randomised statin trials," *The Lancet*, vol. 375, no. 9716, pp. 735–742, 2010.

[53] P. Schoenhagen, E. M. Tuzcu, C. Apperson-Hansen, C. Wang, K. Wolski, S. Lin,

I. Sipahi, S. J. Nicholls, W. A. Magyar, A. Loyd, *et al.*, "Determinants of arterial wall remodeling during lipid-lowering therapy serial intravascular ultrasound observations from the reversal of atherosclerosis with aggressive lipid lowering therapy (reversal) trial," *Circulation*, vol. 113, no. 24, pp. 2826–2834, 2006.

[54] P. K. Shah and J. S. Forrester, "Pathophysiology of acute coronary syndromes," *The American journal of cardiology*, vol. 68, no. 12, pp. 16–23, 1991.

[55] H. C. Stary, "Natural history and histological classification of atherosclerotic lesions an update," *Arteriosclerosis, thrombosis, and vascular biology*, vol. 20, no. 5, pp. 1177–1178, 2000.

[56] G. W. Stone, A. Maehara, A. J. Lansky, B. de Bruyne, E. Cristea, G. S. Mintz, R. Mehran, J. McPherson, N. Farhat, S. P. Marso, *et al.*, "A prospective natural-history study of coronary atherosclerosis," *New England Journal of Medicine*, vol. 364, no. 3, pp. 226–235, 2011.

[57] S. Sun, M. Sonka, and R. Beichel, "Graph-based IVUS segmentation with efficient computer-aided refinement," 2013.

[58] S. Takarada, T. Imanishi, Y. Liu, H. Ikejima, H. Tsujioka, A. Kuroi, K. Ishibashi, K. Komukai, T. Tanimoto, Y. Ino, *et al.*, "Advantage of next-generation frequency-domain optical coherence tomography compared with conventional time-domain system in the assessment of coronary lesion," *Catheterization and Cardiovascular Interventions*, vol. 75, no. 2, pp. 202–206, 2010.

[59] S. Tani, K. Nagao, T. Anazawa, H. Kawamata, S. Furuya, H. Takahashi, K. Iida, M. Matsumoto, T. Washio, N. Kumabe, *et al.*, "Coronary plaque regression and lifestyle modification in patients treated with pravastatin-assessment mainly by daily aerobic exercise and an increase in the serum level of high-density lipoprotein cholesterol," *Circulation Journal*, vol. 74, no. 5, pp. 954–961, 2010.

[60] G. J. Ughi, K. Steigerwald, T. Adriaenssens, W. Desmet, G. Guagliumi, M. Joner, and J. Dhooge, "Automatic characterization of neointimal tissue by intravascular optical coherence tomography," *Journal of biomedical optics*, vol. 19, no. 2, pp. 021 104–021 104, 2014.

[61] E. S. Unit, "Efficacy and safety of cholesterol-lowering treatment: prospective meta-analysis of data from 90 056 participants in 14 randomised trials of statins," *Lancet*, vol. 366, no. 9493, pp. 1267–1278, 2005.

[62] A. M. Varnava, P. G. Mills, and M. J. Davies, "Relationship between coronary artery remodeling and plaque vulnerability," *Circulation*, vol. 105, no. 8, pp. 939–943, 2002.

[63] R. Virmani, "Are our tools for the identification of tcfa ready and do we know them?," *JACC: Cardiovascular Imaging*, vol. 4, no. 6, pp. 656–658, 2011.

[64] R. Virmani, A. P. Burke, A. Farb, and F. D. Kolodgie, "Pathology of the vulnerable plaque," *Journal of the American College of Cardiology*, vol. 47, no. 8s1, pp. C13–C18, 2006.

[65] R. Virmani, F. D. Kolodgie, A. P. Burke, A. Farb, and S. M. Schwartz, "Lessons from sudden coronary death a comprehensive morphological classification scheme for atherosclerotic lesions," *Arteriosclerosis, thrombosis, and vascular biology*, vol. 20, no. 5, pp. 1262–1275, 2000.

[66] C. von Birgelen, M. Hartmann, G. S. Mintz, D. Böse, H. Eggebrecht, M. Gössl, T. Neumann, D. Baumgart, H. Wieneke, A. Schmermund, *et al.*, "Spectrum of remodeling behavior observed with serial long-term (12 months) follow-up intravascular ultrasound studies in left main coronary arteries," *The American journal of cardiology*, vol. 93, no. 9, pp. 1107–1113, 2004.

[67] C. von Birgelen, G. Mintz, E. De Vrey, T. Kimura, J. Popma, S. Airiian, M. Leon, M. Nobuyoshi, P. Serruys, and P. De Feyter, "Atherosclerotic coronary lesions with inadequate compensatory enlargement have smaller plaque and vessel volumes: observations with three dimensional intravascular ultrasound in vivo," *Heart*, vol. 79, no. 2, pp. 137–142, 1998.

[68] A. Wahle, S. C. Mitchell, R. M. Long, and M. Sonka, "Accurate volumetric quantification of coronary lesions by fusion between intravascular ultrasound and biplane angiography," in *Proceedings of Computer Assisted Radiology and Surgery Conference*, 2000, pp. 549–554.

[69] A. Wahle, M. E. Olszewski, and M. Sonka, "Interactive virtual endoscopy in coronary arteries based on multimodality fusion," *IEEE transactions on medical imaging*, vol. 23, no. 11, pp. 1391–1403, 2004.

[70] A. Wahle, M. E. Olszewski, S. C. Vigmostad, R. Medina, A. U. Coskun, C. Feldman, P. H. Stone, K. C. Braddy, T. M. Brennan, J. D. Rossen, *et al.*, "Quantitative analysis of circumferential plaque distribution in human coronary arteries in relation to local vessel curvature," in *Biomedical Imaging: Nano to Macro, 2004. IEEE International Symposium on.* IEEE, 2004, pp. 531–534.

[71] A. Wahle, G. P. Prause, S. C. DeJong, and M. Sonka, "Geometrically correct 3-D reconstruction of intravascular ultrasound images by fusion with biplane angiography-methods and validation," *Medical Imaging, IEEE Transactions on*, vol. 18, no. 8, pp. 686–699, 1999.

[72] A. Wahle and M. Sonka, "Coronary plaque analysis by multimodality fusion," *Studies in health technology and informatics*, vol. 113, p. 321, 2005.

[73] Z. Wang, H. Kyono, H. G. Bezerra, D. L. Wilson, M. A. Costa, and A. M. Rollins, "Automatic segmentation of intravascular optical coherence tomography images for facilitating quantitative diagnosis of atherosclerosis," in *SPIE BiOS*. International Society for Optics and Photonics, 2011, pp. 78 890N–78 890N.

[74] Y. Yin, X. Zhang, R. Williams, X. Wu, D. D. Anderson, and M. Sonka, "LOGISMOS-layered optimal graph image segmentation of multiple objects and surfaces: cartilage segmentation in the knee joint," *Medical Imaging, IEEE Transactions on*, vol. 29, no. 12, pp. 2023–2037, 2010.

[75] G. Zahnd, A. Karanasos, G. van Soest, E. Regar, W. Niessen, F. Gijsen, and T. van Walsum, "Quantification of fibrous cap thickness in intracoronary optical coherence tomography with a contour segmentation method based on dynamic programming," *International journal of computer assisted radiology and surgery*, vol. 10, no. 9, pp. 1383–1394, 2015.

[76] C. K. Zarins, E. Weisenberg, G. Kolettis, R. Stankunavicius, and S. Glagov, "Differential enlargement of artery segments in response to enlarging atherosclerotic plaques," *Journal of vascular surgery*, vol. 7, no. 3, pp. 386–394, 1988.

[77] L. Zhang, A. Wahle, Z. Chen, L. Zhang, R. Downe, T. Kovarnik, and M. Sonka, "Simultaneous registration of location and orientation in intravascular ultrasound pullbacks pairs via 3D graph-based optimization," 2015.